5-2009

Experimental evaluation and modeling of engine driven heat pump

Isaac Y. Mahderekal
University of Nevada, Las Vegas

EXPERIMENTAL EVALUATION AND MODELING OF ENGINE DRIVEN HEAT PUMP

by

Isaac Y. Mahderekal

Bachelor of Science
University of Nevada, Las Vegas, USA
2002

Master of Science
University of Nevada, Las Vegas, USA
2004

A dissertation submitted in partial fulfillment
of the requirements for the

Doctor of Philosophy Degree in Mechanical Engineering
Department of Mechanical Engineering
Howard R. Hughes College of Engineering

Graduate College
University of Nevada, Las Vegas
May 2009

UNLV
UNIVERSITY OF NEVADA LAS VEGAS

Dissertation Approval

The Graduate College
University of Nevada, Las Vegas

April 17, 2009

The Dissertation prepared by

Isaac Y Mahderekal

Entitled

Experimental Evaluation and Modeling of Engine Driven Heat Pump

is approved in partial fulfillment of the requirements for the degree of

Doctor of Philosophy in Engineering

[redacted]
Examination Committee Chair

[redacted]
Dean of the Graduate College

[redacted]
Examination Committee Member

[redacted]
Examination Committee Member

[redacted]
Examination Committee Member

[redacted]
Graduate College Faculty Representative

ABSTRACT

Experimental Evaluation and Modeling of Engine Driven Heat Pump

by

Isaac Mahderekal

Dr. Robert Boehm, Examination Committee Chair
Professor of Department of Mechanical Engineering
University of Nevada, Las Vegas

Recently, the Gas Engine-Driven Heat Pump (GHP) System has become an economic choice and more attractive climate control system than the conventional air conditioner due to its advantage in reducing fossil fuel consumption and environmental pollution. The GHP is a new type of heat pump in which the compressor (the core part) is driven by a gas engine. The GHP typically uses the work produced by the engine to drive a vapor-compression heat pump. At the same time, the waste heat rejected by the engine is used for heating purposes.

To improve the system performance of the GHP, a numerical and experimental study has been made by using suction-liquid line heat exchangers in cooling operation (particularly in high ambient operations) and suction line waste heat recovery to augment heating capacity. Detail experimental and modeling of a GHP in high ambient operating conditions using R410A as a refrigerant is firstly included in this study.

Computational fluid dynamics (CFD) techniques have been used to study the design of the heat exchangers to improve system performance during heating and cooling operations with refrigerant R-410a and ethylene glycol as the working fluids. Seven cases

were investigated to obtain the optimal operating mode. For the first four cases, the operating fluids in the tube side (vapor refrigerant R410 A) and the shell side (aqueous ethylene glycol) were kept the same while the inlet temperature and mass flow rate for the tube and shell sides are changed in different cases. For the last three cases, the operating fluids on the shell side are changed to liquid refrigerant R410A. The numerical results show that although the effectiveness of the shell tube exchanger is small due to the small thermal conductivity of vapor refrigerant R410A, the goal of this numerical study still has been reached and over 30,000 Btu/hr heat exchange has been obtained with the current heat exchanger configuration. The output from the CFD analysis, total heat transferred and pressure drop, are used as an input to the overall GHP modeling.

The performance of overall GHP system has been simulated by using ORNL Modulating Heat Pump Design Software, MODCON, which is used to predict steady-state heating and cooling performance of variable-speed vapor compression air-to-air heat pumps for a wide range of system configuration and operational variables. The modeling includes: (1) GHP cycle without any performance improvements (suction liquid heat exchange and heat recovery) as a baseline (both in cooling and heating mode), (2) the GHP cycle in cooling mode with the suction to the liquid heat exchanger incorporated, (3) GHP cycle in heating mode with heat recovery (recovered heat from engine). According to the system simulation results, a performance gain by using suction liquid line heat exchanger is obtained especially at higher ambient conditions. The waste heat of the gas engine can take about 20-25% of the total heating capacity in rated operating condition. The ambient temperature affects the performance of the heat pump but has little influence on the engine efficiency in the constant engine speed model. Because of

the limitation of speed, the GHP still needs extra equipment to back up the heating in extremely low ambient temperatures.

The modulating heat pump model was compared to experimental trends with respect to compressor speed and the basis of coefficient of performances (COPs) and capacities. The experiment was conducted with use of a psychrometric test facility at Oak Ridge National Heat pump Laboratory. The trends in COP and capacity were generally well predicted. The results of the absolute comparisons over a range of speeds and ambient conditions indicated that best model agreement was obtained at lower speeds in both the heating and cooling modes, with increasing performance over predictions (to maximums of about 10% in both COP and capacity) occurring at higher speeds.

Finally, a comparison of applications of GHP with its most common counterparts, an electrical DX heat pump, in a 5000 ft^2 office building was made in two typical locations (Las Vegas and Chicago) with using thermal simulation software. According to the comparisons, a primary energy saving (10.6% for the Las Vegas simulation and 22.6% for the Chicago simulation less than its nearest alternative) as well as much less CO_2 emissions (26% for the Las Vegas simulation, and 59.9% for the Chicago simulation less than its nearest alternative) for a GHP system were found.

TABLE OF CONTENTS

LIST OF FIGURES

LIST OF TABLES

NOMENCLATURE

$C_{1\varepsilon}$ $C_{2\varepsilon}$ $C_{3\varepsilon}$	constant
Capacity	refrigeration capacity
COP	coefficient of performance
C_p	specific heat at constant pressure,
C_{pa}	specific heat of air
D	discharge saturation temperatures
E	effectiveness of the shell-tube heat exchanger
f	Moody friction factor
Fv	volumetric efficiency correction factor
G_b	generation of turbulence kinetic energy due to buoyancy
G_k	generation of turbulence kinetic energy due to the mean velocity gradients
h	heat transfer coefficient
h_a	fan-motor efficiency
h_{outlet}	enthalpy at the compressor shell outlet
$h_{outlet,isen}$	enthalpy at the compressor shell outlet (isentropic)
L	length of pipe
k	turbulence kinetic energy
$\dot{m}$	mass flow rate

$\dot{m}_{map}$	refrigerant mass flow rate
M_w	molecular weight of the gas
n	engine speed
p	static pressure
P_{op}	operating pressure
Q_{mi}	air flow, indoor, measured
Q_{shell}	heat loss rate from the compressor shell
R	universal gas constant
RCI	relative capacity change index
Re	Reynolds number
S	the compressor suction temperatures
S_k , S_ε	user-defined source terms
t	time
t_{ain}	air temperature entering the indoor unit
t_{aout}	air temperature leaving the indoor unit
$T_{vapor,out}$	vapor outlet temperature of tube side
$T_{vapor,in}$	vapor inlet temperature of tube side
$T_{liquid,in}$	liquid inlet temperature of shell side
T_r	torque
$Tevap$	evaporator temperature
$Tcond$	condenser temperature

U	velocity magnitude
ui	mean velocity component (i=1,2,3)
u_i'	fluctuating velocity components (i = 1; 2; 3)
$\dot{W}_{fan}$	fan motor power consumption
W_{i1}	humidity ratio of air entering the indoor unit
W_{i2}	humidity ratio of air leaving the indoor unit
$\dot{W}_{map}$	compressor power input
W_n	humidity ratio of air at orifice throat
x_i	coordinate
y	represents the power output, fuel input and recoverable engine heat
Y_M	contribution of the fluctuating dilatation in compressible turbulence to the overall dissipation rate
ε	rate of dissipation
μ	dynamic viscosity
μt	turbulent viscosity
ρ	density
σ_k	turbulent Prandtl number for k
σ_ε	turbulent Prandtl number for ε
$\lambda_1 - \lambda_{10}$	map coefficients
ν	kinematic viscosity
ν_n'	specific volume of air at orifice throat

v_{inlet}	specific volume at compressor shell inlet
Δh	enthalpy change

ACKNOWLEDGEMENTS

I would like to express my profound gratitude and sincere appreciation to Dr. Robert Boehm for his inspiration, indispensable guidance and for teaching me invaluable knowledge throughout the course of my study. With his initial support, this great dream of mine can finally turn to reality, and with his unending guidance throughout the study, I was able to navigate the arduous path down to the very end. I am sure that whatever I have learned while working with him will be very useful in my future endeavors. He has been a great mentor.

I sincerely thank all my committee members, Dr. Yim Woosoon, Dr. Samir F. Moujaes, Dr. Daniel Cook and Dr. Eugene McGaugh for their support and providing valuable suggestions along the way.

I am very thankful to my employer Team Consulting for their continued support. I would also like to express my gratitude to the shop personnel at Oak Ridge National Laboratory. I will never forget the time when we worked together in the lab and will always value the team sprit.

I would like to express my deep sense of gratitude towards my parents and to my siblings who have always shown unfaltering faith in me. I cannot leave out my friends, and colleagues who were a great support during the course of my study.

CHAPTER 1

INTRODUCTION AND LITERATURE SURVEY

1.1. Introduction

Nowadays, two of the main problems in the world are depletion of fossil fuels and environmental pollution. Consumption of energy, especially domestic consumption, mainly occurs in space cooling/heating, and the source of energy used in these applications is generally supplied from fossil fuels and/or electricity produced from them. Improved air-conditioning technology thus has the greatest potential impact.

Heat pump (HP) systems are heat-generating devices that transfer heat from a low temperature medium to a high temperature. HPs generally use a vapor-compression cycle or absorption-compression cycle. HPs are divided into many categories according to energy sources, namely electric driven HPs (EHPs), chemical HPs, ground source HP, geothermal energy HP, solar assisted HPs and/or hybrid power systems etc. and gas engine driven HPs (GHPs). Generally, fuel is mainly converted to electrical energy at power plants and the waste heat is discharged to the environment, then electrical energy is transmitted to the HPs and is converted to mechanical energy by the motor of the HPs. In this process, energy is converted twice and the heat loss is high as shown in Figure 1.1 [1-5].

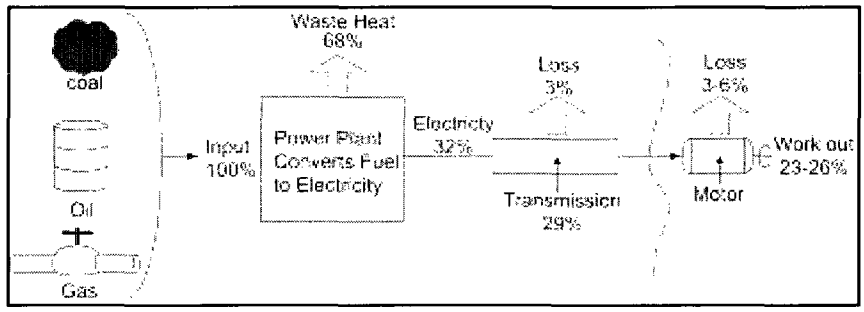

Figure 1.1 Losses of the Conversion Process from Fuels to Work of a Heat Pump.

However, energy efficiency can become higher if fuel conversion can be located closer to where heat is required. Then the heat released in the conversion can be more efficiently used. GHPs are harmonious with this concept as they have high energy efficiency, especially in heating.

Much is expected from GHPs as a product that would help satisfy the air conditioning system demand from medium and small sized buildings to restrict electric power demand peaks in summer and save energy in general. In many instances, GHP is a more attractive climate control system than the conventional air conditioner [6] and [7], e.g.:

A. Variable speed operation: Typically, the GHP can cycle at minimum speed and modulate between a minimum and maximum speed to match the required load. The minimum and maximum speeds are decided by the performance of the engine and compressor. As a result, the part load efficiency of such a system will be high. Its seasonal operational cost and cycling losses will be lower than those of a single speed system with an on–off control system.

B. Engine heat recovery: The engine's heat efficiency is not very high (about 30% for gas engines now) [7]. The heat of fuel combustion is wasted through exhaust gases, cooling water and the engine block. However, the system's efficiency will

C. Natural gas fuel: GHPs also differs from an electric heat pumps (EHP) in the energy they use, primarily natural gas or propane instead of electricity. So, a GHP is preferred in a region where electric costs are high and natural gas is readily available.

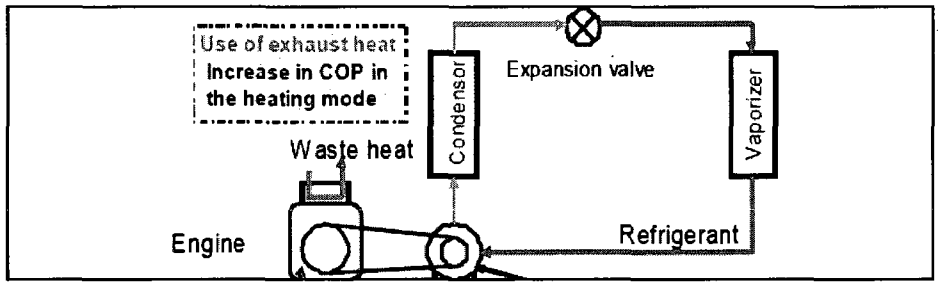

Figure 1.2 Basic Diagram of a GHP

As shown in Figure 1.2, the GHP typically uses the work produced by the engine to drive a vapor-compression heat pump. At the same time, the waste heat rejected by the engine is used for heating purposes. Thus, the GHP is inherently more efficient than conventional heating-systems currently marketed (e.g. furnace, direct-fired absorption heat-pump or electrical heat pump). Since the high energy efficiency of GHPs causes low fossil fuel consumption, the environmental pollution could be reduced. In addition, GHPs use relatively inexpensive energy sources, such as natural gas, propane or liquefied petroleum gas (LPG) instead of electricity [8], so GHPs become an economic choice [5], [9] and [10]. Furthermore, GHPs can play important social and economic roles by

effectively balancing electricity demand, mitigating the electricity peaks and adjusting the energy configuration.

1.2. Description of a GHP

A heat pump is used to transfer thermal energy from a low temperature reservoir to a high temperature field to cool or heat. The GHP is a new type of heat pump in which the compressor (the core part) is driven by a gas engine. In this study the GHP system shown in Figure 1.3 will be investigated. The GHP system consists of the gas engine (E-1), an open type compressor (K1-A and B), pump (P-1), thermostatic expansion valve (TXV), oil separator (S-2), outdoor heat exchanger (C-1), indoor heat exchanger (C-2A), radiator (C-3), coolant exhaust heat exchanger (EAX-1) and valves. In addition to the common components of a regular heat pump listed above, this study will also investigate suction liquid heat exchanger (SGLLHX) and heat recovery heat exchanger (HEX-1) to improve the performance of the GHP in cooling and heating mode respectively.

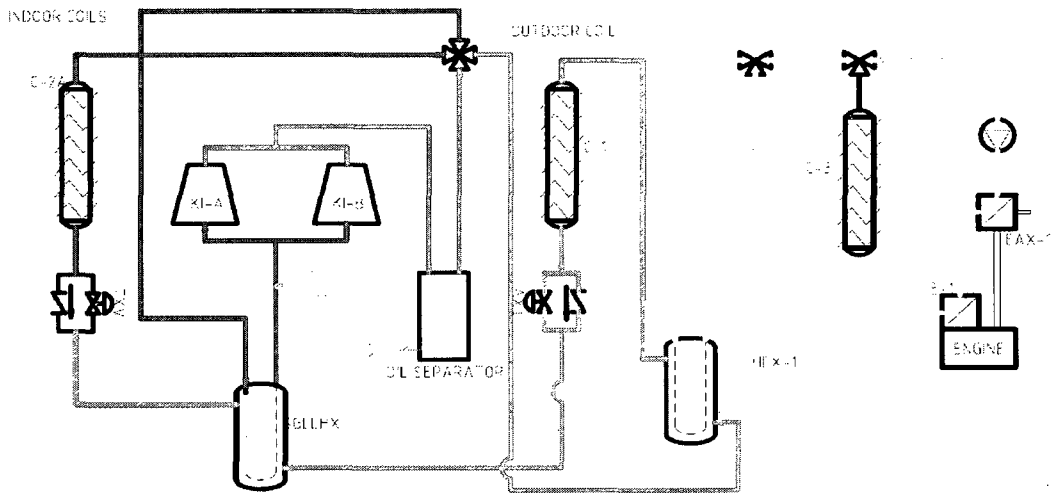

Figure 1.3 Schematic Diagram of GHP to be Studied

Low pressure and temperature refrigerant vapor is compressed to high pressure by compressors. As the vapor is compressed, its temperature increases. The now hot, high pressure refrigerant vapor flows to oil separators which separate oil from the refrigerant. The separated refrigerant oil is returned to compressor suction line through metering devices and solenoid valves. Solenoid valves 13A, 13B are activated by a control system in response to changing operating conditions to provide optimum oil flow to the compressors.

The hot, high pressure refrigerant vapor flows from the oil separators to reversing or switching valves, where the vapor is diverted to the indoor exchanger or the outdoor exchangers depending on whether the system is in heating or cooling mode. When the system is in the cooling mode or cycle, the switching valves divert hot, high pressure refrigerant to the outdoor heat exchangers which in the cooling mode, act as condensers. The high temperature, high pressure refrigerant is then condensed to a high pressure liquid and sub-cooled by removing heat from the refrigerant. The heat is removed by drawing cooler outdoor air across the outdoor heat exchanger. Outdoor fans provide the air flow to the required refrigeration load and outdoor ambient conditions. The high pressure sub-cooled refrigerant liquid then flows through check valve devices to thermostatic expansion device.

The thermostatic expansion devices (TXV) regulate the refrigerant flow which lowers the pressure of the refrigerant as it flows through the device. The pressure reduction causes expansion of the refrigerant liquid whereby a portion flashes into a vapor which, according to the Joule-Thompson effect, the temperature of the two phase refrigerant is reduced. Now the low temperature, two-phase refrigerant then enters indoor heat

exchanger which functions as an evaporator in the cooling mode. Warm return air from the subject air-conditioned space is drawn across the indoor heat exchanger by indoor blower. Heat is removed from the return air thereby cooling the air stream. The cool air stream is then returned to the subject air-conditioned space.

The heat removed from the air stream is transferred to the cold two-phase refrigerant flowing through the tubes of the indoor heat exchanger causing the liquid refrigerant to boil. After all liquid refrigerant has boiled into vapor, additional heat is added to the heat exchanger causing the refrigerant vapor to become superheated. Amount of superheat is controlled by the TXV devices. The superheated refrigerant vapor then flows back to the switching valves and then drawn into low pressure inlets of the compressors such that the cycle can be repeated.

Figure 1.3 also illustrates a direct-expansion vapor compression refrigeration system utilizing a liquid-suction heat exchanger. In this configuration, high temperature liquid leaving the heat rejection device (condenser in this case) is sub cooled prior to being throttled to the evaporator pressure by an expansion device such as a thermostatic expansion valve. Thus, the liquid-suction heat exchanger is an indirect liquid-to-vapor heat transfer device.

Table 1.1 Investigated Unit Specifications

Engine	Water-cooled, 4 cycle, 3 cylinder, 9.5kW rated output
Engine speed	1200 to 2450 rpm
Fuel type	Natural gas or propane
Compressor	Scroll type, 60.5 cc/rev.
Compressor	2280 to 4655 rpm
Refrigerant type	R410A
Design cooling rating	120,000 Btu/hr
Design heating rating	140,000 Btu/hr
Electrical power requirement	2 kW

During both heating and cooling operation, engine coolant is circulated throughout the system by a coolant pump. Warm coolant is pumped through the exhaust heat exchanger (shell and tube heat exchanger), where its temperature is raised a few degrees by waste heat recovered from the engine exhaust. The coolant then flows to the water cooled exhaust manifold located on the internal combustion engine, where its temperature is further increased. The coolant then enters the internal combustion engine and removes heat from the engine. This portion of the coolant circuit is where engine waste heat is recovered for efficient use during the heating cycle. When the GHP is operated in the heating mode, waste heat is removed from the engine and exhaust by the coolant and is directed to the heat recovery heat exchanger (HEX). All hot engine coolant is directed to heat exchanger, thus transferring all recoverable waste heat from the engine into the suction stream of the refrigerant cycle. When the GHP is operated in the cooling mode,

waste heat is removed from the engine and exhaust by the coolant directed to the radiator and rejected to the atmosphere.

1.3. Literature Review

1.3.1. Theoretical and Experimental Investigation of a GHP

Many researchers have studied the GHP [11], but most of them devote their attention to the system integral energy efficiency and economic aspects of the units by way of field tests [11-18]. Very few of these investigations are related to system modeling and even fewer investigators focus on the mutual effect between the engine and the heat pump system. In fact, the performance of the gas engine would be much affected by the operating condition of heat pump, and at the same time, the engine waste heat will also affect the heating performance of the heat pump.

In 1981, Japan's Ministry of International Trade and Industry (MITI) launched a small-scale gas cooling technology research association, pairing gas engine manufacturers with HVAC equipment manufacturers. As a result, gas engine-driven heat pumps have been on the market in Japan since 1987. And since the late 1970s, the Gas Research Institute (GRI), the U.S. Department of Energy (DOE), and others funded American research and development of this new technology [11]. As part of the development process, Japan's Tokyo Gas conducted field tests of five gas engine-driven heat pumps (1-2 tons cooling capacity, a typical residential size) produced by different manufacturers. Engines and compressors were automotive or diesel engines and automotive or general-purpose compressors. All units used R-22 refrigerant. The units also heated water for domestic use, stored in auxiliary tanks. Tokyo Gas installed the

units in 15 residential and commercial buildings and evaluated them for up to 18 months between 1983 and 1985. Tokyo Gas monitored: gas and electric consumption, operating hours (cycling on/off times, run hours, and defrost time), engine speed, indoor and outdoor temperature and humidity, refrigerant temperatures. At the end of the tests, researchers determined performance characteristics and pinpointed equipment reliability problems which, in turn, indicated the design modifications needed. All of the units met cooling and water heating loads during the summer, water heating loads in spring and fall, and space heating loads in the winter. Based on the field test data, researchers determined both steady-state and seasonal Coefficients of Performance (COPs) for each of the five units. (The COP, a dimensionless number, is the ratio of total heating or cooling capacity in Btu/hr, to total energy consumption in Btu/hr, under designated operating conditions.) Steady state COPs for heating at 45 degrees F were 1.20, and for cooling at 95 degrees F, 0.74-.99. Researchers also compared estimated operating costs of the gas heat pumps to two conventional electric heat pump scenarios, one with an electric water heater and the other with a gas water heater. In both instances, the gas heat pump operating costs were lower. Operating costs for the electric heat pumps were, with a gas water heater, 16-35% higher than that for the gas heat pumps, and with an electric water heater, 29-56% higher [11-14].

Several reliability and design problems emerged including noise, vibration-induced piping damage, leaks, control signal errors, starter unreliability, refrigerant pressure problems, engine and valve corrosion, and inadequate oil tank shielding from rain which caused engine burnout. Manufacturers attempted to correct these faults in later models.

However, gas heat pumps by design are more likely to leak refrigerant at the shaft seal, which electric heat pumps avoid by keeping both motor and compressor within one case.

In a second study, after gas engine-driven heat pumps had been in the marketplace for four years with 14,000 installed, Tokyo Gas tracked the incidence of problems from April 1990 to March 1991. This study refined the problems into five main areas: engine-related (39%), refrigeration cycle-related (14%), control-related (23%), unit main body-related (6%), and other problems (17%). Tokyo Gas also found that the newer the model, the less frequent these problems appeared, indicating that design was improving. The percentage of units with any kind of trouble at all decreased from 100% for the 1980's model years to 19% for the 1990's model years [19].

An early modeling study about GHP systems was done by MacArthur and Gerald [20]. They presented a dynamic model of vapor compression HP, including a mathematical treatment of the condenser and evaporator. Lumped-parameter models were developed for the expansion device, natural-gas-fueled internal combustion engine and compressor (open and hermetic). The spatial variations of temperature, enthalpy, mass flow rate and density are predicted at each point in time for the two heat exchangers. The engine model consists of five major components: the throttle body sub model to simulate the intake system; engine steady state performance maps developed from a detailed model of the engine; the engine heat transfer sub model for heat flow from the cylinder to the coolant and the ambient; engine structure temperature corrections to the steady state performance maps; and the ignition-off representation of the engine. The three node heat transfer model simulates heat flow between the inner structure of the engine and the coolant, to the outer structure and the environment. The results of the heat pump model

for the 2 ton open compressor system have been compared with laboratory data at several ambient conditions and compressor speeds. Good agreement between model and laboratory figures was demonstrated in the cooling mode for an ambient temperature of 101.5°F and compressor speed of 978 rpm as well as for an ambient temperature of 75°F and compressor speed of 1512 rpm [20].

Rusk et al. [21] established a mathematical model consisting of two parts, an engine model and a HP model. This model was more consistent than the others but it had not taken into account any heat recovery being critical for GHP. The model is done by developing a system of equations based on the conservation laws of physics, generalized correlations appropriate to the situation, and the physical characteristics of the component and system. The model predicted the seasonal COP values to be greater than one for both for northern and southern U.S. weather conditions. This makes the GHP more energy efficient than direct gas or electric resistance heating.

Following the initial model [21], an improved dynamic model was presented taking into consideration the exhaust gas. This model included an exhaust gas heat exchanger. The exhaust heat recovery system is an essential part for a gas engine-driven heat pump (GHP). An integrated simulation mathematical model consisting of a gas engine model and an exhaust gas heat exchanger model was presented for the dynamic performance of the exhaust heat recovery system. A computer program was also developed for the model. A comparison of the experimental results indicated that the mathematical model presented in this study could simulate the thermodynamic performance of the system satisfactorily and could be used to guide the design of the exhaust heat recovery system for the GHP [22-23].

Zhang et al. [24] established another simulation tool, which contained a theoretical heat recovery model. In this study, the heating performance of a gas engine driven air-to-water heat pump was analyzed using a steady state model. The thermodynamic model of a natural gas engine is identified by the experimental data and the compressor model is created by several empirical equations. The heat exchanger models are developed by using heat balances. The system model is validated by comparing the experimental and simulation data, which show good agreement. To understand the heating characteristic in detail, the performance of the system is analyzed for a wide range of operating conditions, and especially the effect of engine waste heat on the heating performance is discussed. The results show that engine waste heat can provide about 1/3 of the total heating capacity in this gas engine driven air to water heat pump. The performance of the engine, heat pump and integral system are analyzed under variations of engine speed and ambient temperature. It shows that engine speed has remarkable effects on both the engine and heat pump, but ambient temperature has little influence on the engine's performance. The system and component performances in variable speed operating conditions are also discussed. The results show that:

A. the waste heat of the gas engine can take about 30% of the total heating capacity in rated operating condition;
B. both the heat pump and engine system are influenced significantly by engine speed. The increase of engine speed will decrease the efficiency of the heat pump and the total energy efficiency of the engine. The decrease of engine speed will affect the power efficiency of the engine but the total energy efficiency will

C. the ambient temperature affects the performance of the heat pump to a large degree but has little influence on the engine efficiency in the constant engine speed mode;

D. when operated in the whole heating season, the GEHP has perfect performance due to its easy speed modulation. However, because of the limitation of speed, the GEHP still needs extra equipment to back up the heating in extreme low ambient temperatures, while in light heating load conditions, some other capacity control strategy should be adopted to reduce the system energy consumption.

Investigations on improving the performance of GHP systems have also been made. The performance of three combined absorption/vapor compression cycles was assessed in a theoretical study with regard to their feasibility to enhance the efficiency and capacity of gas-fired internal combustion engine-driven heat pumps. Coefficients of performance and the capacity have been calculated for typical heating and cooling applications. Operating parameters and the heat duties were also investigated. When all of the exhaust heat is used for heat pumping in addition to the work output, then a performance improvement with regard to both capacity and coefficient of performance, of up to 31% for cooling and 17 % for heating can be accomplished with the desorber-absorber heat exchange (DAHX) cycle, and, respectively, 21 and 11% for the simple absorption cycle (SC). The total heat duty increases up to 32 % for the DAHX cycle and 23 % for the SC compared with conventional engine-driven systems. The study also indicated that the increase in heat transfer area is smaller than the increase in heat duty due to more

favorable heat transfer coefficients. Initial economic considerations indicate that the change in first cost is small because the increased heat exchange surface requirement is offset by smaller compressor and ICE size [25].

Rakopoulos [26] presented a detailed survey concerning the work committed so far to the application of the second-law of thermodynamics in internal combustion engines. Detailed equations were given for the evaluation of state properties, the first-law of thermodynamics, fuel chemical availability, the second-law of thermodynamics applied to all engine subsystems and the definition of second-law efficiencies together with explicit examples. The research in the field of the second-law application to internal combustion engines has covered so far both compression ignition (CI) and spark ignition (SI) four-stroke engines fundamentally, by also including most of the engine parameters effect. The review of the previous works was categorized in various subsections, i.e. compression ignition engines (overall analyses and phenomenological models-direct and indirect injection), spark ignition engines, engine subsystems, low heat rejection, alternative fuels, and transient operation. Typical tables were given presenting the first- and second-law efficiency analyses of various engine configurations studied, where the different magnitude that the second-law attributes to the engine processes was highlighted. Some interesting results have been obtained from this field when the second-law balance is applied. For example, the decomposition of lighter fuels (e.g. methane or methanol) molecules during chemical reaction creates lower entropy generation than the larger n-dodecane molecule. All in all, ethanol, methane, methanol, oxygen enrichment and compressed natural gas (CNG) prove favorable from the second-law perspective,

whereas water addition and butanol increase the (spark ignition engine) combustion irreversibility and are, thus, not recommended.

1.3.2. Investigation of Refrigerant R410A on Heat Pump Operation

Due to the impending ban of refrigerant R-22 production, there is a pressing need for studies on the performance characteristics of alternative refrigerants in air-conditioning and heat pump systems. Therefore a survey of the previous investigations on R-22 replacement refrigerants in these systems is a very important part of this present study.

Radermacher and Jung [27] conducted a simulation study of potential R-22 replacements in residential equipment. The coefficient of performance (COP) and the seasonal performance factor (SPF) were calculated for binary and ternary substitutes for R-22. They found that for a ternary mixture of R-32/R-152a/R-124 with a concentration of 20 wt%/20 wt%/60 wt%, the COP was 13.7% larger and the compressor volumetric capacity was 23% smaller than the respective values for R-22. This study found that in general, based on thermodynamic properties only, refrigerant mixtures have the potential to replace R-22 without a loss in efficiency. Efficiency gains are possible when counter flow heat exchangers are used and additional efficiency gains are possible when capacity modification is employed.

Kondepudi [28] performed experimental "drop-in" (unchanged system, same heat exchangers) testing of R-32/R-134a and R-32/R-152a blends in a two-ton split-system air conditioner. Five different refrigerant blends of R-32 with R-134a and R-152a were tested as "drop-in" refrigerants against a set of R-22 baseline tests for comparison. No hardware changes were made except for the use of a hand-operated expansion device, which allowed for a "drop-in" comparison of the refrigerant blends. Hence, other than the

use of a different lubricant and a hand-operated expansion valve, no form of optimization was performed for the refrigerant blends. Parameters measured included capacity, efficiency, and seasonal efficiency. The steady state energy efficiency ratio (EER) and seasonal efficiency energy efficiency ratio (SEER) of all the R-32/R-134a and R-32/R-152a blends tested were within 2% of those for a system using R-22. The 40 wt%/60 wt% blend of R-32/R-134a performed the best in a non-optimized system.

Domanski and Didion [29] evaluated the performance of nine R-22 alternatives. The study was conducted using a semi-theoretical model of a residential heat pump with a pure cross-flow representation of heat transfer in the evaporator and condenser. The models did not include transport properties since they carried the implicit assumption that transport properties (and the overall heat transfer coefficients) are the same for the fluids studied. Simulations were conducted for "drop-in" performance, for performance in a modified system to assess the fluids' potentials, and for performance in a modified system equipped with a liquid line/suction-line heat exchanger. The simulation results obtained from the "drop-in" evaluation predicted the performance of candidate replacement refrigerants tested in a system designed for the original refrigerant, with a possible modification of the expansion device. The "drop-in" model evaluations revealed significant differences in performance for high-pressure fluids with respect to R-22 and indicated possible safety problems if those fluids were used in unmodified R-22 equipment. The simulation results obtained from the constant heat-exchanger-loading evaluation corresponded to a test in a system modified specifically for each refrigerant to obtain the same heat flux through the evaporator and condenser at the design rating point. This simulation constraint ensures that the evaporator pressures are not affected by the

different volumetric capacities of the refrigerants studied. The results for the modified system performance showed that capacity differences were larger for modified systems than for the "drop-in" evaluation. However, none of the candidate replacement refrigerants exceeded the COP of R-22 at any of the test conditions.

Bivens [30] compared experimental performance tests with ternary and binary mixtures in a split system residential heat pump as well as a window air-conditioner. This study investigated refrigerants R-407c, a ternary zeotropic mixture of 23 wt% R-32, 25 wt% R-125 and 52 wt% R-134a, and R-410b, a near azeotropic binary mixture composed of 45 wt% R-32 and 55 wt% R-125 as working fluids. The heat pump used for the evaluations was designed to operate with R-22 and was equipped with a fin-and-tube evaporator with 4 refrigerant flow parallel circuits, and a condenser with five circuits and one sub-cooling circuit. It was found that R-407c provided essentially the same cooling capacity as compared with R-22 with no equipment modification. R-410b provided a close match in cooling capacity using modified compressor and expansion devices. The energy efficiency ratio for R-407c versus R-22 during cooling ranged from 0.95 to 0.97. The energy efficiency ratio for R-410b versus R-22 during cooling ranged from 1.01 to 1.04.

In summation, in the search for a replacement for refrigerant R-22 many refrigerants have been studied. Many of those studied are refrigerant mixtures. A list of many of the refrigerant mixtures studied by the sources sited in this literature survey is summarized below:

A. Refrigerant R-410a - R-32/50%, R-125/50% (weight percent)

B. Refrigerant R-407b R-32/45%, R-125/55% (weight percent)

C. Refrigerant R-407c R-32/23%, R-125/25%, R-134a/52% (weight percent)

As a result of many of the studies discussed in this literature survey, refrigerant R-410a has emerged as the primary candidate to replace R-22 in many industrial and residential applications.

1.3.3. Investigation on Suction/Liquid Heat Exchanger

Liquid-suction heat exchangers are commonly installed in refrigeration systems with the intent of ensuring proper system operation and increasing system performance. Specifically, ASHRAE Refrigeration Handbook 1998 states that liquid-suction heat exchangers are effective in:

A. increasing the system performance,

B. subcooling liquid refrigerant to prevent flash gas formation at inlets to expansion devices, and

C. fully evaporating any residual liquid that may remain in the liquid-suction prior to reaching the compressor(s) [31]

Stoecker and Walukas [32] focused on the influence of liquid-suction heat exchangers in both single temperature evaporator and dual temperature evaporator systems utilizing refrigerant mixtures. Their analysis indicated that liquid-suction heat exchangers yielded greater performance improvements when nonazeotropic mixtures were used compared with systems utilizing single component refrigerants or azeoptropic mixtures.

McLinden [33] used the principle of corresponding states to evaluate the anticipated effects of new refrigerants. He showed that the performance of a system using a liquid-suction heat exchanger increases as the ideal gas specific heat (related to the molecular complexity of the refrigerant) increases.

Domanski and Didion [34] evaluated the performance of nine alternatives to R22 including the impact of liquid-suction heat exchangers. Domanski et al. [35] later extended the analysis by evaluating the influence of liquid-suction heat exchangers installed in vapor compression refrigeration systems considering 29 different refrigerants in a theoretical analysis.

Bivens et al. [36] evaluated a proposed mixture to substitute for R22 in air conditioners and heat pumps. Their analysis indicated a 6-7% improvement for the alternative refrigerant system when system modifications included a liquid-suction heat exchanger and counterflow system heat exchangers (evaporator and condenser).

Bittle et al. [37] conducted an experimental evaluation of a liquid-suction heat exchanger applied in a domestic refrigerator using R152a. The authors compared the system performance with that of a traditional R12-based system. Bittle et al. [38] also compared the ASHRAE method for predicting capillary tube performance (including the effects of liquid-suction heat exchangers) with experimental data. Predicted capillary tube mass flow rates were within 10% of predicted values and subcooling levels were within 3°F of actual measurements.

Klein and Brownell [39] concluded that liquid-suction heat exchangers that have a minimal pressure loss on the low pressure side are useful for systems using R507A, R134a, R12, R404A, R290, and R407C. The liquid-suction heat exchanger is detrimental to system performance in systems using R22, R32, and R717.

Kim and Shin [40] presented test results of a residential window air-conditioner using R-22 and two potential alternative refrigerants, R-407C and R-410B. A series of performance tests have been carried out for the basic and liquid suction heat exchange

cycles in a psychrometric calorimeter of which the dry and wet bulb temperatures for the indoor and outdoor chambers are 80/67°F and 95/75°F, respectively. For R-407C, the same rotary compressor was used as in the R-22 system. The R-410B system was equipped with a newly designed compressor to provide the similar cooling capacity as the baseline system. The liquid suction heat exchange cycle with the modified counter-cross flow evaporator was considered to improve the system performance. System characteristics such as cooling capacity, energy efficiency ratio, and suction and discharge pressures and heat exchanger temperature profiles are presented compared to those for the baseline R-22 system. The modified system with a liquid suction heat exchanger increased cooling capacity and energy efficiency by up to 5%.

Another goal of this study is to evaluate a liquid-suction heat exchanger design and quantify its impact on system capacity and performance. The influence of liquid-suction heat exchanger size over a range of operating conditions will be illustrated and quantified. The investigation extends the results presented in previous studies in that it considers new refrigerant (R410A); it specifically considers the effects of the pressure drops. Computational fluid dynamics analysis (CFD) will be conducted on the shell and tube heat exchanger design to estimate the pressure drops across the heat exchanger and temperature differences. The values from the CFD analysis will be the input parameters in the heat pump model to evaluate the overall performance gain.

1.4. Motivation of the Dissertation

According to the literature reviewed, there is no detailed information in available current publications concerning detail experimental and modeling of a GHP in high

ambient operating conditions using R410A as a refrigerant. Knowledge of the performance characteristics of air-cooled refrigerant heat exchangers with alternative refrigerants is of practical importance in designing air-cooled heat exchangers required in air-conditioning equipment.

As one of the most promising systems that have emerged in recent years, GHP offers an attractive efficiency (performance) for space heating, as compared with other heating systems such as the gas furnace, electric heat pump, and electric resistance heating. At the same time, it is capable of a space cooling performance comparable to that of the electric heat pump (i.e., electric air conditioner). However, there is no detailed system study which focused on the modeling of GHP numerically and experimentally based on the literature review. Another motivation of this study is to improve the performance of the GHP such as using suction-liquid line heat exchangers in cooling operation (particularly in high ambient operations) and suction line waste heat recovery to augment heating capacity. The improved performance will results in greatly economical saving in fossil fuel consumption and reducing the environmental pollution.

In this study, the heat pump model is created using correlations of experimental data for engine/compressor performance and heat recovery. The model is used to predict heat pump performance for a fixed total coil size (indoor coil plus outdoor coil); various parameters are investigated to evaluate the influence on the IC engine driven heat pump performance. From this model, the design can be optimized to yield the maximum performance for heating and cooling. Since the design yielding maximum performance is associated with the highest capital cost, the optimum design is determined by a tradeoff

between economics and performance. The results of this analysis are then generalized for any size system and economic conditions.

1.5. Research Objectives

The primary objective of this current work is to study the design and performance of an engine driven heat pump (GHP) system with refrigerant R-410a as the working fluid. The GHP system operating conditions are varied so that the system's performance can be evaluated. Subsequently, it is also the intent of this study that the methodology detailed in this work provides guidelines for future design optimizations of this type technology. A secondary objective of this study is to investigate cooling and heating performance improvement by transferring heat from the liquid line to suction in cooling mode and the recovered heat from engine coolant and exhaust to the refrigerant in the suction line in heating mode. A summary of the overall work includes:

A. Little experimental data exist for natural gas engine driven heat pump. Several tests in cooling and heating modes will be conducted and the engine model from experimental data will be identified. The steady working condition of the engine is mainly a function of load and speed. In the GHP system modeling the concerned parameters are fuel consumption, inlet and outlet coolant temperature of the engine and coolant flow rate. A second order bivariante regression polynomial equation is employed here to express the relationship between the required parameters.

B. Conduct a computational fluid dynamics (CFD) simulation to design and evaluate the viability of a shell and tube heat exchanger.

C. The GHP is modeled using ORNL Modulating Heat Pump Design Software. The ORNL Modulating Heat Pump Design Tool consists of a Modulating HPDM (Heat Pump Design Model) and a parametric-analysis (contour-data generating) front-end. Collectively the program is also referred to as MODCON which is in reference to the modulating and the contour data generating capabilities. In this study, the GHP is modeled in the following steps:

   i. The GHP cycle without any performance improvements (suction liquid heat exchange and heat recovery) as a baseline (both in cooling and heating mode).

   ii. The GHP cycle is modeled in cooling mode with the suction to liquid heat exchanger incorporated.

   iii. The GHP cycle is modeled in heating mode with the heat recovery (recovered heat from engine) circuit incorporated.

D. Compare the application of GHP system in different locations with the most common counter parts, an electrical DX heat pump with using the thermal simulation software, Energy Plus. Obtain the primary energy cost and CO_2 emission for different systems to evaluate the performance of GHP system.

1.6. Outline of Dissertation

This dissertation focuses on the development of a system modeling of the GHP system with using numerical and experimental methods. The parametric study has been made to evaluate the impact of differencing operating parameters on the system performance. The outline of this dissertation is list as follow:

In Chapter 2, the CFD model has been established to evaluate the heat performance of a liquid-suction heat exchanger with using the working refrigerant (R410A). Seven different operating cases were investigated. Both of the pressure drops inside the heat exchanger and effectiveness for heat transfer were analyzed. The final results from CFD analysis provide the input parameters for the modeling of the system performance of whole GHP cycle.

Chapter 3 provides a detailed introduction of the ORNL Modulating Heat Pump Design Software, also referred to as MODCON, which is used for the system modeling of GHP cycle. All of basic theory and principle of the MODCON as well as the modeling procedure are provided in this chapter.

Chapter 4 discusses the results from three different GHP cycle models, which include the baseline system for heating and cooling without considering the suction line heat exchanger and heat recovery, the heat performance of the system considering suction line heat recovery and the cooling performance including the suction liquid line heat exchanger. A parametric study has been provided to get the optimal operating condition for the whole GHP system.

Chapter 5 shows the experimental data which were found in tests conducted in a psychrometric test facility at Oak Ridge National Heat pump Laboratory. The experimental data were compared with the system modeling data. Good agreement has been reached.

Chapter 6 discusses the energy saving as well as CO_2 emission with comparing the improved GHP system with the commercially available electrical DX heat pump. Chapter 7 concludes the current research and provides suggestions for future work.

CHAPTER 2

NUMERICAL EVALUATION OF HEAT EXCHANGER

2.1. Description of the Problem and Methodology

Computational fluid dynamics (CFD) is used to simulate the flows through the shell and tube type heat exchanger for the following cases:

A. performance evaluation of a shell and tube type heat exchanger in recovering heat from internal combustion (IC) engine (exhaust and coolant) to augment the heat pump heating mode

B. operation performance evaluation of a liquid to suction refrigerant heat exchanger.

The primary objective of the first part) is to study the design of the heat exchangers to improve system performance during heating and cooling operations with refrigerant R-410a and ethylene glycol as the working fluids. The system's performance is evaluated as a function of the operating conditions. Subsequently, it is also the intent of this study that the methodology detailed in this work provides guidelines to the heat exchanger designer for future design optimizations of this type.

One of the main disadvantages of an electric driven heat pump is that during winter operation, the heating capacity decreases with the ambient temperature. At the same time, building heating loads increase, and under some conditions supplemental heat is required to keep the temperature of the conditioned space at a comfortable level. Typically,

auxiliary electric (resistance) heat strips are added which significantly increase the electric power usage and cost during cold winter operations. Utilizing an internal combustion (IC) engine in lieu of an electric motor for a heat pump system eliminates the need for supplemental heat. The excess heat of combustion generated is available for wintertime heating augmentation, thus reducing or eliminating the need for auxiliary heaters. This energy recovery significantly reduces running costs, while providing stable comfort conditions.

While the advantages of using waste heat from a combustion engine are well recognized, the wide range of options for recovery and use of waste heat has required numerous separate components for heat exchange, auxiliary heating, defrosting, and heat rejection to the ambient.

The complexity, size and cost of these heat pump systems with effective heat recovery have increased accordingly. The purpose of this study is to investigate a readily available, cost effective, shell and tube type heat exchanger performance in transferring the recovered IC heat to the refrigerant. The heat is transferred from the engine coolant to the suction stream of the refrigerant. A schematic of heat recovery process during heating mode is shown in Figure 2.1.

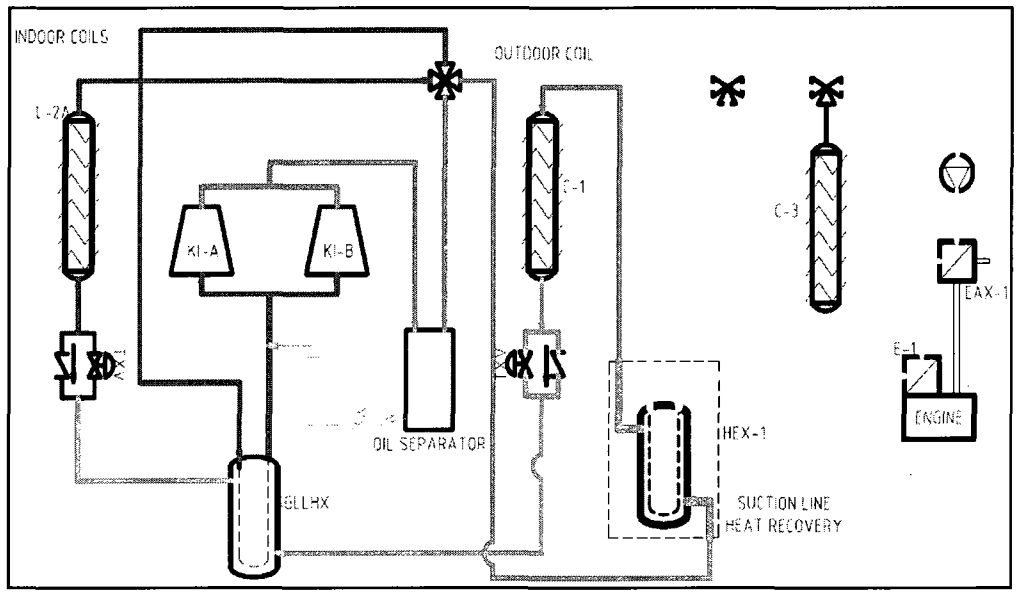

Figure 2.1 Heat Recovery at Refrigerant Suction Line

The second part of this study focuses on performance evaluation of liquid-suction heat exchangers. Liquid-suction heat exchangers are commonly installed in refrigeration systems with the intent of ensuring proper system operation and increasing system performance. Specifically, ASHRAE 1998 [31] states that liquid-suction heat exchangers are effective in:

A. increasing the system performance

B. subcooling liquid refrigerant to prevent flash gas formation at inlets to expansion devices

C. fully evaporating any residual liquid that may remain in the liquid-suction prior to reaching the compressor(s)

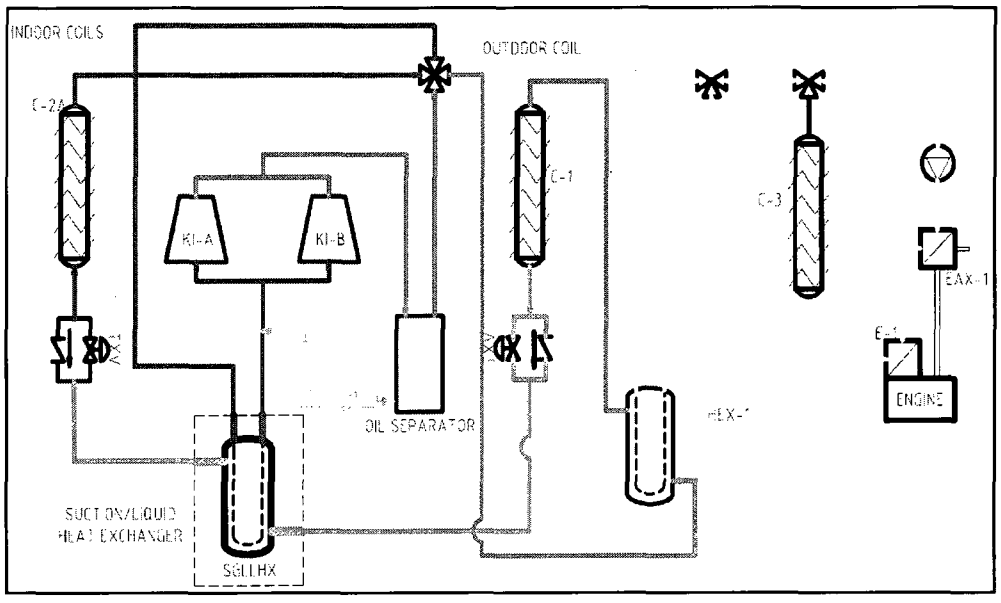

Figure 2.2 Liquid-Suction Refrigerant Heat Exchangers

Figure 2.2 illustrates a simple engine driven direct-expansion vapor compression refrigeration system utilizing a liquid-suction heat exchanger. In this configuration, high temperature liquid leaving the heat rejection device (an evaporative condenser in this case) is subcooled prior to being throttled to the evaporator pressure by an expansion device such as a thermostatic expansion valve. The sink for subcooling the liquid is low temperature refrigerant vapor leaving the evaporator. Thus, the liquid-suction heat exchanger is an indirect liquid-to-vapor heat transfer device.

Although previous researchers have investigated performance of liquid-suction heat exchangers, this study can be distinguished from the previous studies in the following ways:

A. The conclusion of most of the literature surveyed was that the improvement is highly dependent on the type of the refrigerant used in this study the newly adapted refrigerant R410A is investigated.

B. The analysis includes the impact of pressure drops through the liquid-suction heat exchanger on system performance.

C. The ability of a heat exchanger to transfer energy from the warm liquid to the cool vapor at steady-state conditions is dependent on the size and configuration of the heat transfer device. The liquid-suction heat exchanger performance, expressed in terms of effectiveness, is a parameter in the analysis.

D. The liquid-suction heat exchanger affects the performance of a refrigeration system by influencing both the high and low pressure sides of a system. Figure 2.3 shows the key state points for a vapor compression cycle utilizing an idealized liquid-suction heat exchanger on a pressure enthalpy diagram. The enthalpy of the refrigerant leaving the condenser (state 3) is decreased prior to entering the expansion device (state 4) by rejecting energy to the vapor refrigerant leaving the evaporator (state 1) prior to entering the compressor (state 2). Pressure losses are not shown.

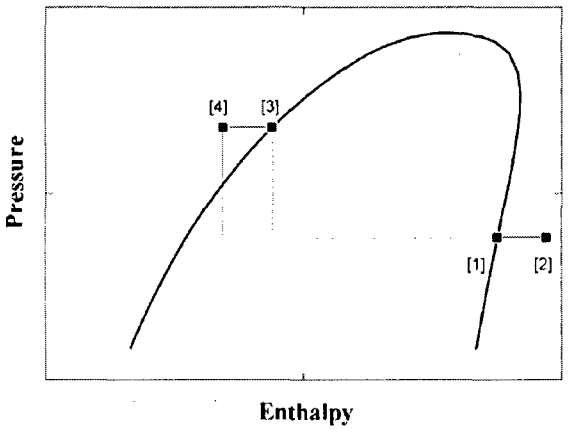

Figure 2.3 Key State Points for a Vapor Compression Cycle

The cooling of the condensate that occurs on the high pressure side serves to increase the refrigeration capacity and reduce the likelihood of liquid refrigerant flashing prior to reaching the expansion device. On the low pressure side, the liquid-suction heat exchanger increases the temperature of the vapor entering the compressor and reduces the refrigerant pressure, both of which increases the specific volume of the refrigerant and thereby decreases the mass flow rate and capacity. A major benefit of the liquid-suction heat exchanger is that it reduces the possibility of liquid carry-over from the evaporator, which could harm the compressor. Liquid carry over can be readily caused by a number of factors that may include wide fluctuations in evaporator load and poorly maintained expansion devices.

The ability of a heat exchanger to transfer energy from the warm liquid to the cool vapor at steady-state conditions is dependent on the size and configuration of the heat transfer device. The liquid-suction heat exchanger performance, expressed in terms of effectiveness, is a parameter in the analysis.

2.2. Operating Condition for Shell-Tube Heat Exchanger

As shown in Figure 2.4, the straight-tube heat exchanger with one pass tube side was selected to evaluate system performance during heating and cooling operations with refrigerant R-410a and ethylene glycol as the working fluids. Copper is used as solid material for the shell and tube. Here, only half of the heat exchanger is shown.

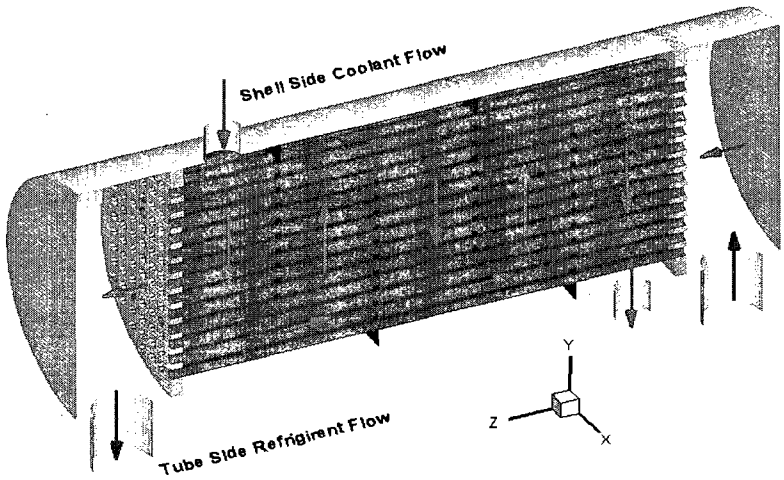

Figure 2.4 Schematical of Shell-Tube Heat Exchanger

This type of shell-tube heat exchanger is the most common type of heat exchanger in oil refineries and other large chemical processes, and it is suited for higher-pressure applications. As shown in Figure 2.4, it consists of a shell (a large pressure vessel) with a bundle of tubes inside it. Two fluids, of different starting temperatures, flow through the heat exchanger. One flows through the tubes (the tube side) and the other flows outside the tubes but inside the shell (the shell side). Heat is transferred from one fluid to the other through the tube walls, either from tube side to shell side or vice versa.

In this study, the fluid in the tube sides is vapor refrigerant R410A while the shell side fluid is aqueous ethylene glycol (50/50% by volume) or liquid refrigerant R410A. It is assumed that the phase of the fluids in the tube side and shell side do not change during the heat transfer process. In order to transfer heat efficiently, a total of 145 tubes was designed to obtain the large heat transfer area. The detailed dimension information of this shell-tube heat exchanger is listed in Table 2.1.

Table 2.1. Dimensions of Shell-Tube Heat Exchanger

Description	**Dimension (in)**
Length of the exchanger	22.500
Diameter of Shell	9.000
Diameter of Inner Tube	0.375
Length of Inner Tube	16.500
Diameter of Inlet of Tube Side	1.125
Diameter of Outlet of Tube Side	1.125
Diameter of Inlet of Shell Side	1.875
Diameter of Outlet of Shell Side	1.875
Distance between Baffle	1.875
Height of Baffle	6.000
Thickness of Tube sheet	0.375

Table 2.2 lists the operating conditions of the shell-tube heat exchanger. Here, seven cases were investigated to obtain the optimal operating mode. For the first four cases, the operating fluids in tube side (vapor refrigerant R410 A) and shell side (aqueous ethylene glycol) keep the same while the inlet temperature and mass flow rate are for the tube and shell side are changed in different cases. For the last three cases, the operating fluids in the shell side are changed into liquid refrigerant R410A. The operating pressure for the vapor refrigerant R410A is 100 psi.

Table 2.2. Operating Conditions of the Shell-Tube Heat Exchanger

Case ID	Operating Fluids	Fluid Inlet	Inlet Temperature °F	Refrigerant Flow Rate (lb/hr)	Glycol Flow Rate (gpm)
Case 1	Vapor R410A	Tube side	40	2000	N/A
	Ethylene glycol (50/50 by vol.)	Shell side	165	0	10
Case 2	Vapor R410A	Tube side	20	1200	N/A
	Ethylene glycol (50/50 by vol.)	Shell side	165	0	10
Case 3	Vapor R410A	Tube side	40	1400	0
	Ethylene glycol (50/50 by vol.)	Shell side	165	0	10
Case 4	Vapor R410A	Tube side	40	1400	N/A
	Ethylene glycol (50/50 by vol.)	Shell side	165	0	5
Case 5	Vapor R410A	Tube side	50	2000	0
	Vapor R410A	Shell side	100	2000	0
Case 6	Vapor R410A	Tube side	50	2000	0
	Liquid R410A	Shell side	120	2000	0
Case 7	Vapor R410A	Tube side	50	2000	0
	Liquid R410A	Shell side	130	2000	0

Table 2.3 shows the thermal properties for the operating fluids. It is noted that the vapor refrigerant R410A has very small conductivity, which results low heat exchange in the fluids between the tube side and shell side.

Table 2.3. Thermal Properties for the Operating Fluids

Fluid Type	Phase	Specific Heat	Density	Dynamic Viscosity	Thermal Cond.
		$\frac{Btu}{lb^{\circ}F}$	$\frac{lb}{ft^3}$	(cP)	$\frac{Btu}{hr \cdot ft \cdot ^{\circ}F}$
Vapor Refrigerant R410A	Vapor	0.2061	-	0.01341	0.0068
Liquid Refrigerant R410A	Liquid	0.5967	57.5997	0.125	0.0443
Ethylene glycol (50/50% by volume)	Liquid	0.85	64.9251	1.0036	0.24

2.3. Governing Equations of Fluid Flow and Heat Transfer

According to the inlet tube-side mass flow rate for the vapor refrigerant R410A, the Reynolds number of flow in tube side is over than 10,000, therefore the flow mode inside the heat exchanger is turbulent. For the turbulent flow, the velocities and temperature can be divided into a mean and a fluctuating value, $u_j = U_j + u_j^{'}$ and $t = T + T^{'}$. Then the governing time-averaged partial differential equations for conservation of gas phase mass momentum, and energy are:

Continuity equation:

$$\frac{\partial \rho u_j}{\partial x_j} = 0 \tag{2.1}$$

Momentum equation:

$$\frac{\partial}{\partial x_j}\left(\rho U_i U_j\right) = -\frac{\partial P}{\partial x_i} + \frac{\partial}{\partial x_j}\left[\mu\left(\frac{\partial U_i}{\partial x_j} + \frac{\partial U_j}{\partial x_i}\right) - \rho\overline{u'_i u'_j}\right] - \rho g_i \tag{2.2}$$

Energy equation:

$$\frac{\partial}{\partial x_j}\left(\rho u_j C_p T\right) = \frac{\partial}{\partial x_j}\left(\lambda\frac{\partial T}{\partial x_j} - \rho\overline{u'_j T'}\right) \tag{2.3}$$

where ρ is the density, μ is the viscosity, p is the pressure, C_p is the specific heat capacity, λ is the thermal conductivity. The turbulent stress and heat flux are determined by

$$\rho\overline{u'_i u'_j} = \mu_t\left(\frac{\partial U_i}{\partial x_j} + \frac{\partial U_j}{\partial x_i}\right) - \frac{2}{3}\rho\delta_{ij}k \tag{2.4}$$

$$\rho\overline{u'_j T} = \frac{\mu_t}{\mathrm{Pr}_t}\frac{\partial T}{\partial x_j} \tag{2.5}$$

where δ_{ij} is the Kronecker delta function, $\delta_{ij} = 1$ when $i = j$ and zero when $i \neq j$, k is the turbulent kinetic energy, Pr_t is the turbulent Prandtl number and taken as 0.9, and μ_t is the turbulent viscosity, $\mu_t = \rho C_\mu k^2/\varepsilon$, where $C_\mu = 0.09$ and ε is the turbulence dissipation.

As the simplest two-equation turbulence models in which the solution of two separate transport equations, the standard $k-\varepsilon$ model are used in heat exchanger calculation and it allows the turbulent velocity and length scales to be independently determined. The standard $k-\varepsilon$ model has become the workhorse of practical engineering flow calculations in the time since it was proposed by Launder and Spalding [41]. Robustness,

economy, and reasonable accuracy for a wide range of turbulent flows explain its popularity in industrial flow and heat transfer simulations. It is a semi-empirical model, and the derivation of the model equations relies on phenomenological considerations and empiricism.

The standard $k-\varepsilon$ model is a semi-empirical model based on model transport equations for the turbulence kinetic energy (k) and its dissipation rate (ε). The model transport equation for k is derived from the exact equation, while the model transport equation for ε was obtained using physical reasoning and bears little resemblance to its mathematically exact counterpart.

In the derivation of the $k-\varepsilon$ model, the assumption is that the flow is fully turbulent, and the effects of molecular viscosity are negligible. The standard $k-\varepsilon$ model is therefore valid only for fully turbulent flows. The governing equations of the turbulence kinetic energy (k) and its dissipation rate (ε) for steady state of turbulent flow are shown as follows.

$$\frac{\partial}{\partial x_i}(\rho k u_i) = \frac{\partial}{\partial x_j}\left[\left(\mu + \frac{\mu_t}{\sigma_k}\right)\frac{\partial k}{\partial x_j}\right] + G_k + G_b - \rho\varepsilon - Y_M + S_k \tag{2.6}$$

$$\frac{\partial}{\partial x_i}(\rho \varepsilon u_i) = \frac{\partial}{\partial x_j}\left[\left(\mu + \frac{\mu_t}{\sigma_\varepsilon}\right)\frac{\partial \varepsilon}{\partial x_j}\right] + C_{1\varepsilon}\frac{\varepsilon}{k}(G_k + C_{3\varepsilon}G_b) - C_{2\varepsilon}\rho\frac{\varepsilon^2}{k} + S_\varepsilon \tag{2.7}$$

where:

ρ = density of air

k = turbulence kinetic energy

ε = rate of dissipation

x_i , x_j = coordinate

u_i = mean velocity

μ = viscosity

μ_t = turbulent viscosity

σ_k , σ_ε = turbulent Prandtl number for k and ε

G_k = generation of turbulence kinetic energy due to the mean velocity gradients

G_b = generation of turbulence kinetic energy due to buoyancy

Y_M = contribution of the fluctuating dilatation in compressible turbulence to the overall dissipation rate

S_k , S_ε = user-defined source terms

$C_{1\varepsilon}$ $C_{2\varepsilon}$ $C_{3\varepsilon}$ = constant.

The model constants $C_{1\varepsilon}, C_{2\varepsilon}, C_{3\varepsilon}, \sigma_k$ and σ_ε have the following default values:

$$C_{1\varepsilon} = 1.44\,,\ C_{2\varepsilon} = 1.92\,,\ C_{3\varepsilon} = 0.09\,,\ \sigma_k = 1.0\,,\ \sigma_\varepsilon = 1.3$$

These default values have been determined from experiments with air and water for fundamental turbulent shear flows including homogeneous shear flows and decaying isotropic grid turbulence. They have been found to work fairly well for a wide range of wall-bounded and free shear flows.

In this study, the vapor refrigerant R410A in the tube side is treated as incompressible ideal gas. Buoyancy-driven convection (i.e., gravitational effects) is based on an ideal gas equation, which is defined in the following equation.

$$\rho = \frac{p_{op}}{\frac{R}{M_w}T} \tag{2.8}$$

where:

ρ = density

P_{op} = operating pressure

R = universal gas constant

M_w = molecular weight of the gas

This directly couples the momentum equation to the energy equation at every location in the vapor refrigerant R410A domain to account explicitly for the effects of temperature change on the vapor refrigerant R410A density.

2.4. Numerical Method and Mesh System

The governing equations are solved in the Cartesian coordinate system using a control volume finite difference method. A non-staggered grid storage scheme is adapted to define the discrete control volumes. In this scheme, the same control volume is employed for the integration of all conservation equations. All variables are stored at the control volume's cell center. The numerical scheme used in this study is a power-law differencing scheme, and the solver used is a segregated solver (Figure 2.5).

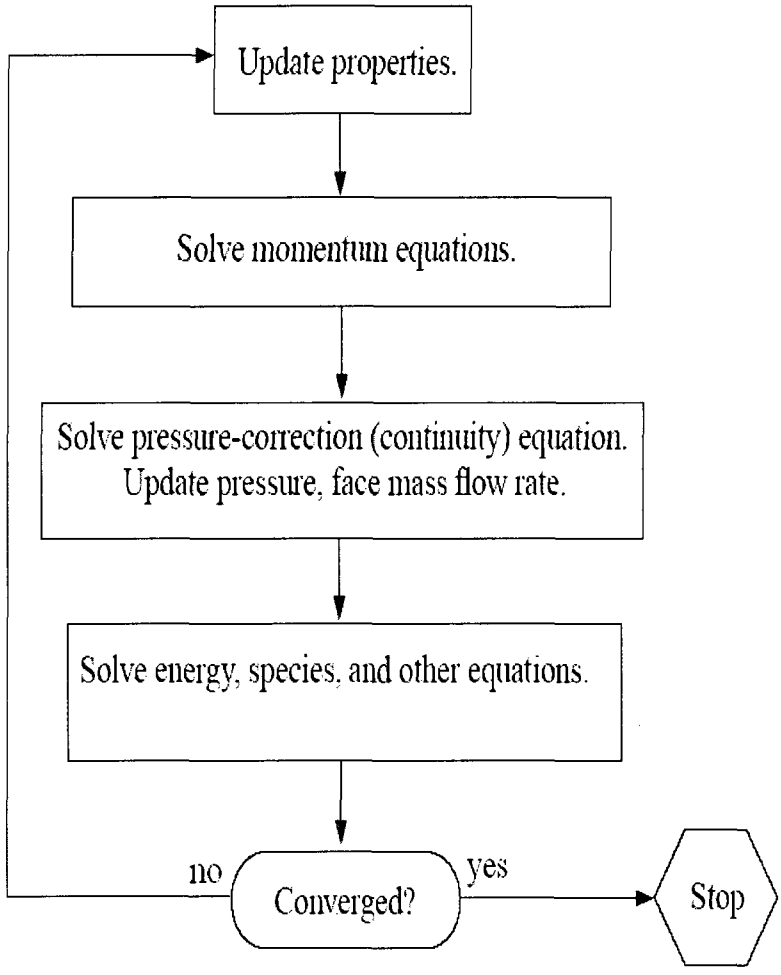

Figure 2.5 Iterative Solution Method for the Segregate Solver

SIMPLE (semi-implicit method for pressure-linked equations) algorithm is used to resolve the coupling between pressure and velocity. The governing equations, which are discrete and nonlinear, are linearized using an implicit technique with respect to a set of dependent variables. The resulting algebraic equations are solved iteratively using an additive correction multigrid method with a Gauss-Seidel relaxation procedure.

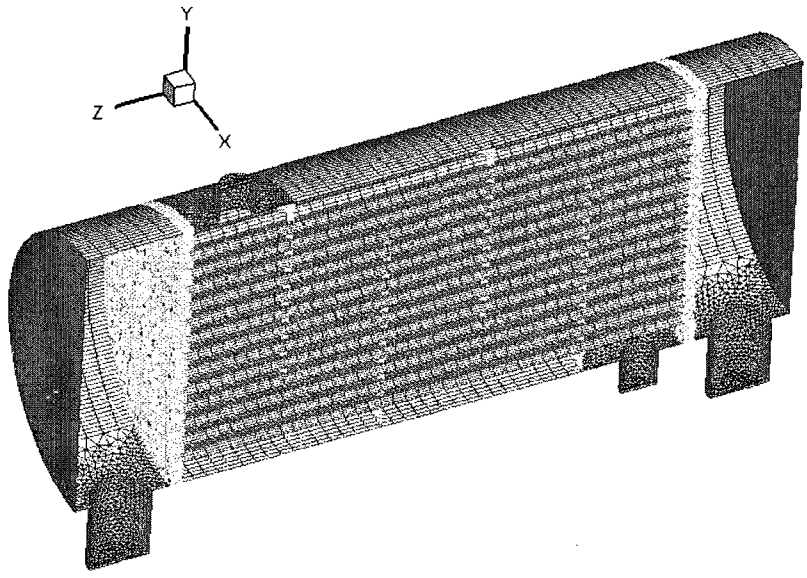

(a) Full view

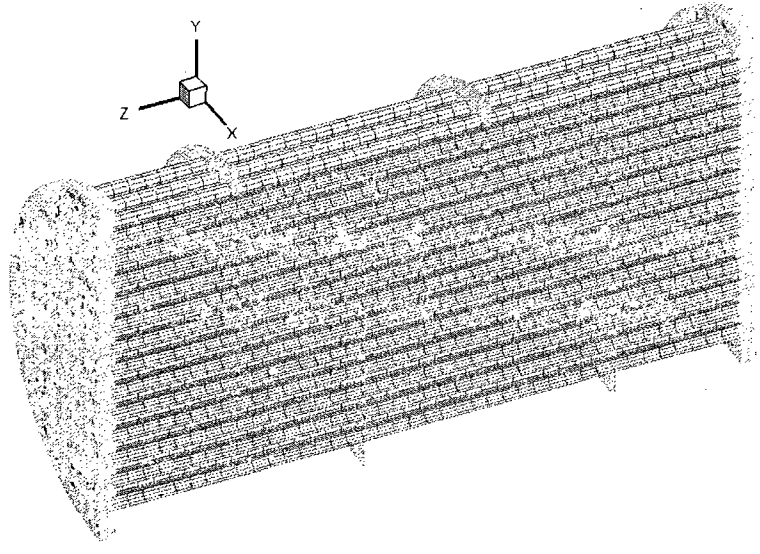

(b) inside view

Figure 2.6 Mesh System of Shell-Tube Heat Exchanger

As indicated above, to solve the governing equation, the computational domain for the heat exchanger must be discretized into the finite control volume cell. Figure 2.6 shows the mesh system for the shell-tube heat exchanger. Due to the symmetry of the geometry of the system, only half of shell-tube heat exchanger is considered to save the CPU time. The grid independence studies are performed to check the dependence of the calculated parameters (pressure, temperature and velocities) on mesh size. The grids systems are refined until the calculated parameters became independent from the grid size. The final meshes used in this calculation are 264964 mixed cells with 379894 nodes.

2.5. Fluid flow and Temperature Distribution Analysis

To illustrate the fluid flow inside the shell-tube heat exchanger, the path lines released from the tube-side and shell side are shown in Figure 2.7. The flow structures and temperature distributions inside the shell-tube heat exchanger are similar in all the cases. Here, only the simulation results of fluid flow and temperature for case 1 are illustrated. In Figure 2.7 Pathlines Released from Inlet of Tube Side and Shell Side., the pathlines are colored by the velocity magnitude and temperature. As shown in Figure (a), there is a pair of vorticies generated inside the tube-side chamber which connects tube-side inlet due to the large injection velocity of vapor Refrigerant R410A. While in operation, the major heat exchange occurs between the vapor refrigerant R410A flow and the aqueous ethylene glycol flow at the inner tube walls during the period that vapor refrigerant R410A flow through the inner tube. To increase the residence time of the shell-side aqueous ethylene glycol, a baffle plate is used for the design of shell-tube heat exchanger. Meanwhile, the use of a baffle will also result in larger pressure drop in the shell-side.

Figure 2.7(b) shows the pathlines colored by the temperature. As the vapor Refrigerant R410A flows through the inner tubes, the temperature increases gradually and the final temperature difference between inlet and outlet is around 30°F. In the shell-side, a 7°F temperature drop is noted for the aqueous Ethylene Glycol.

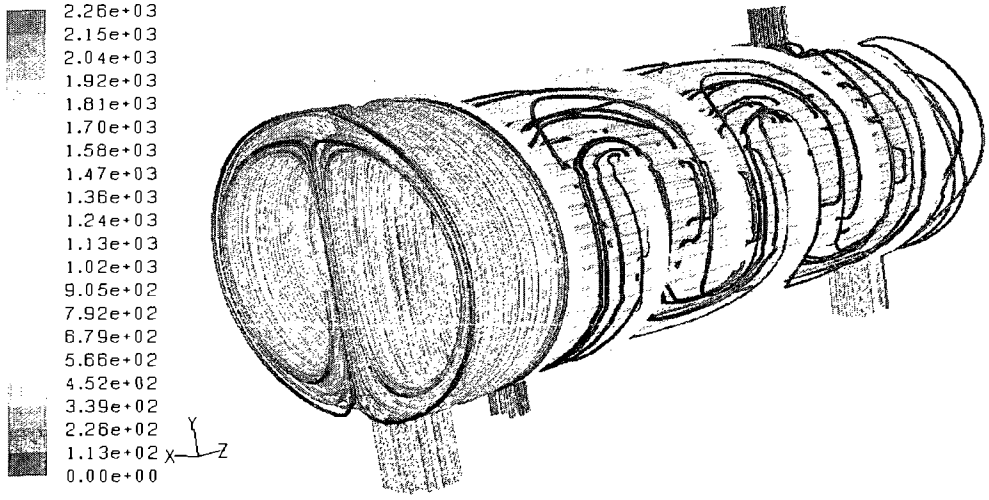

(a) colored by velocity magnitude (fpm)

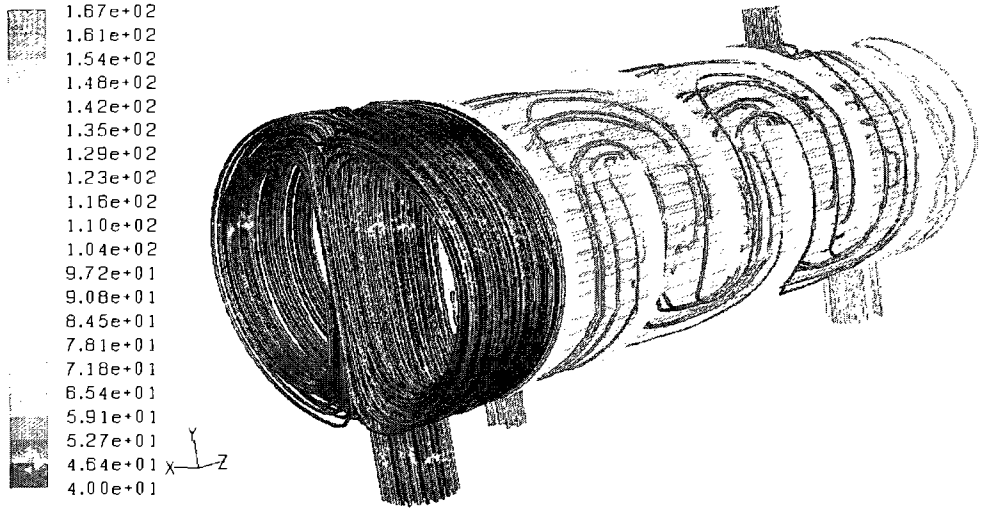

(a) colored by temperature (°F)

Figure 2.7 Pathlines Released from Inlet of Tube Side and Shell Side.

Figure 2.8 illustrates the pressure drop (psi) on the symmetry plane. According to the pressure distribution, an approximate 0.6 psi pressure drop can be found on the tube side. The reason for the high pressure drop in the tube-side is that the size of inner tube size is relative small. The highest pressure occurs at the top wall of tube-side injection chamber. For the shell side, the pressure drop is less than 0.1 psi. According to design baseline for the shell-tube heat exchanger, the maximum pressure drop is still in the acceptable range.

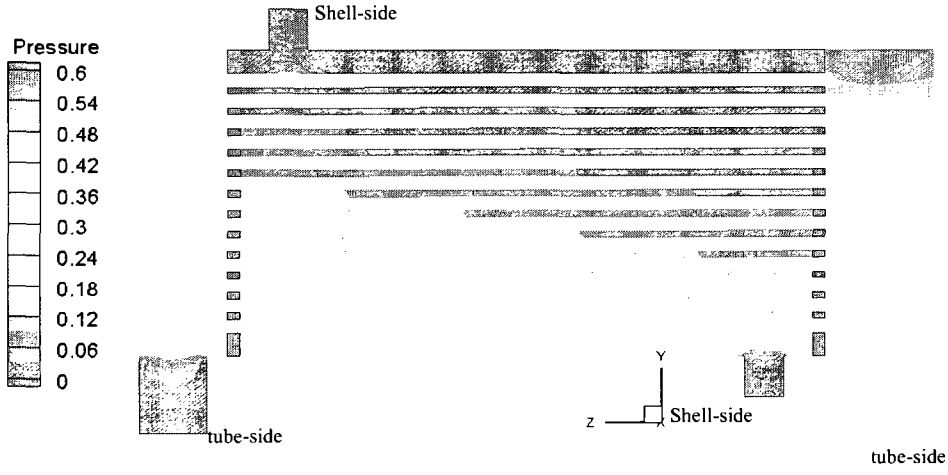

Figure 2.8 Pressure (psi) Distribution on the Symmetry Plane

To show the detailed flow, temperature and pressure distribution, the simulation results for the selected slices are extracted out, as shown in Figure 2.9. Here, the slices for cross-section at the tube-side inlet (Slice A), shell side outlet (Slice B), shell side inlet (Slice C), and tube-side outlet (Slice D) are selected for investigation.

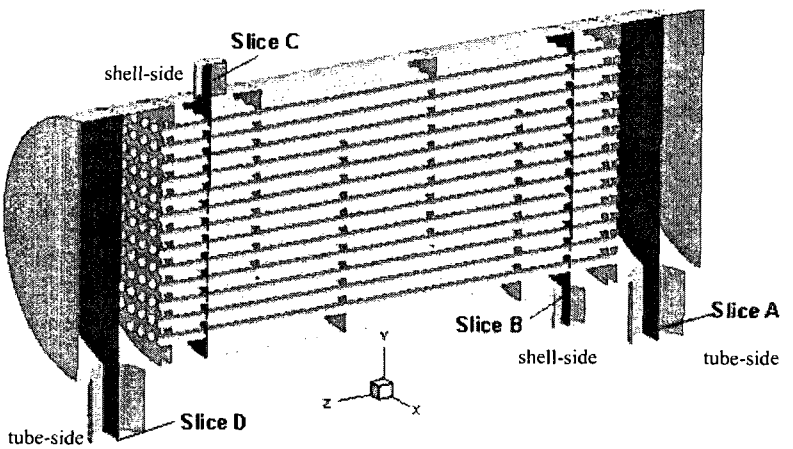

Figure 2.9 Schematic of Selected Slice Inside the Heat Exchanger.

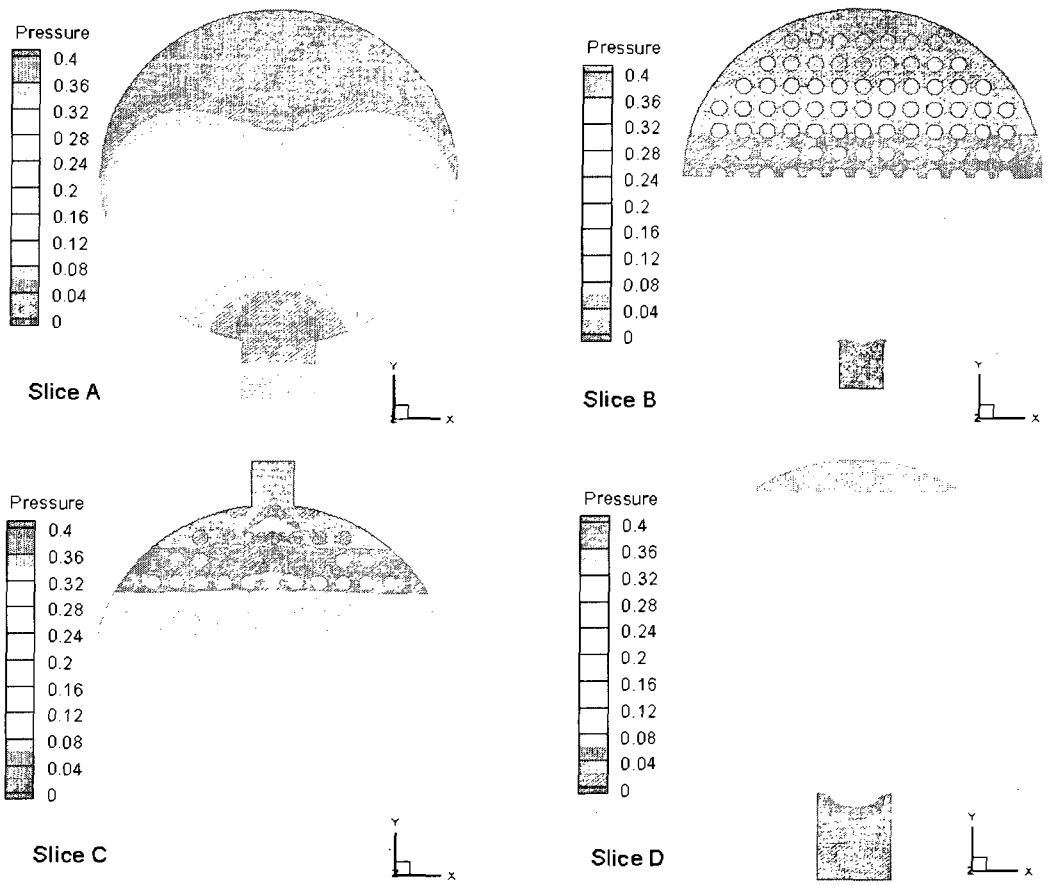

Figure 2.10 Pressure (psi) Distributions at Selected Slices

Figure 2.10 shows the pressure (psi) distributions at the selected slices. For the tube-side vapor refrigerant R410A, the higher pressure occurs at the top region of the heat exchanger while the pressure for the shell side aqueous Ethylene glycol at the bottom region is higher than the top region.

Figure 2.11 illustrates the velocity magnitude (fpm) distribution at the different slices. As shown in the figures, it can be found that the velocity magnitude for the tube side refrigerant R410A is much larger than that of shell side aqueous Ethylene Glycol. Due the generation of vortex at inlet region for the vapor refrigerant R410A, the maximum velocity can be found at the inlet chamber while the tube side flow inside the inner tube is much smaller.

Considering that the pressure distribution at the inlet of tube is different, the velocity magnitude is not uniform in each tube, which corresponds to different mass flow rate for the tubes. According to the figures, it can be found the mass flow rates at the top and bottom region is higher than that at the middle region. Hence, it is expected that the vapor refrigerant R410A flow inside the tubes at the middle region will have higher temperature.

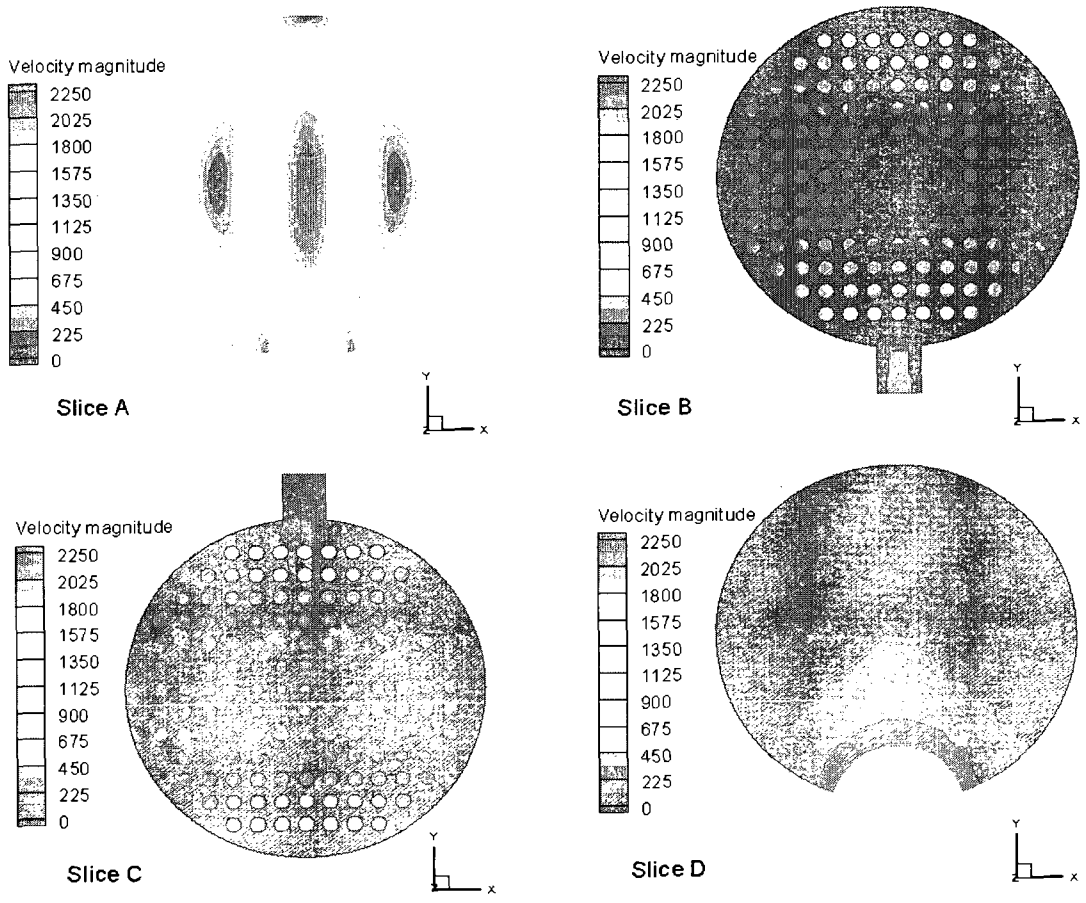

Figure 2.11. Velocity Magnitude (fpm) Distribution on the Selected Slices

Figure 2.12 illustrates the temperature distributions at the different selected slices. At the inlet chamber (Slice A), the temperature stays almost the same as the inlet temperature. As the vapor refrigerant R410 flow through the inner tube, it is heated up gradually. Due to non-uniformity of mass flow rate of the tubes, the vapor flow at the middle region is higher than that at the top and bottom region. Compared with the temperature of vapor refrigerant R410A, the temperature for the aqueous Ethylene glycol does not change too much due to the high specific heat. As shown in slice B and slice C, there still exists big temperature difference between the tube side fluid and shell side

fluids. The reason for this is that the thermal conductivity of the vapor is very small ~0.0068 $\left(\frac{Btu}{hr \cdot ft \cdot {}^{o}F}\right)$, which results in low heat transfer exchange rate between the tube side fluids and shell side fluids.

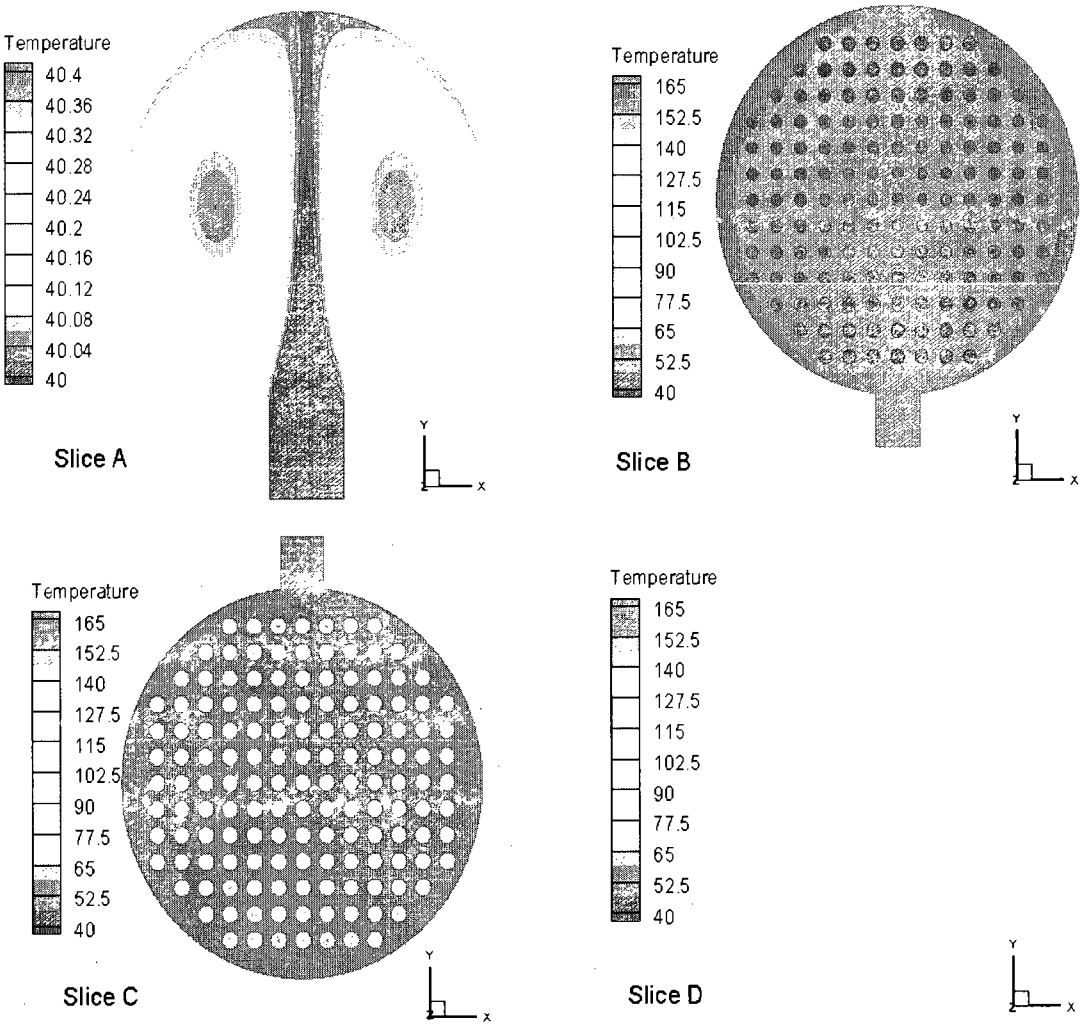

Figure 2.12. Temperature (^{o}F) Distributions on the Selected Slices

2.6. Thermal Performance Evaluation

Table 2.4 lists the summary of simulation results for different operating condition. The effectiveness inside the table is defined by

$$E = \frac{(T_{vapor,out} - T_{vapor,in})}{(T_{liquid,in} - T_{vapor,in})} \tag{2.9}$$

where:

E is the effectiveness of the shell-tube heat exchanger

$T_{vapor,out}$ is the vapor outlet temperature of tube side

$T_{vapor,in}$ is the vapor inlet temperature of tube side

$T_{liquid,in}$ is the liquid inlet temperature of shell side

Table 2.4 Summary of Simulation Results for Different Cases

ID	Pressure Drop (Psi)		Heat Exchange (Btu/hr)	Inlet Temperature (F)		Outlet Temperature (F)		E
	Tube	Shell	Total	Tube	Shell	Tube	Shell	
1	0.32	0.03	31680	40	165	78.2	155.2	0.306
2	0.15	0.03	25905	20	165	74.9	157	0.379
3	0.21	0.03	25783	40	165	82.9	157	0.343
4	0.21	0.13	24594	40	165	81.7	149.8	0.333
5	0.3	0.14	10226	50	100.1	63.7	90	0.273
6	0.3	0.14	14935	50	120	67.7	106.3	0.253
7	0.3	0.14	24594	50	130	69.4	115.6	0.242

According to Table 2.4, the pressure drop on the tube side is much larger than that on the shell side. The pressure drop in Case 1 is biggest, which is 0.32 psi. The Case 1 also has the highest heat exchange, which is 31680 Btu/hr. Case 2 has the highest improved temperature for the tube side, which is 54.9 ^{o}F. As found in the table, the effectiveness for the heat exchanger for all the cases is relatively small, which is around 30%.

The major reason for the small effectivenesses is that the thermal conductivity of vapor refrigerant R410A is very small. Among these cases, the Case 2 has the largest effectiveness, which is 0.379. Case 5 has the lowest heat exchange and temperature change at the tube side. Although the effectiveness of the shell tube exchanger is small, the goal of this numerical study still has been reached and over 30,000 Bu/hr has been obtained at cases.

CHAPTER 3

GHP SYSTEM MODEL

3.1. Modeling Program

The heat pump cycle is modeled using ORNL Modulating Heat Pump Design Software. The ORNL Modulating Heat Pump Design Tool consists of a Modulating HPDM (Heat Pump Design Model) and a parametric-analysis (contour-data generating) front-end. Collectively the program is also referred to as MODCON which is in reference to the modulating and the contour data generating capabilities. The program was developed by Oak Ridge National Laboratory for the Department of Energy to provide a publicly-available system design tool for variable- and single speed heat pumps. The current model has evolved from programs written at ORNL [42, 43] and at the Massachusetts Institute of Technology [44]. It also makes use of selected routines by Kartsounes and Erth [45], Flower [46], and Kusuda [47]. The philosophy of the model development has been to base the program on underlying physical principles and generalized correlations to the greatest extent possible, so as to avoid the limitations of empirical correlations derived from manufacturers' literature.

MODCON predicts the steady-state heating and cooling performance of variable-speed vapor compression air-to-air heat pumps for a wide range of system configuration and operational variables. The user can generate steady-state performance data sets at

fixed ambient or as a function of ambient temperature. The range of selection options includes:

A. 52 design and control variables for parametric analysis,

B. 8 user-defined operational control relationships as functions of compressor speed or ambient temperature, and

C. over 100 possible heat pump model output parameters.

The ORNL Heat Pump Design Model allows the user to specify:

A. System operating conditions, the desired indoor and outdoor air temperatures and relative humidity,

B. Engine and compressor characteristics

- a map-based model,

C. Refrigerant Flow Control Devices

- a capillary tube, thermostatic expansion valve (TXV), or a short-tube orifice, or
- a specified value of refrigerant subcooling (or quality) at the condenser exit (in this case the program calculates the equivalent capillary tube, TXV, and short-tube orifice parameters);

D. Fin-and-Tube Heat Exchanger Parameters

- tube size, spacing, and number of rows, and number of parallel circuits,
- fin pitch, thickness, and thermal conductivity; type of fins (smooth, wavy, or louvered),
- air flow rates;

E. Fan and Indoor Duct Characteristics

- overall fan efficiency values for indoor and outdoor fans, or
- a specified fan efficiency curve for the outdoor fan,
- the diameter of one of six equivalent ducts;

F. Refrigerants

G. Refrigerant Lines

- lengths and diameters of interconnecting pipes,
- pipe specifications independent of heating or cooling mode,
- heat losses from suction, discharge, and liquid lines.

The front-end program allows use of the modulating HPDM to parametrically generate sets of steady-state performance data suitable either for tabulation, for plotting y vs. x for families of x, or for plotting y-contours for ranges of x_1 vs. x_2. The parametric, or contour-data generating, front-end provides an automated means to conduct parametric performance mappings of selected pairs of independent design variables. The user can generate steady-state performance data sets at fixed ambient or as a function of ambient temperature.

3.2. Modeling Procedure for the Vapor Compression Cycle

The vapor compression refrigeration cycle modeled for this study is shown in Figure 3.1. As the figure shows, low pressure, superheated refrigerant vapor from the evaporator enters the compressor (State 1) and leaves as high pressure, superheated vapor (State 2). This vapor enters the condenser where heat is rejected to outdoor air that is forced over the condenser coils.

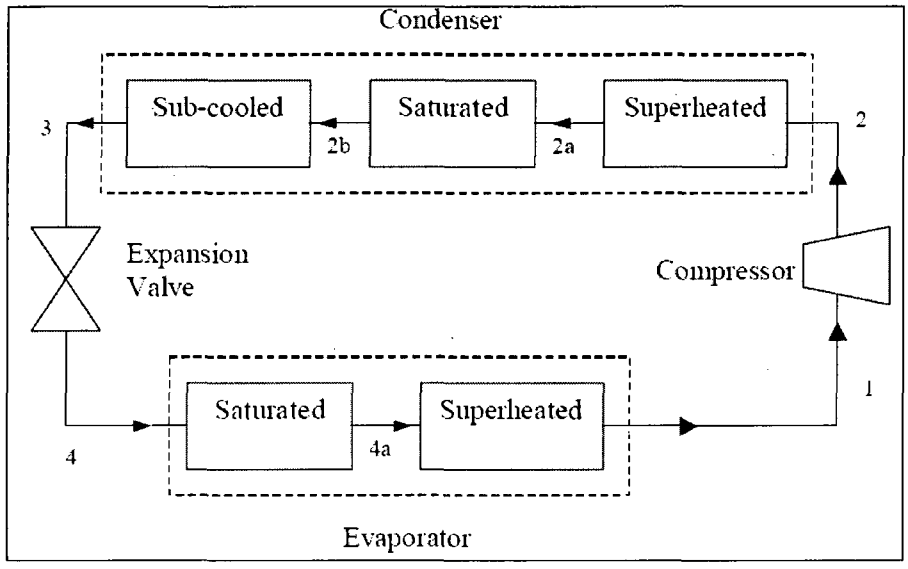

Figure 3.1. Vapor-Compression Refrigeration Cycle

Next the refrigerant vapor is cooled to the saturation temperature (State 2b), and then cooled to below the saturation point until only subcooled liquid is present (State 3). The high pressure liquid is then forced through the expansion valve into the evaporator (State 4). The refrigerant then absorbs heat from warm indoor air that is blown over the evaporator coils. The refrigerant is completed evaporated (State 4a) and heated above the saturation temperature before entering the compressor (State 1). The indoor air is cooled and dehumidified as it flows over the evaporator and returned to the living space.

The heat pump model is organized functionally into two major sections. The first section combines the compressor, condenser, and flow control device routines into an interrelated high-side unit. The second section, the low-side unit, contains the evaporator model. Calculations proceed iteratively between these two sections until the desired overall balance is obtained. The calculation scheme is independent of whether the unit is operating in the heating or cooling mode. Figure 3.2 represents the basic vapor

compression cycle, shown on an exaggerated pressure-enthalpy diagram that is modeled by the program. The user is required to specify:

A. the level of evaporator exit superheat (or quality),

B. design parameters for a flow-control device or the level of

C. condenser exit subcooling (or quality),

D. condenser and evaporator inlet air temperatures,

E. dimensions of components and interconnecting pipes, and

F. heat losses from interconnecting pipes.

The computations for the high-side system balance begin with the refrigerant state at the exit of the evaporator (point 4a Figure 3.2), which is defined by the specified superheat and the estimate of the saturation temperature.

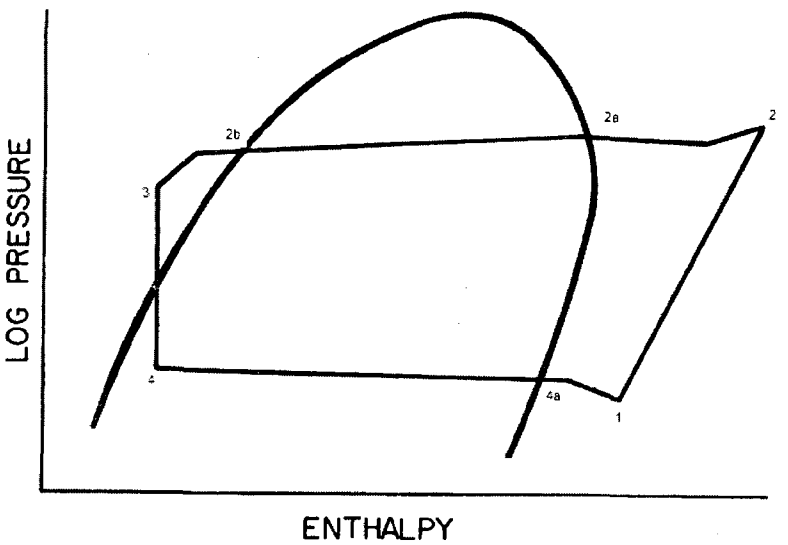

Figure 3.2. Pressure vs. Enthalpy Diagram for the Heat Pump Cycle

This point remains fixed for one iteration of the compressor, condenser, expansion device, and evaporator calculations. The compressor model uses state point 4a along with:

A. the estimates of the refrigerant mass flow rate and saturation temperature at the condenser inlet, and
B. the specification of the dimensions and heat losses for the suction and discharge lines

to calculate the state at the shell inlet, 1, shell outlet, 2, and the condenser inlet, 2a, as well as a new estimate of the mass flow rate. The remainder of the high-side calculations depends on whether a flow control device has been chosen or if a desired value of condenser exit subcooling (or quality) has been specified. The latter case is described since it is used for this modeling. The condenser sub model uses:

A. the physical description of the heat exchanger,
B. the calculated refrigerant mass flow rate,
C. the condenser inlet air temperature and relative humidity, and
D. the refrigerant state at the condenser inlet, point 2a,

to evaluate the refrigerant state at the condenser outlet, 2b. The level of condenser subcooling is computed from knowledge of state 2b, and compared to the specified value. If the two values do not agree within a fixed tolerance, the saturation temperature at point 2a, is changed (in effect specifying a new condenser entrance pressure), and the compressor and condenser calculations are repeated. Each time the condenser saturation temperature is changed, the compressor model calculates a new refrigerant mass flow rate and new states 1, 2, and 2a and the condenser model updates state 2b. Once the desired

condenser subcooling is achieved, the state at the flow control device, 3, is computed using:

A. the state at the condenser exit, 2a,

B. the dimensions and heat loss for the liquid line, and

C. the most recent calculation of the refrigerant mass flow rate.

Refrigerant state 3 and the mass flow rate are then used to calculate the equivalent capillary tube, TXV, and short-tube orifice parameters that would produce the specified subcooling.

The evaporator, or low-side, computations are based on:

- the refrigerant condition at the evaporator exit, state 4a,
- the refrigerant enthalpy at the evaporator inlet, point 4, and
- the refrigerant mass flow rate.

These values have all been computed based on the estimated saturation temperature and specified superheat (or quality) at the evaporator exit. The saturation pressure at the evaporator inlet, point 4, and the inlet air temperature which would yield the specified superheat at the assumed exit saturation temperature are still unknown. The evaporator model is executed iteratively, varying the inlet air temperature from one execution to the next, to calculate a value of superheat at the evaporator exit and a pressure drop across the heat exchanger (and hence a saturation pressure at the inlet since the exit conditions are fixed).

A system solution has been completed for some evaporator inlet air temperature, though not necessarily the desired one, when the calculated exit superheat agrees with the specified value within a given tolerance. (The high- and low-side loops are repeated once

if a thermostatic expansion valve or a short-tube orifice is specified as the flow control device to ensure that an accurate evaporator inlet pressure is used during the high-side calculations.) The system solution is found for the desired evaporator inlet air temperature by changing the saturation temperature at the evaporator exit, point 4a, and repeating the entire calculation process. This iteration on state point '4a' continues until the computed inlet air temperature agrees with the desired value within a specified tolerance. The sequence of calculations is summarized in Figure 3.3. The evaporator inlet air temperature is nearly a linear function of the exit refrigerant saturation temperature so that usually only one or two iterations over the outermost loop in Figure 3.3 are required.

3.3. Organization of the Computer Program

Subroutines to perform computations are divided into distinct modules. The calculation of the system high-side balance, for example, requires computing the performance of the compressor, condenser, and (optionally) the flow control device and then balancing the output of these components and the interconnecting pipes with each other. This is accomplished in the heat pump model using individual subroutines, one for each task:

A. modeling the compressor

B. modeling the engine

C. modeling the condenser

D. modeling the flow control device

E. iterating on condenser saturation temperature

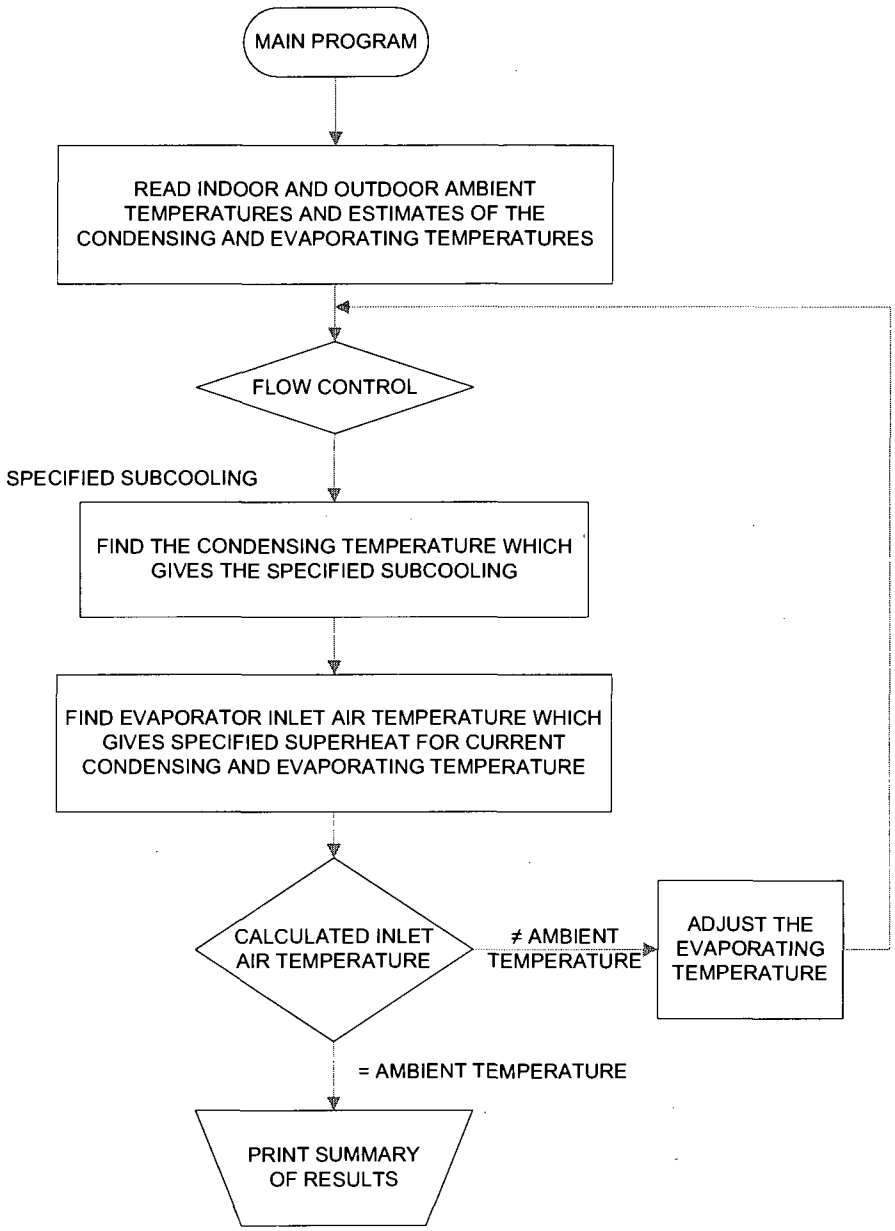

Figure 3.3 Block Diagram of Iterative Loops in the Main Program

3.3.1. Compressor Model

Since the compressor is the heart of a heat pump system and the primary user of power, accurate compressor modeling is important to good system performance prediction. The model is based on the compressor map generated from compressor

calorimeter test data. These performance curves provide compressor power input, refrigerant mass flow rate and/or refrigerating capacity as functions of evaporator saturation temperature (i.e., at compressor shell inlet) for four to six condenser saturation temperatures (i.e., at the compressor shell outlet). Each performance map is generated for fixed values of condenser exit subcooling and compressor inlet superheat. The routine uses curve fits to the compressor power input and the refrigerant mass flow rate as functions of compressor shell inlet and outlet saturation temperatures to model the published performance data.

Mass flow rate and power calorimeter test data for scroll compressors have been collected. These test data are commonly correlated with 10-coefficient polynomials using the method presented in ARI Standard 540 [48] as a function of the saturated evaporator and condenser temperatures. In general, these polynomial representations accurately represent the experimental data. Twenty-one sets of calorimeter test data have been collected on compressors using R-410A (CH_2F_2/CHF_2CF_3) as the refrigerant. The compressors were tested at seventeen different operating conditions (different saturated evaporating and condensing temperatures). The condensing temperatures ranged from 90°F to 140°F and the evaporating temperature ranged from 1.5°F to 53°F. For each evaporating and condensing condition, experimental values of power input and refrigerant mass flow rate given. A method for representing compressor test data is described in [48]. The method uses a bivariate cubic polynomial with cross-terms to describe the mass flow rate and the power input as a function of saturated evaporating and condensing temperatures.

$$F(S,D) = \lambda_1 + \lambda_2 S + \lambda_3 D + \lambda_4 S^2 + \lambda_5 DS + \lambda_6 D^2 + \lambda_7 S^3 + \lambda_8 DS^2 + \lambda_9 SD^2 + \lambda_{10} D^3 \quad (3.1)$$

Where:

$\lambda_1 - \lambda_{10}$ are the map coefficients per [48],

S & D are the compressor suction & discharge saturation temperatures (°F)

Table 3.1 The Ten Coefficients Based on the Polynomial Fit

Compressor Speed				
	2380 rpm		**3400 rpm**	
	$\dot{m}_{map}$	$\dot{W}_{map}$	$\dot{m}_{map}$	$\dot{W}_{map}$
λ_1	3.48E+02	6.18E+02	5.07E+02	5.70E+02
λ_2	2.26E+00	-8.86E+00	3.39E+00	-1.07E+01
λ_3	-3.52E+00	-8.44E+00	-4.93E+00	-3.67E+00
λ_4	5.63E-02	2.86E-01	8.44E-02	3.50E-01
λ_5	4.41E-02	1.04E-01	6.56E-02	1.44E-01
λ_6	3.56E-02	2.85E-01	5.05E-02	3.43E-01
λ_7	-2.16E-04	-2.24E-03	-3.19E-04	-3.09E-03
λ_8	-1.08E-05	-2.10E-03	-1.96E-05	-2.66E-03
λ_9	-1.93E-04	3.53E-06	-2.86E-04	-5.16E-05
λ_{10}	-1.17E-04	-5.97E-04	-1.67E-04	-6.63E-04

Total actual compressor displacement, the rated compressor speed, and the fixed refrigerant superheat or temperature at the compressor shell inlet will be entered as inputs for the compressor which is being modeled. The desired compressor displacement is also an input parameter; this value is used by the map-based model to scale the compressor performance curves linearly to represent a compressor with the same general performance characteristics as the original compressor but of a different capacity. The input power and mass flow rate of the refrigerant are plotted in Figure 3.4 and Figure 3.5 respectively. As shown in Figure 3.4, the input power to the compressor is directly proportional to the refrigerant condensing pressure and engine/compressor speed

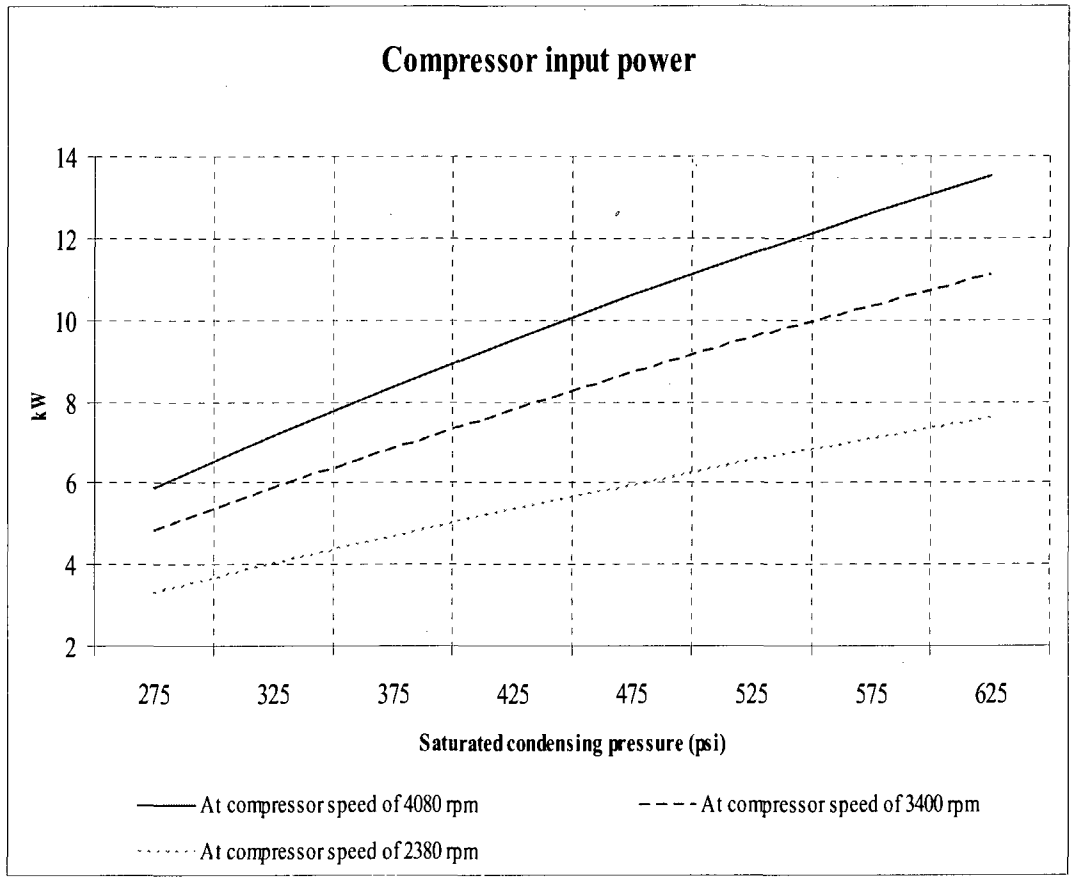

Figure 3.4 Compressor Input Power vs. Condensing Pressure

The refrigerant mass flow rate depends upon the compressor inlet vapor density which is related to the evaporating temperature. As the refrigerant evaporating temperature increases the refrigerant density also increases. Figure 3.5 illustrates the mass flow rate of the refrigerant as function of evaporating pressure at three compressor speed. As the rotational speed of the compressor speed increases the mass flow rate of the refrigerant is also increases.

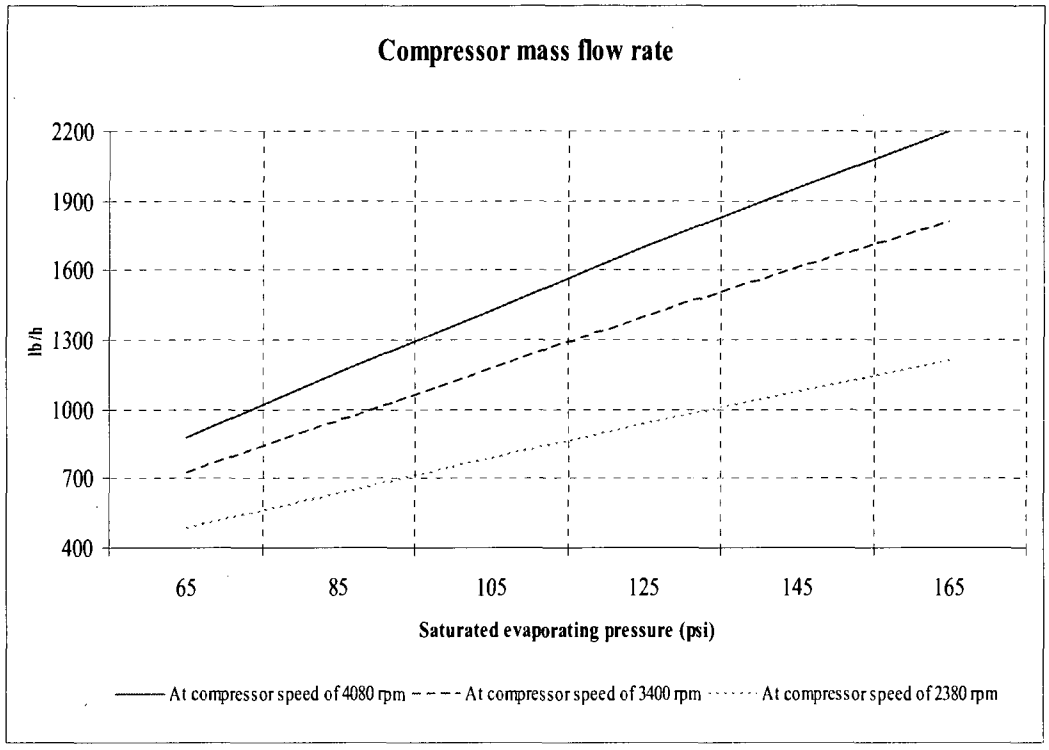

Figure 3.5 Refrigerant Mass Flow Rate vs. Evaporating Pressure

Figure 3.6 shows the refrigerant mass flow rate as a function of condensing and evaporating pressures at engine and compressor speed of 2400 and 4080 rpm respectively.

Total actual compressor displacement, the rated compressor speed, and the fixed refrigerant superheat or temperature at the compressor shell inlet will be entered as inputs for the compressor which is being modeled. The desired compressor displacement is also an input parameter; this value is used by the map-based model to scale the compressor performance curves linearly to represent a compressor with the same general performance characteristics as the original compressor but of a different capacity.

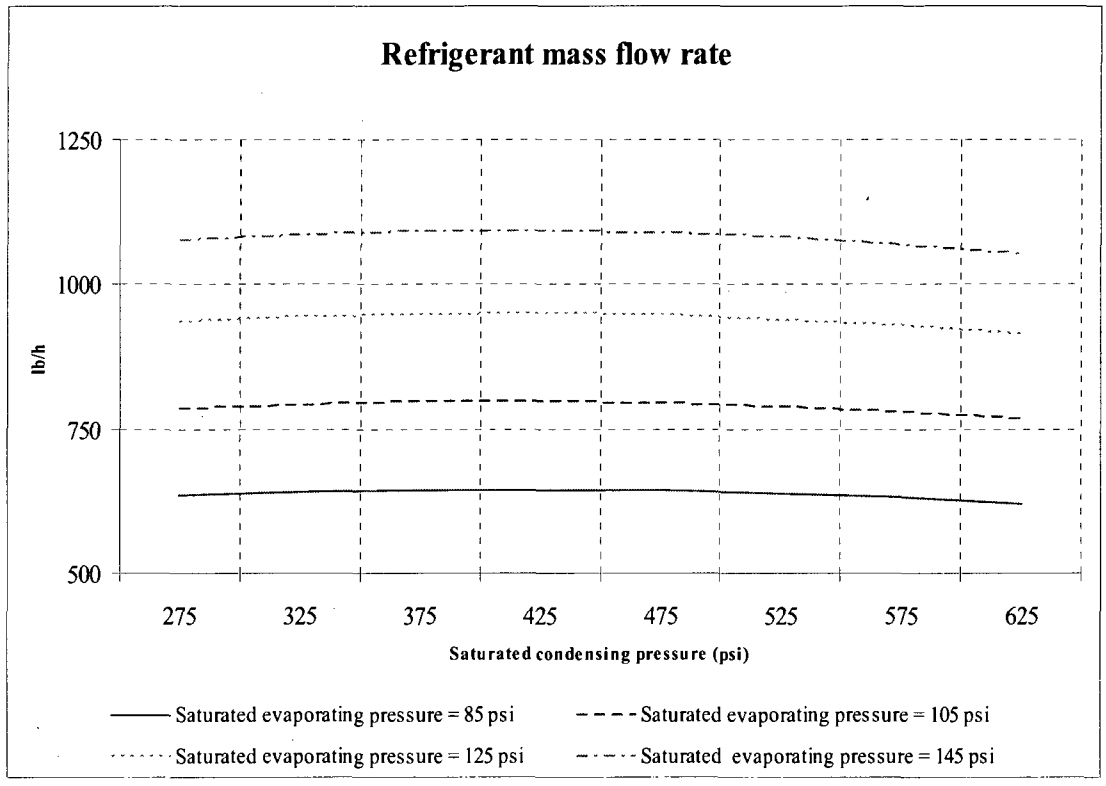

Figure 3.6 Refrigerant Mass Flow Rates vs. Saturated Condensing Pressure

As noted earlier, the compressor maps and the biquadiatic fits to them are strictly applicable only for the superheat level or suction gas temperature for which they were generated. The map-based model applies correction factors to the empirical curve fits to model the compressor at actual operating conditions. Dabiri and Rice [49] presented a technique for correcting the compressor power input, $\dot{W}_{map}$, and the refrigerant mass flow rate, $\dot{m}_{map}$, for values of superheat or suction gas temperature other than those for which the maps were generated. Equations 3.2 and 3.3 give their correction factors to account for non-standard superheat values,

$$\dot{m}_{actual} = \left[1 + F_v\left(\frac{v_{map}}{v_{actual}} - 1\right)\right]\dot{m}_{map} \tag{3.2}$$

$$\dot{W}_{actual} = \left(\frac{\dot{m}_{actual}}{\dot{m}_{map}}\right)\left(\frac{\Delta h_{isen,actual}}{\Delta h_{isen,map}}\right)\dot{W}_{map} \tag{3.3}$$

where v and Δh represent specific volume and enthalpy change, respectively, of the refrigerant based on estimated suction port conditions. The subscripts "actual", "map", and "isen" represent actual superheat conditions, map superheat conditions, and an isentropic process from estimated suction port conditions to compressor shell outlet pressure, respectively, and F_v is a volumetric efficiency correction factor (assigned a value of 0.75 in the Block Data subroutine). Once the corrections for actual superheat level have been applied to the values of $\dot{W}_{map}$ and $\dot{m}_{map}$, the enthalpy at the compressor shell outlet, h_{outlet} is computed from Eq. 3.4

$$h_{outlet} = \frac{\left(\dot{W}_{actual} - \dot{Q}_{shell}\right)}{\dot{m}_{actual}} + h_{inlet} \tag{3.4}$$

Where Q_{shell}, is the heat loss rate from the compressor shell and is specified by the user as either a fixed input value or as a specified fraction of actual compressor power. The state at the compressor exit has been identified at this point in the calculations and all the relevant thermodynamic properties at the shell exit and condenser entrance are computed next. The calculations then proceed to the outer pressure drop convergence loop. The model is functionally dependent on the refrigerant saturation temperature at the condenser entrance and the evaporator exit and on the refrigerant superheat at the evaporator exit.

Figure 3.7 shows the sequence of calculations of compressor simulation. The current estimates of the condenser inlet and evaporator outlet refrigerant saturation temperatures are used to calculate the corresponding refrigerant pressures at the evaporator exit and the condenser entrance. The refrigerant state at the evaporator exit is identified using the specified degree of evaporator superheat or quality and the calculated evaporator exit pressure (from the estimated refrigerant saturation temperature), from which the refrigerant temperature, enthalpy, entropy, and specific volume are computed.

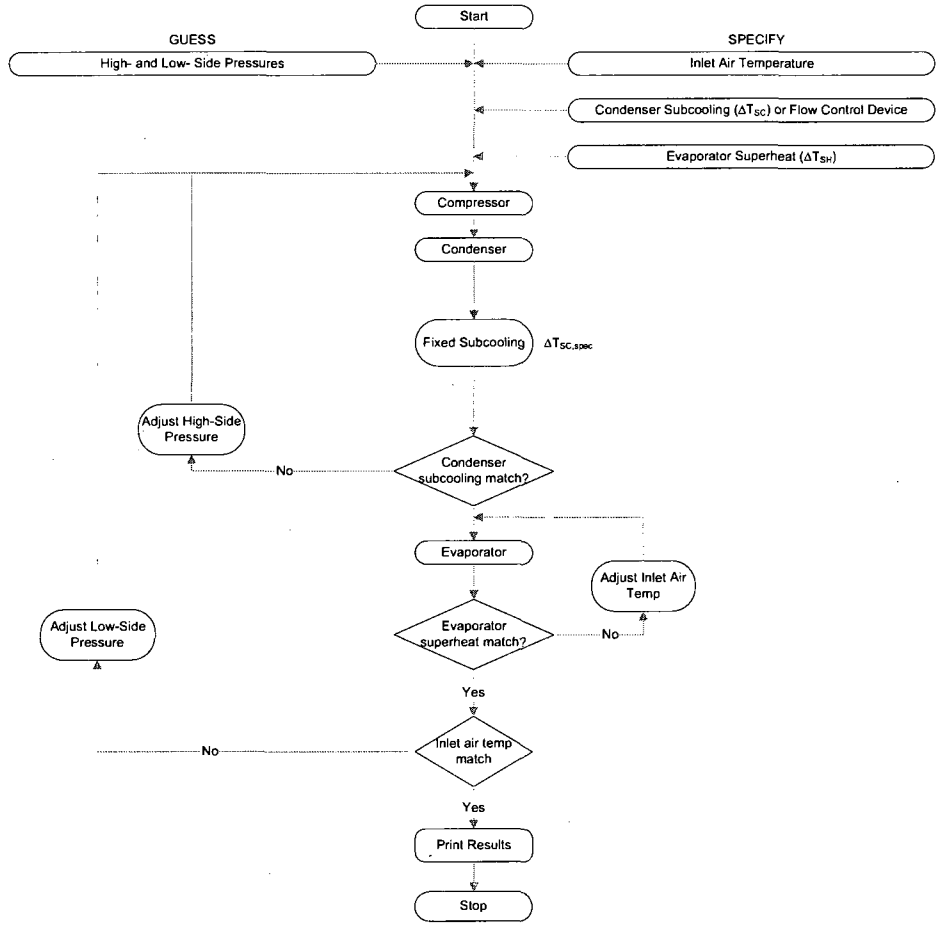

Figure 3.7 Computational Sequence of the Compressor Model

The pressure drops in the suction and discharge lines are computed using the current estimates for the refrigerant mass flow rate and average refrigerant temperatures in the lines. The refrigerant state at the compressor shell inlet is then identified using the calculated suction line pressure drop and the specified input value of heat gain in the suction line. The next step is calculating:

A. the refrigerant mass flow rate,

B. the compressor input power,

C. the refrigerant state at the compressor shell exit.

The refrigerant state at condenser entrance is computed using the previously calculated discharge line pressure drop and the specified (input) value of discharge line heat loss. Upon completion of these calculations, new average temperatures and specific volumes in the suction and discharge lines are computed. These are used with the latest calculation of the refrigerant mass flow rate to recalculate the suction and discharge line pressure drops. The entire process is repeated, as shown in Figure 3.7 , until the pressure drops agree within tolerances from one iteration to the next. After completion of the pressure drop iteration, compressor efficiency indices are computed. Two basic efficiency indices are calculated - the overall isentropic compression efficiency and the overall volumetric efficiency. The term "overall" is used to refer to a value based on compressor shell inlet and (when appropriate) shell outlet conditions. The overall isentropic compression efficiency is given by the equation;

$$\eta_{isen} = \frac{\dot{m}_{actual}(h_{outlet,isen} - h_{inlet})}{\dot{W}_{actual}} \tag{3.5}$$

where $\dot{W}_{map}$ and $\dot{m}_{map}$, represent compressor power and refrigerant mass flow rate. The term $\dot{h}_{outlet,isen}$ represents the outlet specific enthalpy that would be obtained an (ideal) isentropic compression process based on the refrigerant entropy at compressor shell inlet and the refrigerant pressure at shell outlet. Thus overall isentropic compression efficiency represents the ratio of the minimum power required (to compress a given refrigerant mass per unit time) to the actual required power. The overall volumetric efficiency (η_{vol}) is given by:

$$\eta_{vol} = \frac{\dot{m}_{actual}}{\dot{m}_{ideal}} = \frac{\dot{m}_{actual} v_{inlet}}{DS} \tag{3.6}$$

where v_{inlet} is the refrigerant specific volume at compressor shell inlet, D is the total compressor displacement, and S is the rated compressor speed.

3.3.2. Engine Model

The engine used for the GHP application is shown in Figure 3.8. This 3-cylinder water-cooled engine featuring high torque in the low rpm range is designed to run on natural gas and LPG (propane)/CNG (compressed natural gas). Considerable work has gone into developing this engine for specific GHP operation.

Figure 3.8 Engine Compressor Sub-Assembly

The engine oil sump contains 35 liters of oil. This excess oil allows a maintenance interval of every 6,000 hours and total engine life of 40,000 hours. Summary of engine specifications is shown in Table 3.2:

Table 3.2 Engine Specification

Item	Description
Model	950P
Type	4-stroke, Water cooled
Cylinder number	3
Displacement	950 cm^3
Compression ratio	9.3
Rated output	9.5 kW
Revolution range	1000 to 2800 rpm
Thermal efficiency	29 % (HHV) at maximum engine output
Enclosing oil amount	35 L
Maintenance interval	Every 6,000 hours
Engine life	40,000 hours

The thermodynamic model of the engine is obtained by the means experiment from the manufacturer. The steady working condition of the engine is mainly a function of load and speed. In this system modeling, the concerned parameters are engine power output, fuel flow rate (fuel input) and recoverable waste heat. In order to get the relationship between the engine thermodynamic parameters in a wide range of loads and speeds, an experimental data on the engine has been obtained. As shown in equation (3.7) a second order bivariate regression polynomial equation is employed to express the relations between the required parameters and speed and load.

$$y = \lambda_1 + \lambda_2 n + \lambda_3 n^2 + \lambda_4 T_r + \lambda_5 T_r^2 + \lambda_6 n T_r + \lambda_7 n T_r^2 + \lambda_8 n^2 T_r + \lambda_9 n^2 T_r^2 \qquad (3.7)$$

Where output y represents the power output, fuel input and recoverable engine heat, n represents engine speed and T_r represents torque. There are 66 valid data points from the experiment with the speed ranging from 1000 to 2800 rpm and torque ranging from 10 to 45 lbf-ft. The constants of the polynomials are shown in Table 3.3.

Table 3.3 Constants of Polynomial

	Fuel Flow rate	Engine Efficiency	Available Heat for Recovery
λ_1	6.11E-02	-1.45E-04	4.92E+01
λ_2	-1.31E-05	4.61E-08	-1.05E-02
λ_3	2.36E+00	7.31E-03	1.90E+03
λ_4	-2.86E-02	-1.12E-04	-2.30E+01
λ_6	-3.32E-03	1.33E-05	-3.04E+00
λ_7	5.93E-05	-1.69E-07	4.78E-02
λ_8	1.14E-06	-4.16E-09	9.18E-04
λ_9	-1.57E-08	5.58E-11	-1.27E-05

The engine power output, fuel input and amount of heat recovery computation begins after the compressor input requirement is determined from the heat pump cycle. As shown in Figure 3.9 block diagram, input variables to engine sub routine are engine/compressor speed, compressor input power, and fuel heating value.

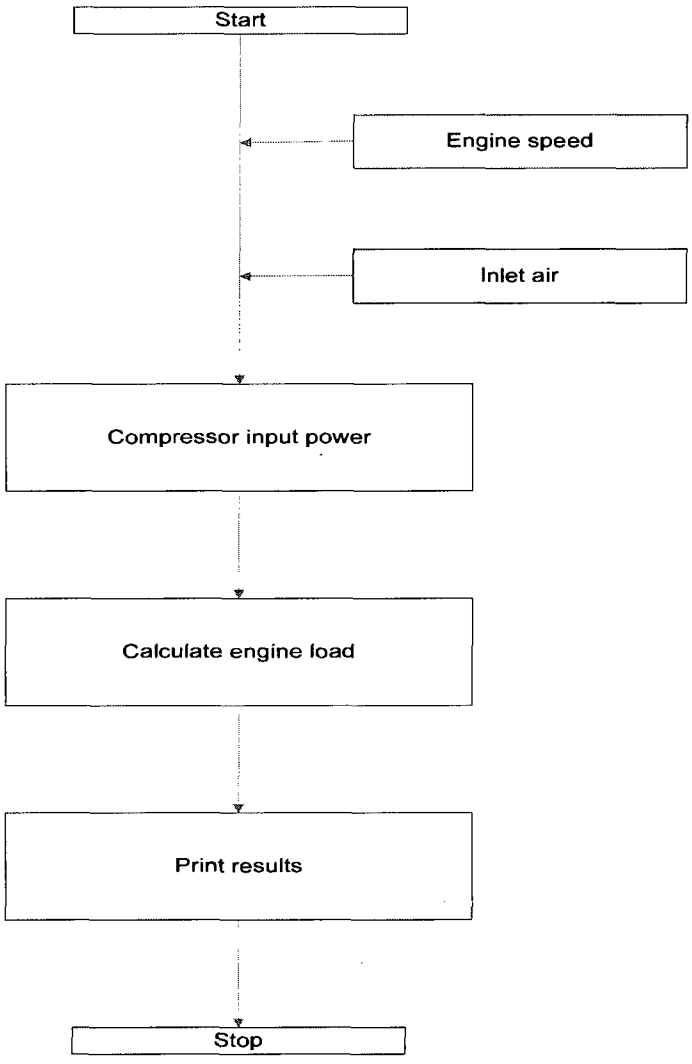

Figure 3.9 Block Diagram after Input Compressor Power

Figure 3.10 shows the horsepower curve for the engine. The graph points out the peak horsepower, an rpm value at which the power available from the engine is at its maximum. The peak horsepower in this case is around 2400 rpm and the peak torque at 2000 rpm.

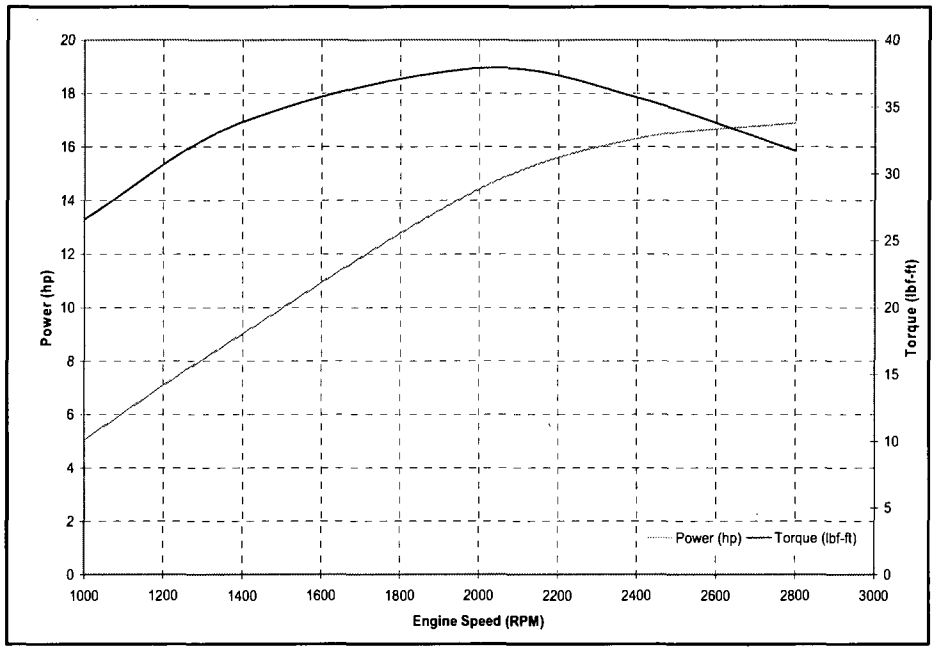

Figure 3.10 Power and Torque Curve of the Engine

As shown in Figure 3.11, the fuel consumption is highly dependent on speed. The fuel consumption ranges from 25 to 150 $\frac{ft^3}{hr}$ as the speed increases from 1000 to 2800 rpm. This is a vital parameter when evaluating the overall performance of the GHP.

One of the clear advantages of the GHP is the ability to recover the waste heat released by the engine cylinder jacket and exhaust gas in the heating mode. Figure 3.12 illustrate the available heat recovered from the engine cylinder jacket and exhaust gas as a function of speed and load. The available heat recovered ranges from 15000 to 80,000 Btu/hr.

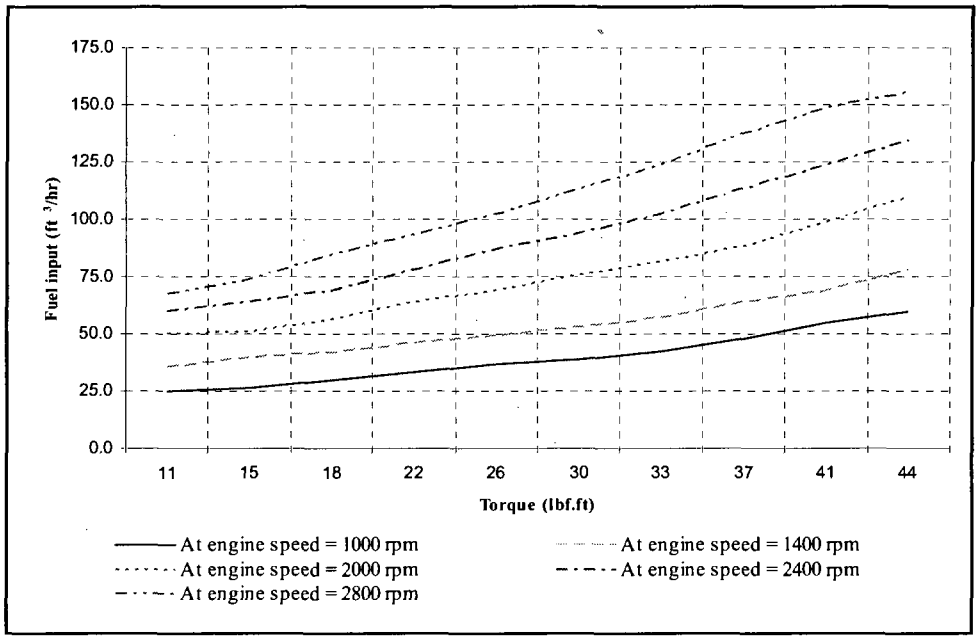

Figure 3.11 Input Fuel Consumption vs. Torque

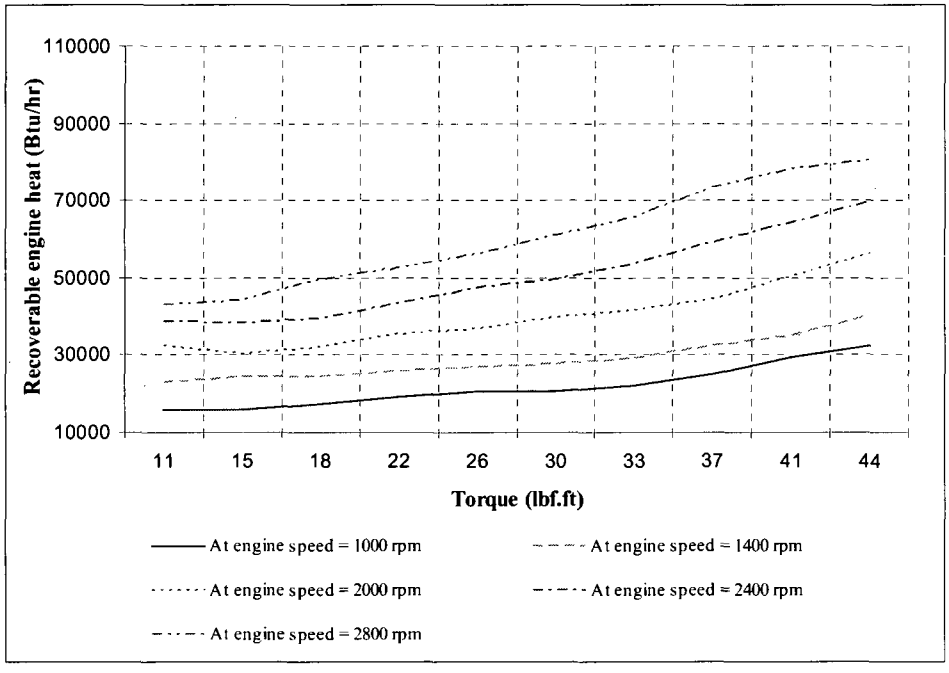

Figure 3.12 Recoverable Engine Heat vs. Engine Torque

3.3.3. Condenser and Evaporator Model

The heat exchanger of interest for this study is of the plate-fin-and-tube configuration. A schematic of a typical plate-fin-and-tube heat exchanger is shown in Figure 3.13.

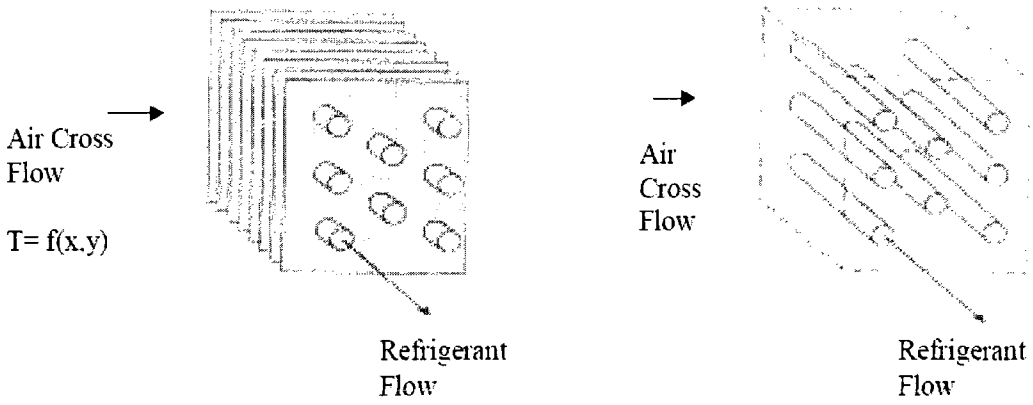

Figure 3.13. Typical Plate Fin-and-Tube Cross Flow Heat Exchanger

Table 3.4 show the specification of both indoor and out door heat exchangers used in this study.

Table 3.4 Outdoor and Indoor Heat Exchanger Specification

	Outdoor unit data	**Indoor unit data**
Heat exchanger frontal area	27.5 ft^2	15.25 ft^2
Fin material	Aluminum	Aluminum
Fin thickness	0.0045 *in*	0.0045 *in*
Fin type	Wavy	Wavy
Pitch	20 $\frac{fins}{in}$	18 $\frac{fins}{in}$
Tube material	Copper	Copper
Tube outer diameter	0.3125 *in*	0.3125 *in*
Tube wall thickness	0.012 *in*	0.012 *in*
Number of rows	4	4
Tube spacing	1.00 X 0.625 *in*	1.00 X 0.625 *in*

The model calculates the performance of air-to-refrigerant condensers and evaporators by using:

A. effectiveness vs. NTU correlations for heat transfer for a dry coil,

B. a modified version of the effective surface temperature approach when there is dehumidification,

C. the Thorn correlation for two-phase refrigerant pressure drops and the Moody friction factor chart plus momentum terms for the single phase refrigerant pressure drop, and

The calculation methods which have been used assume that the heat exchangers consist of equivalent, parallel refrigerant circuits with unmixed flow on both the air and refrigerant sides. The refrigerant-side calculations are separated into two computations for the superheated and two-phase regions for the evaporator and for the superheated, two-phase, and subcooled regions for the condenser. Figure 3.14 is a general block diagram, or flow chart, outlining the organization and iterative loops for the condenser model. Figure 3.15 is a similar diagram for the evaporator calculations. The air-side mass flow rate for each heat exchanger is calculated from the volumetric air flow rate specified in the input data and the air density calculated from the ideal gas equation using atmospheric pressure, the universal gas constant for air, and the inlet air temperature. Since the heat exchangers are modeled as several equivalent parallel refrigerant circuits (the actual number being specified with the input data), the air-side mass flow rate and the estimated refrigerant mass flow rate from the compressor model are divided by the number of circuits to obtain values for each circuit.

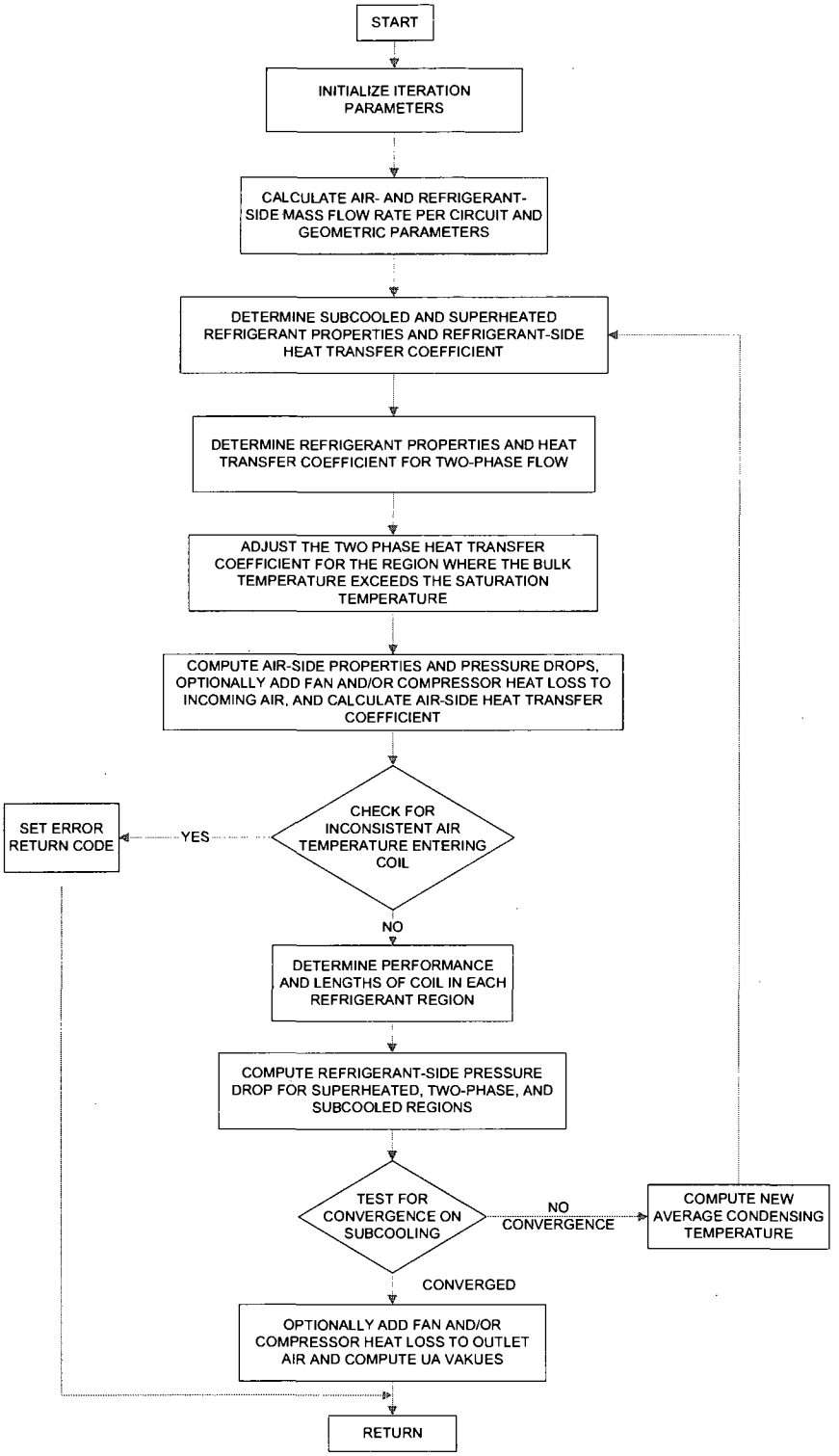

Figure 3.14 General Structure of the Condenser Model

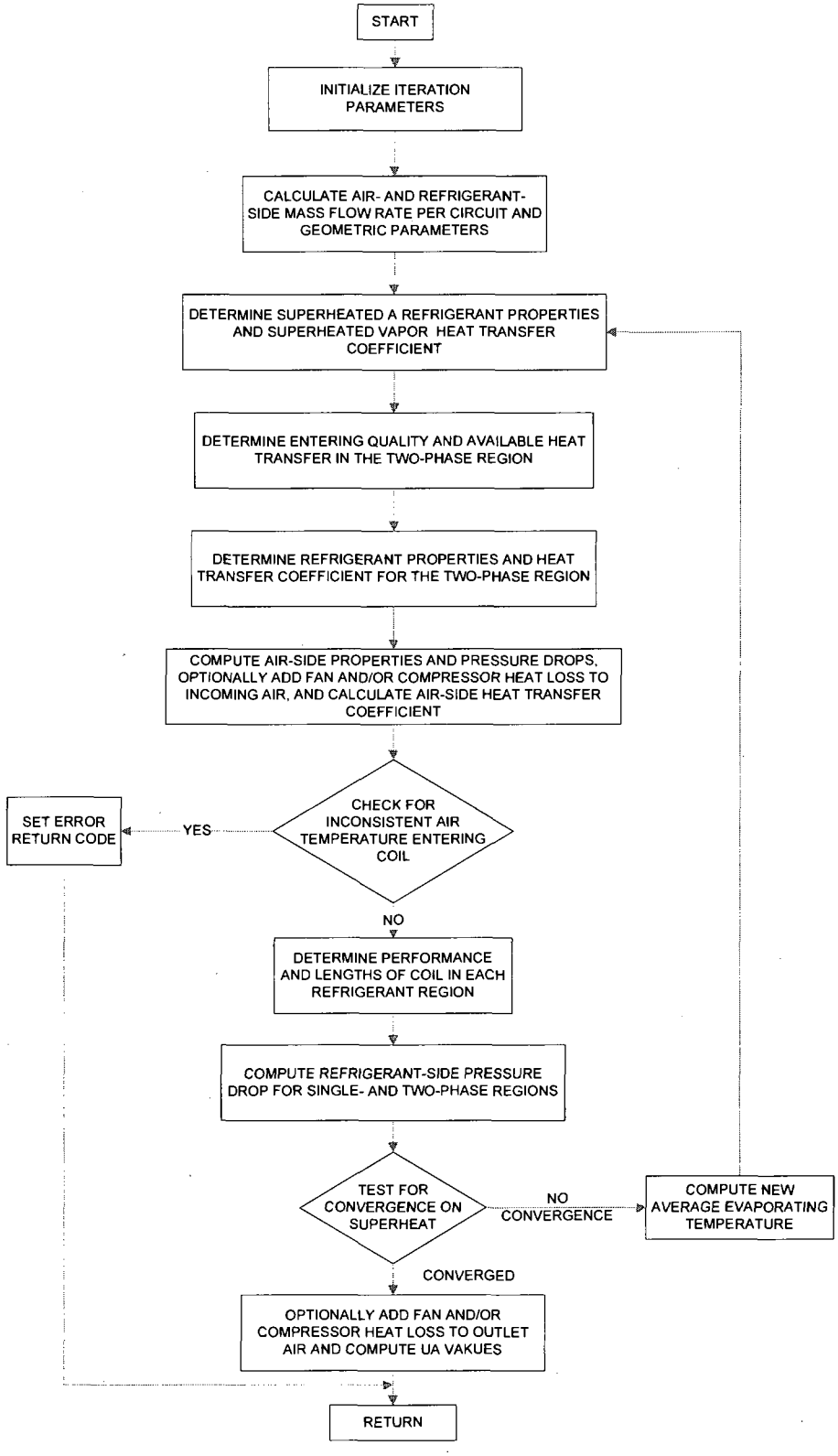

Figure 3.15 General Structure of the Evaporator Model

The average densities of the refrigerant liquid and vapor in the two-phase region of each coil and the latent heat of vaporization are calculated from the current estimates of the average saturation temperatures in the heat exchangers. The thermo-physical properties for the single-phase refrigerant (subcooled and superheated for the condenser and superheated for the evaporator), i.e., the viscosity, thermal conductivity, and liquid specific heat, are calculated according to a routine written by Flower [50]. The specific heat for the vapor region, is determined by a routine developed by Kartsounes and Erth [51] which computes the local value of

$$\left.\frac{\partial h}{\partial t}\right|_p = C_{p,v} \tag{3.8}$$

Single-phase refrigerant heat transfer coefficient for the superheated region in the condenser is calculated using an equation by Kays and London [52].

$$h = C_1 G_r C_{p,v} \mathrm{Pr}^{\frac{-2}{3}} \mathrm{Re}^{C_2} \tag{3.9}$$

Where $\mathrm{Re} = \dfrac{G_r D}{\mu}$

$$C_1 = 1.10647 \rightarrow for \rightarrow \mathrm{Re} < 3500$$
$$C_1 = 3.5194 \times 10^{-7} \rightarrow for \rightarrow 3500 \leq \mathrm{Re} < 6000$$
$$C_1 = 0.01080 \rightarrow for \rightarrow \mathrm{Re} \geq 6000$$

$$C_2 = -0.78992 \rightarrow for \rightarrow \mathrm{Re} < 3500$$
$$C_2 = 1.03804 \rightarrow for \rightarrow 3500 \leq \mathrm{Re} < 6000$$
$$C_2 = -0.13750 \rightarrow for \rightarrow \mathrm{Re} \geq 6000$$

The heat transfer coefficients for the subcooled region of the condenser and the superheated region in the evaporator are computed using the Dittus-Boelter correlation for fully developed flow [53]:

$$h = 0.023 G_r C_p \, \mathrm{Pr}^{C-1} \, \mathrm{Re}^{-0.20} \tag{3.10}$$

where "C" is 0.3 when the refrigerant is being cooling and 0.4 when being heated. The air-side heat transfer coefficients are based on the work of McQuiston [54, 55], and are calculated by the correlation given by

$$h_a = C_0 G_a C_{pa} \, \mathrm{Pr}^{\frac{-2}{3}} \, j \left[\frac{1 - 1280 N_T \, \mathrm{Re}^{-1.2}}{1 - 5120 \, \mathrm{Re}^{-1.2}} \right] \tag{3.11}$$

where:

$$j = 0.0014 + 0.02618 \left(\frac{1}{1 - F_a} \right)^{-0.15} \left(\frac{G_a D}{\mu} \right)^{-0.4} \tag{3.12}$$

C_0 = 1.0, 1.45, or 1.75 depending on whether the fins are smooth, wavy, or louvered

The above equation was obtained from extensive test data on smooth fins over the Reynolds number range of $3500 \le \mathrm{Re} \le 15000$. The heat transfer coefficients for wavy and louvered fins are assumed to be predicted approximately by the use of the smooth fin equation increased by the multiplicative constant C_o. The heat transfer coefficients also calculated for wavy and louvered fin surfaces are assumed to be referenced to smooth-fin surface area; thus the C_o values for wavy and louvered fins are intended to account for increases in both heat transfer coefficient and surface area from smooth fin values. The equation 3.11 includes terms to adjust for a number of geometric effects such as the number of tube rows, the fin spacing, and the transverse tube spacing. The air-side properties calculated using a modified version of a subroutine by Flower [50]. The air-side heat transfer coefficient for the portion of the evaporator which is wetted due to dehumidification is calculated from the dry coefficient, h_a given by Myers [56].

$$h_{a,w} = 0.626\left(\frac{\dot{Q}}{A}\right)^{0.101} h_a \tag{3.13}$$

The fin efficiency and overall surface effectiveness for the condenser and for the dry region of the evaporator are calculated based on the work of Schmidt [57] as reported by McQuiston and Tree [58] for a tube surrounded by a hexagonal fin segment of a sheet fin (the representative fin shape surrounding each tube in a staggered tube arrangement). This work has been generalized to properly handle orientation changes that occur as the longitudinal and transverse tube spacing is varied.

3.3.4. Air-Side Pressure Drops and Fan Powers

The airside pressure drop for the indoor unit is calculated as the sum of pressure drops due to the ducts, filter, and the coil. The coil pressure drop for smooth fins is based on Fanning friction factors for the dry and wet regions and correlating parameters and defined by McQuiston [54, 55].

The fan motor power consumption, $\dot{W}_{fan}$, is computed according to Equation (3.14)

$$\dot{W}_{fan} = 11.1\frac{\dot{Q}\Delta P_{air}}{\eta_{fan}} \tag{3.14}$$

where the constant is to convert to consistent units. The combined fan and fan-motor efficiency, $\eta_{famotorn}$, is a constant for the indoor unit and can be held constant or allowed to vary with the fan specific speed for the outdoor unit. An outdoor fan efficiency curve is provided as an option for the outdoor coil because the outdoor coil and fan characteristics are closely coupled. The indoor fan is less affected by the indoor coil airside pressure drop than by the rest of the indoor duct system. Therefore, an after-the-fact selection of an indoor fan will not be likely to result in any compatibility problems.

3.3.5. Pressure and Enthalpy Changes in Refrigerant Lines

All of the refrigerant-side pressure losses are computed on the basis of equivalent lengths. The equivalent length and inside diameter of each section of refrigerant piping are specified as part of the input data for:

A. the liquid line from the condenser to the flow control device,

B. the line from the outdoor coil to the reversing valve,

C. the line from the indoor coil to the reversing valve, and

D. the suction and discharge lines from the compressor shell inlet and outlet to the reversing valve.

The rates of heat loss in the discharge and liquid lines, and the heat gain in the suction line can also be specified in order to allow enthalpy changes in the piping. The Darcy incompressible flow relation, as given by Equation (3.15), is used to compute the pressure drop of the refrigerant in both the compressor suction and discharge lines:

$$\Delta P = \frac{2f(\frac{L}{D})G^2}{\rho_{ave}} \tag{3.15}$$

where f is the Moody friction factor.

Thus, it has been assumed that there are no significant density or momentum changes in these lines. The Moody friction factor, *f*, in Equation (3.15) is computed using a subroutine written by Hiller and Glicksman [44] and takes into account the surface roughness of the tubes.

The refrigerant-side pressure drops for the evaporator and condenser are calculated separately for the superheated, two-phase, and subcooled regions of each coil. The

pressure drop in the vapor region is computed as the sum of changes due to momentum and friction effects and due to losses in the return bends.

It has been assumed that the density changes in the subcooled region of the condenser are insignificant, so the pressure drop in the liquid region only has friction and return bend components. The pressure drop in the two-phase region of each heat exchanger is calculated as the sum of momentum, friction, and return bend components integrated over the two-phase region. The momentum and friction terms are computed using equations from Thorn [59] as discussed by Goldstein [60]. The total pressure drop in the return bends with two-phase flow is computed using equation given by [61].

CHAPTER 4

SYSTEM MODELING RESULTS AND ANALYSIS

4.1. Baseline System Modeling Results and Analysis

In this section the performance of the GHP without the suction liquid line and heat recovery heat exchanger will be discussed. This gives the baseline performance of the unit and will later aid to compare performance gains due two the suction liquid line heat exchange in cooling case and the suction heat recovery in heating mode. In this model the GHP performance at low (1400 rpm), intermediate (2000rpm) and high (2400 rpm) engine speeds is analyzed. The air flow rate in the outdoor and indoor heat exchanger is 8000 and 4000 $\frac{ft^3}{\min}$ respectively.

4.1.1. Cooling Performance Analysis

In order for the condenser to reject the total heat (process heat load plus heat of compression) to the ambient air, the temperature difference between the hot refrigerant gas and the ambient air must be sufficient. Figure 4.1 show the relationship between the condensing temperatures as a function of ambient temperature.

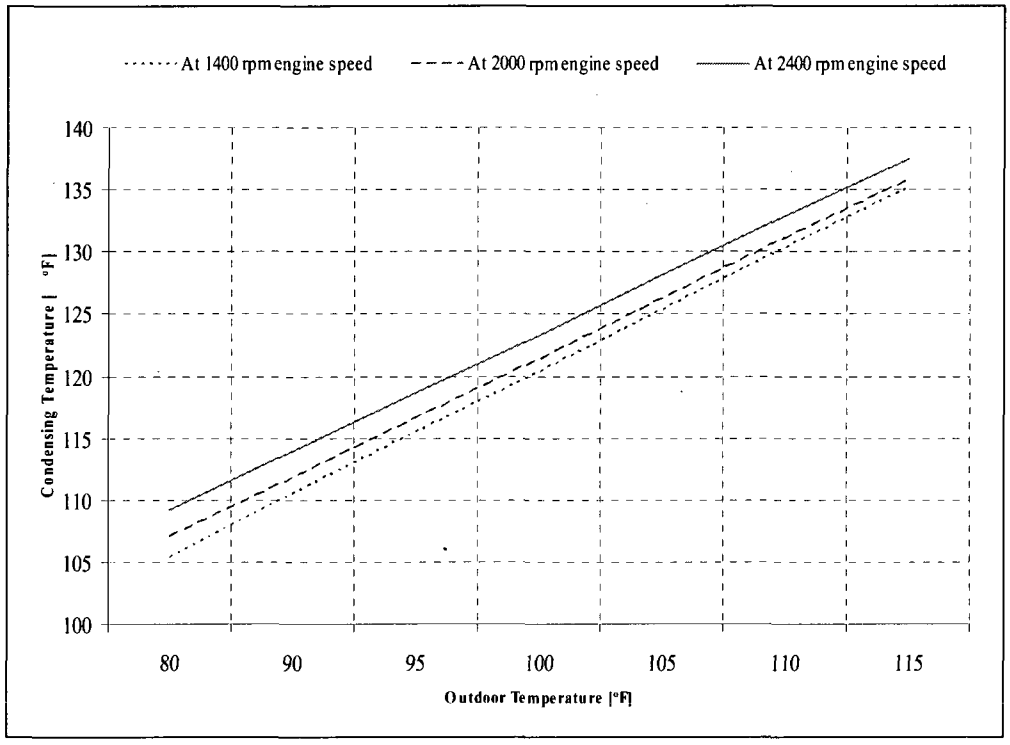

Figure 4.1 Condenser Temperature vs. Outdoor Temperature

As the ambient air temperature increases, the ability of the condenser to transfer the process heat from the refrigerant to the ambient air is reduced, causing higher condensing temperatures and pressures that could result in reduced system performance. Similarly, if the ambient temperature decreases, the performance will improve due to the larger initial temperature differential.

Figure 4.2 shows cooling capacity at outdoor temperature ranged from 80 °F to 115 °F using refrigerant R410A. Over this temperature range, capacity decreased from 134.8 kBtu/h to 116.4 kBtu/h; a decrease of 13.6 % for the higher speed case. The two most influential fundamental thermodynamic properties affecting capacity degradation are a refrigerant's critical temperature and molar heat capacity. For a given application, a fluid with a lower critical temperature will tend to have a lower capacity. The lower critical

temperature of R410A indicates that degradation of performance at high ambient temperature should be greater for R410A than the phased out refrigerant R22.

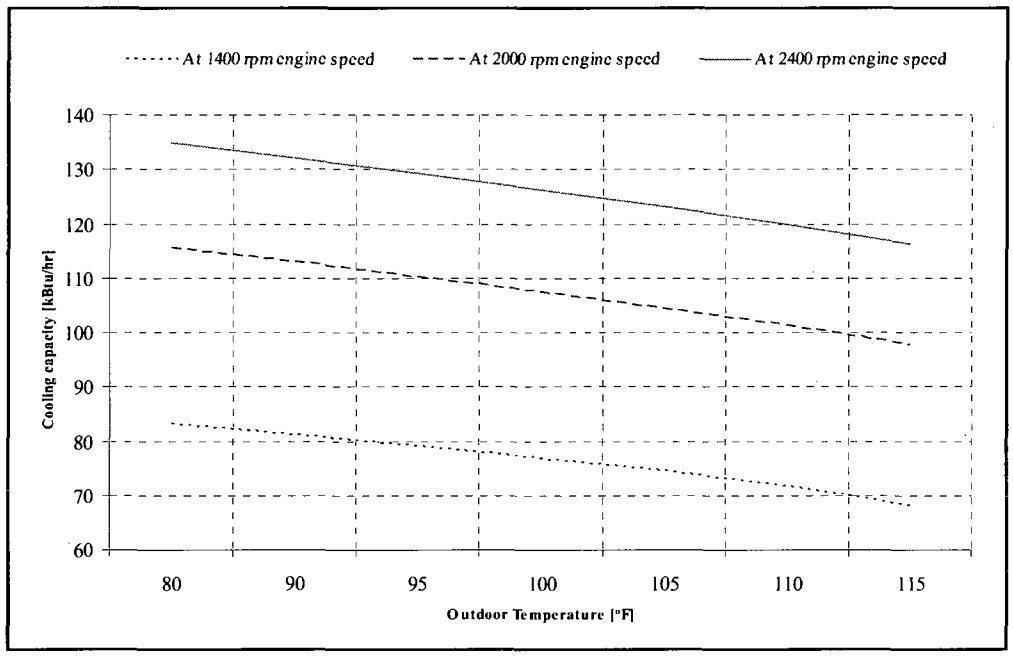

Figure 4.2 GHP Cooling Capacity vs. Outdoor Temperature

Scroll compressor designs have been used traditionally with refrigerants due to both the cooling provided by the high density and high specific heat gas, and the low heat-of-compression associated with typical refrigerants. This results in gas compression temperatures of less than 300°F and oil sump temperatures less than 212°F, and moderate operating temperatures for the gas cooled compressor motor and mechanical components such as valves and bearings. Gas entering a typical air conditioning scroll requires approximately three orbits, or crankshaft rotations, to reach discharge pressure. The scroll compression process is optimal at a specific design pressure ratio (based on the design volume ratio) but has reduced efficiency for increasingly higher pressure ratios. This

efficiency reduction is common to most compressors, and is due primarily to the greater inherent losses at higher-pressure ratios than to operation away from the design pressure ratio. For example, an increase in compression ratio from 2.8 to 3.8 at high speed operation has isentropic efficiencies of 79% and 74% respectively. As shown in Figure 4.3, in cooling mode operation the compression is highly a function of condensing pressure which is mainly a function of ambient temperature.

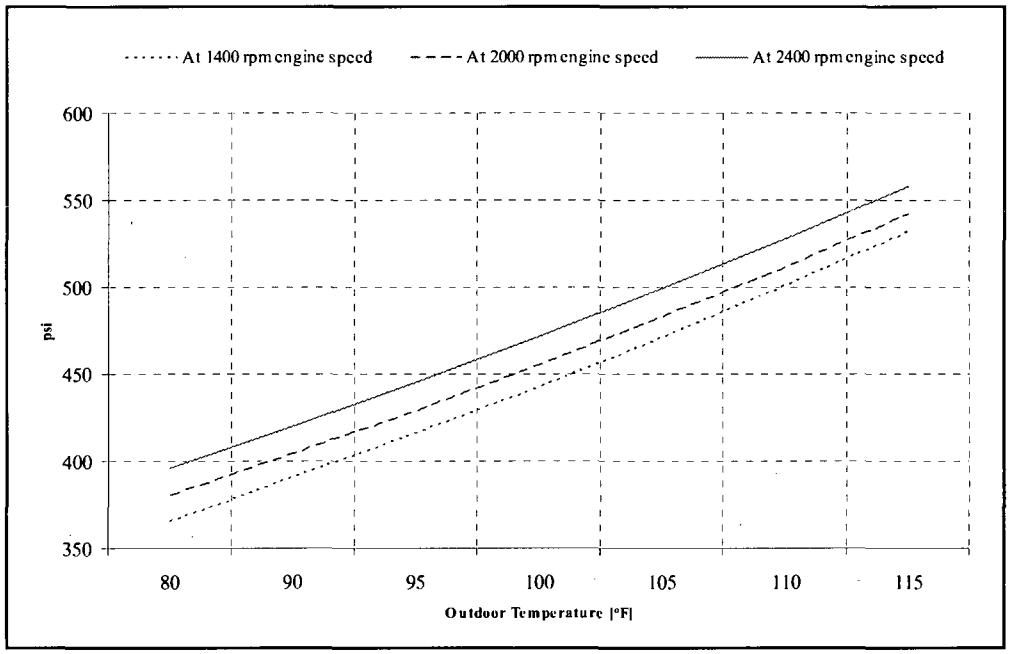

Figure 4.3 Refrigerant Discharge Pressure vs. Outdoor Temperature

As shown in Figure 4.4, the compression ratio increased from 2.75 to 3.75 when the ambient temperature increased from $80^{o}F$ to $115^{o}F$ at a constant refrigerant evaporating temperature and compressor/engine speed.

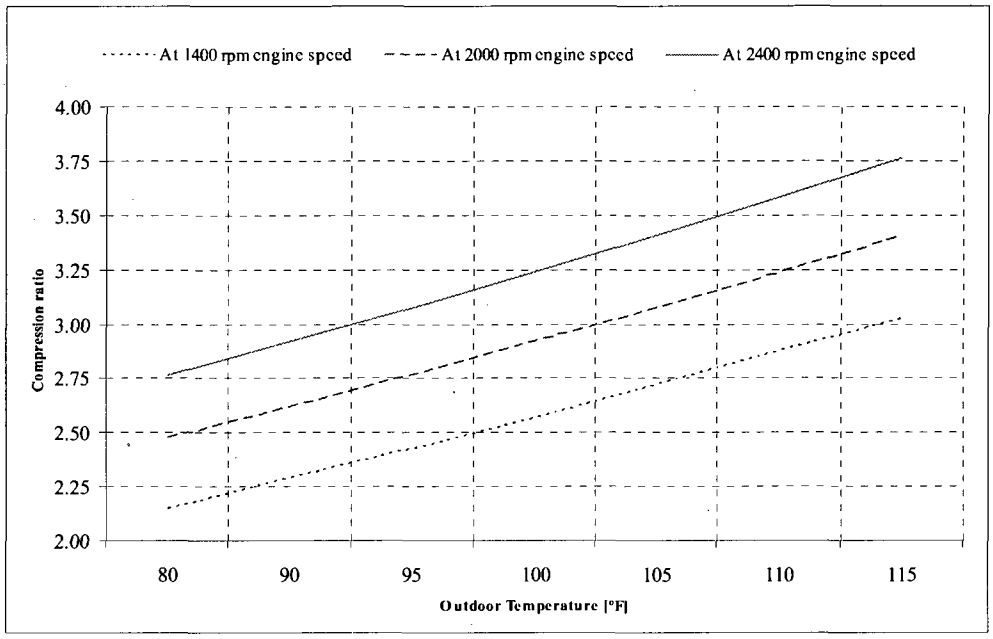

Figure 4.4 Compression Ratio vs. Outdoor Temperature

As the ambient temperature decreases, the saturation pressure in the condenser also decreases. Therefore, the pressure rise in the compressor decreases. As a result, the compressor requires less power. Furthermore, as the ambient temperature decreases, the condensing temperature decreases. Thus, the enthalpy of the refrigerant entering the evaporator is reduced.

The decrease in the enthalpy of the refrigerant entering the evaporator that is produced by the decrease in the ambient temperature causes the evaporator cooling capacity to increase. This decrease in the enthalpy of the refrigerant entering the evaporator also causes a reduction of the mass flow rate of refrigerant required to maintain the evaporator cooling capacity. Hence, the amount of compressor work is decreased. Therefore, the ultimate result of decreasing the ambient temperature is an increase in the overall system performance.

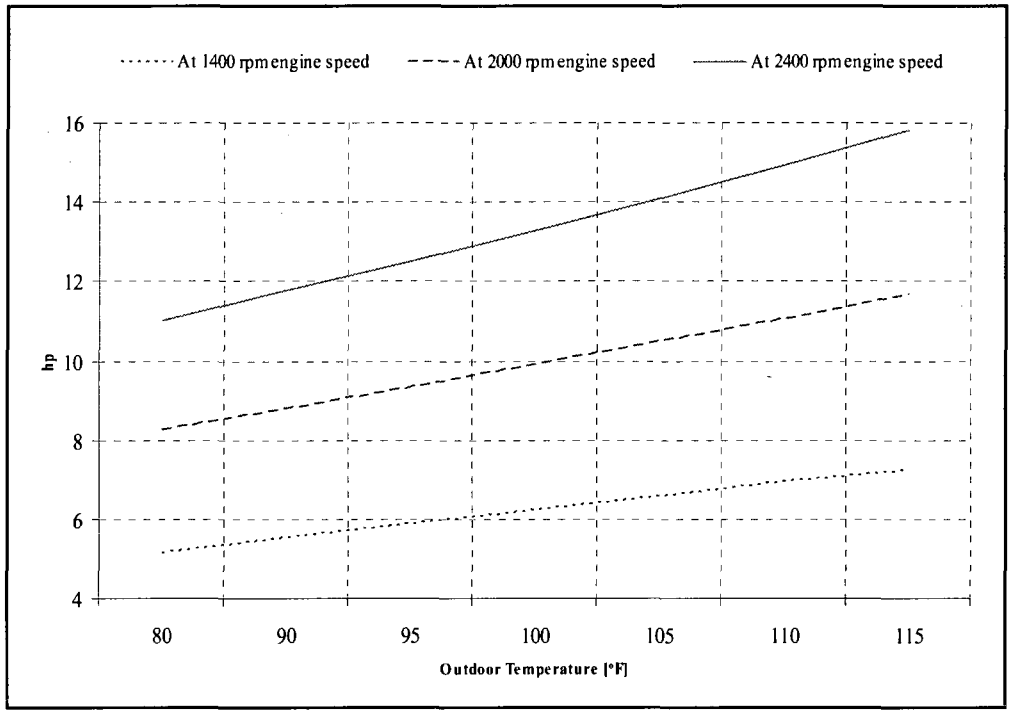

Figure 4.5 Compressor Input Power vs. Outdoor Temperature

Figure 4.5 shows how ambient temperature influence the power input to the compressor and mass flow rate. It's shown that the power consumption increases linearly with ambient temperature. As the power consumption by the compressor increases the fuel consumption by the engine also increases proportionally. As shown in Figure 4.6, the fuel consumption is significantly affected by the engine speed. This unique capability of modulating the compressor speed by adjusting the gas supply allows matching the building load accurately and at the same time lowers the input energy (natural gas input power by the engine) requirement.

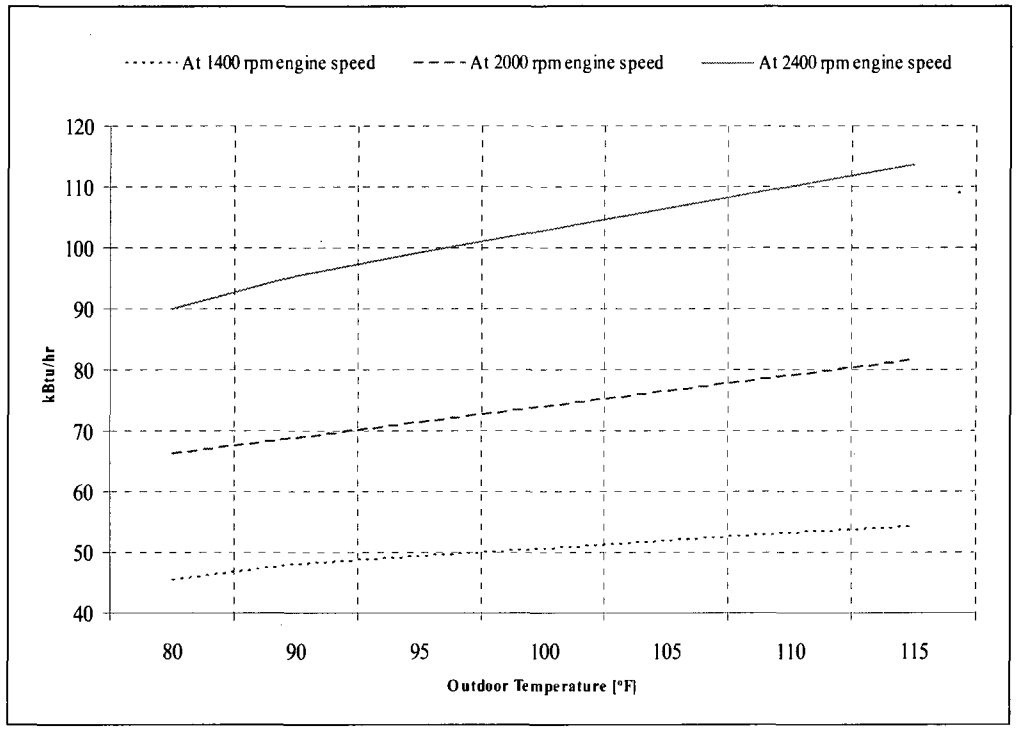

Figure 4.6 Fuel Consumption by the IC Engine vs. Outdoor Temperature

In Figure 4.7 it is attempted to determine the percentage of power output to fuel input by the internal combustion engine. The ratio is the highest and the lowest at engine speeds of 2000 rpm and 1400 rpm respectively. At internal combustion engine speed of 2000 rpm, 31.7% of the total energy input is converted to useful work. The remaining 68.3% is rejected as heat to the cooling coolant, exhaust and unrecoverable engine block heat.

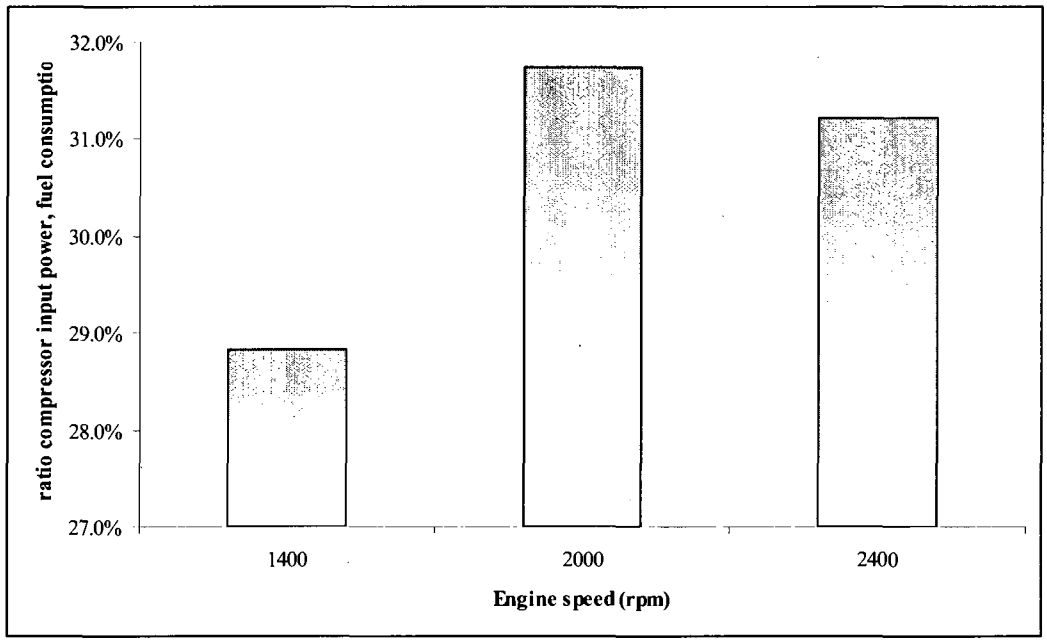

Figure 4.7 Ratio of Power Output to Energy Input vs. Engine Speed

In order to quantitatively evaluate the performance of any heat pump system, a figure of merit must be established. For a heat pump system utilizing a vapor compression refrigeration cycle, the efficiency is expressed in terms of the cooling/heating coefficient of performance or the COP. The coefficient of performance is a dimensionless quantity. It is the ratio of the rate of cooling or heating capacity to the power input. In this study, the COP is expressed as:

$$COP_C = \frac{Cooling_{capacity}}{Engine_{fuel\_input}} \tag{4.1}$$

Figure 4.8 shows a decrease in COP at elevated ambient temperatures. Operation of an air conditioner at elevated ambient temperatures inherently results in a lower COP. This conclusion comes directly from examining the Carnot cycle. The COP relation

indicates that the COP decreases when the condenser temperature increases at a constant evaporation temperature.

$$COPp_{Carnot} = \frac{T_{evap}}{(T_{cond} - T_{evap})} \tag{4.2}$$

This theoretical indication derived from the reversible cycle is valid for all refrigerants. For refrigerants operating in the vapor compression cycle, the COP degradation is greater than that for the Carnot cycle and varies among fluids.

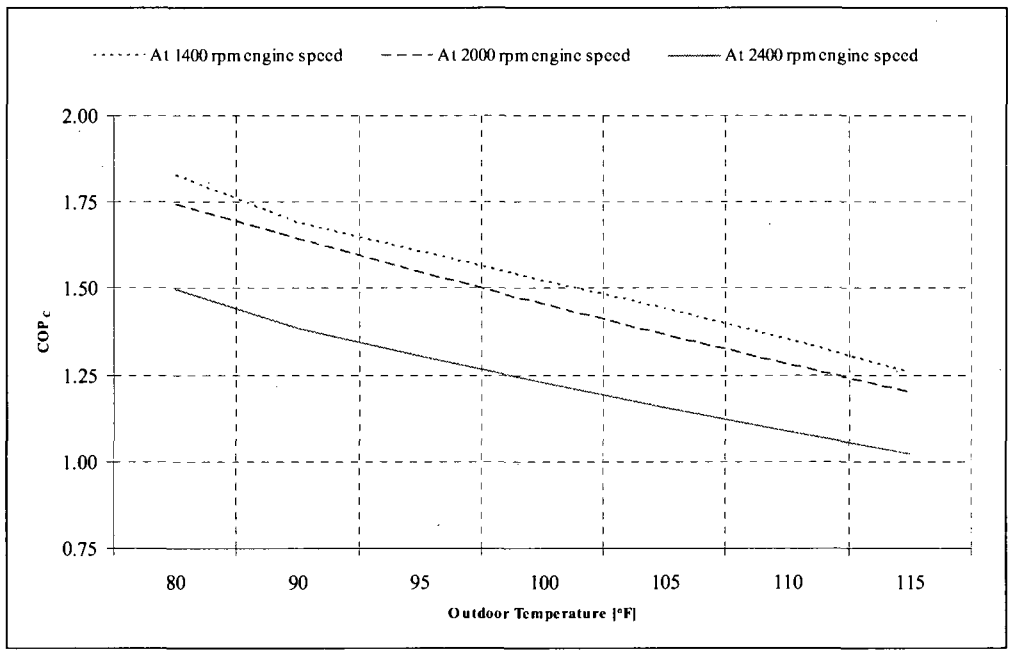

Figure 4.8 Source Cooling Coefficient of Performance vs. Outdoor Temperature

Based on the results obtained, the following key conclusion could be deduced:

A. both the heat pump and engine system are influenced by engine speed remarkably. The increase of engine speed will decrease the efficiency of the heat pump. GHP is more energy saving in low speed mode;

B. Ambient temperature affects the performance of the heat pump much but has little influence on the engine efficiency in the constant engine speed mode;

C. At an engine speed of 2000 rpm the ratio of input to output power is found to be the highest.

4.1.2. Heating Performance Analysis

Figure 4.9 and Figure 4.10 show the refrigerant suction pressure and compression ratio as a function of evaporating temperature respectively. In the heating application of a heat pump, the evaporator is the outdoor coil and it is a function of ambient inlet air temperature. As the ambient temperature increases the refrigerant evaporating temperature and pressure also increases.

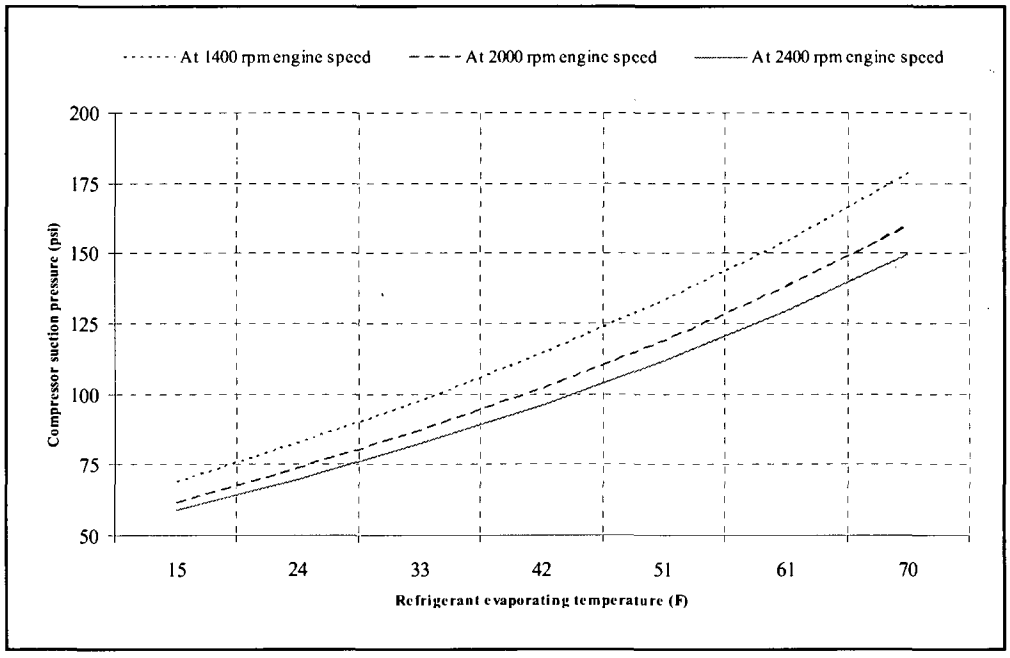

Figure 4.9 Suction Pressure vs. Refrigerant Evaporating Temperature

The compression ratio (discharge refrigerant pressure divided by suction refrigerant pressure) is higher at lower evaporating temperatures. The condensing/discharge pressure is a strong function of indoor air inlet temperature which is normally at room temperature. In this case, the compression ratio is highly affected by the ambient temperature or refrigerant evaporating temperature. As the ambient temperature decreases, the evaporating temperature/pressure decreases and this increases the pressure ratio between discharge and suction. Temperature lift (compression ratio) affects compressor performance significantly.

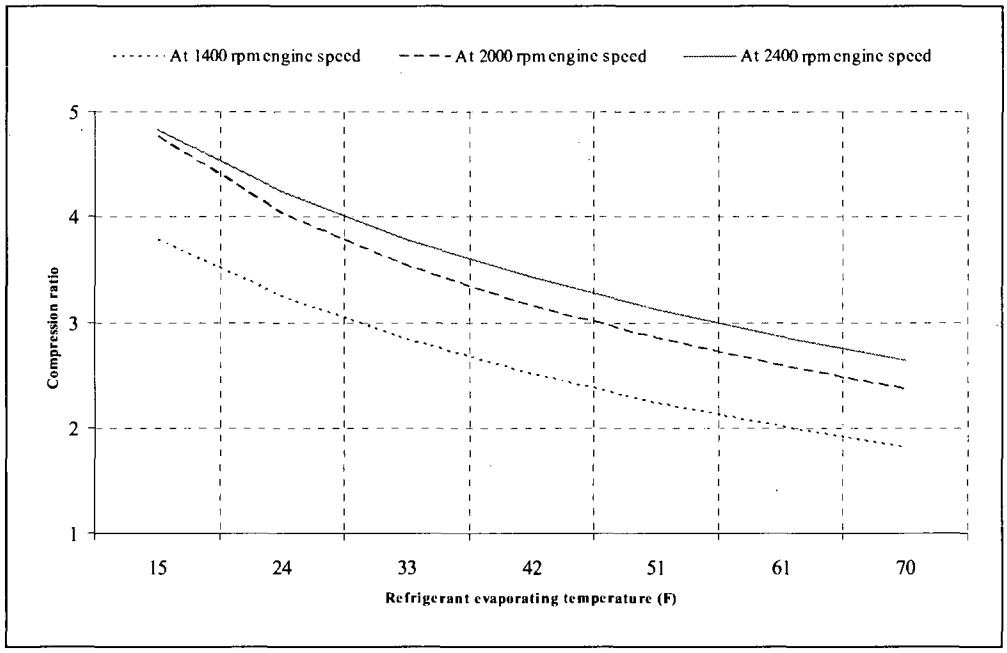

Figure 4.10 Compression Ratio vs. Refrigerant Evaporating Temperature

Figure 4.11 shows the variation of the compressor power requirement with evaporating temperature. Power requirement increases, of course, with speed and compression ratio (highly a function of evaporating temperature/pressure). When the

refrigerant evaporating temperature increased from 15 to 70°F, the compressor input power requirement increased by 48.1%, 31.7% and 29.4% at 2400, 2000 and 1400 rpm respectively.

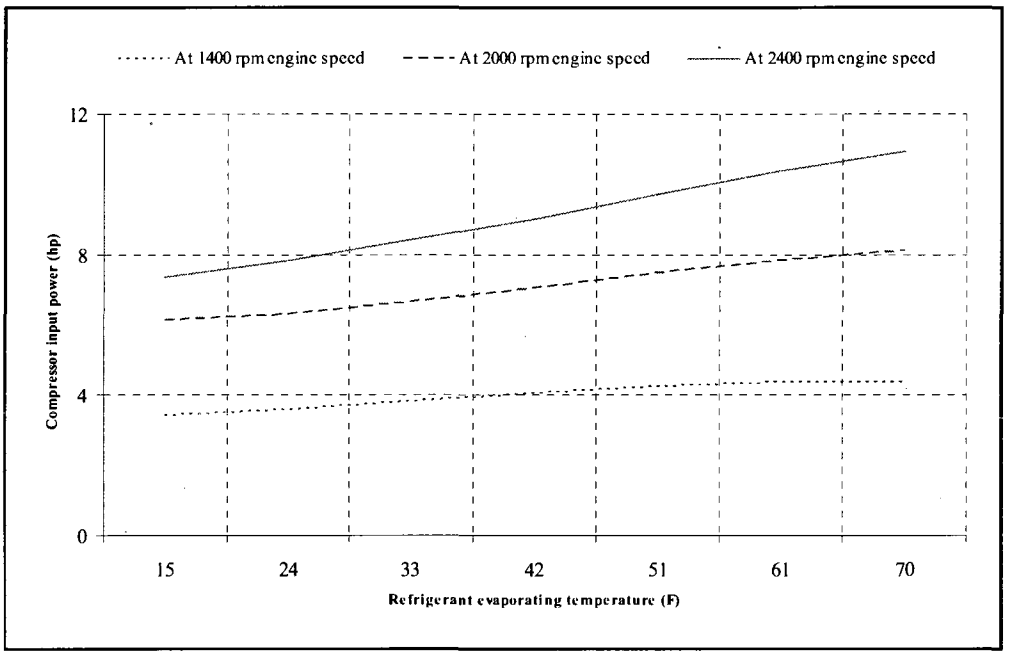

Figure 4.11 Compressor Power Requirement vs. Evaporating Temperature

The compressor is more efficient when the condensing pressure is low and the evaporating pressure is high, leading to the minimum temperature lift and compression ratios. Figure 4.12 shows a plot of heat pump capacity to compressor input power ratio as a function of evaporating temperature and engine speed. As shown in the figure as the evaporating temperature increases the ratio is higher. It is essential that the refrigerant reaches a sufficiently high temperature when it is compressed, since the second law of thermodynamics prevents heat from flowing from a cold fluid to a hot heat sink. Similarly, the fluid must reach a sufficiently low temperature when allowed to expand, or

heat cannot flow from the cold region into the fluid. In particular, the pressure difference must be great enough for the fluid to condense at the hot side and still evaporate in the lower pressure region at the cold side. The greater the temperature difference, the greater the required pressure difference and consequently more energy is needed to compress the fluid. Thus as with all heat pumps, the performances (amount of heat moved per unit of input work required) decreases with increasing temperature difference. The ratio is also highest at part load when the compressor speed is lower (lower engine speed).

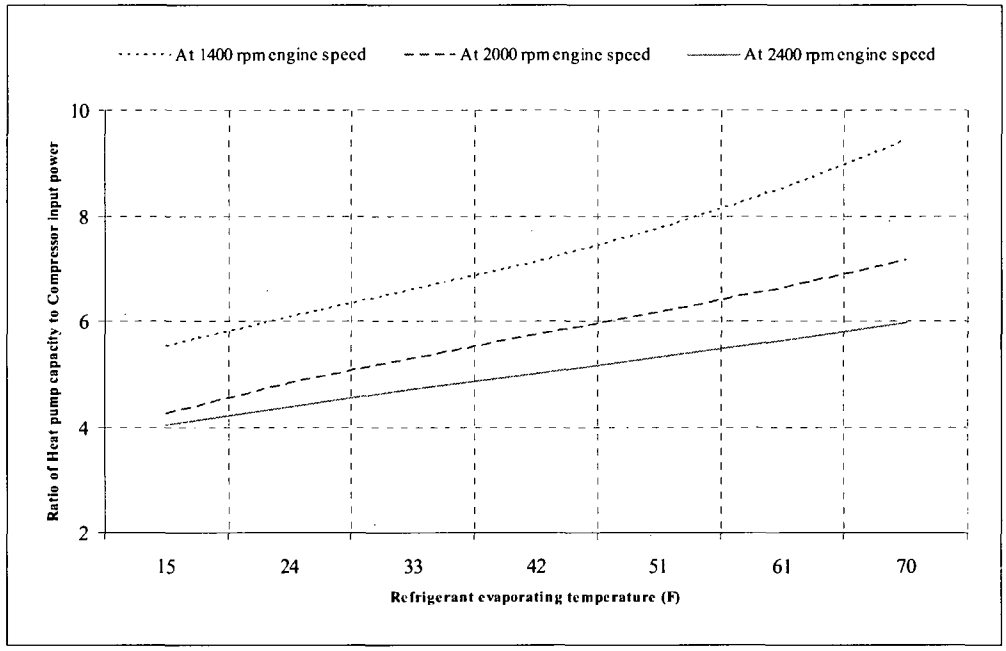

Figure 4.12 Ratio of Heat Pump Capacity to Compressor Input Power

The mass flow rate of refrigerant through the compressor depends on displacement and density of gas entering the chamber. The volume displaced depends on the compressor rpm. This volumetric displacement is a fixed volume per revolution. The amount of refrigerant molecules that fill this fixed volume depends on how dense the

refrigerant gases are coming into suction side of the compressor. The density of the refrigerant depends on the evaporating temperature and pressure. The higher evaporating temperature the superheated gases are, the denser they will be. As shown in Figure 4.13, at engine speed of 2400 rpm, the refrigerant mass flow rate dropped by 61% when the evaporating temperature fell from 70 to $15\,^{o}F$.

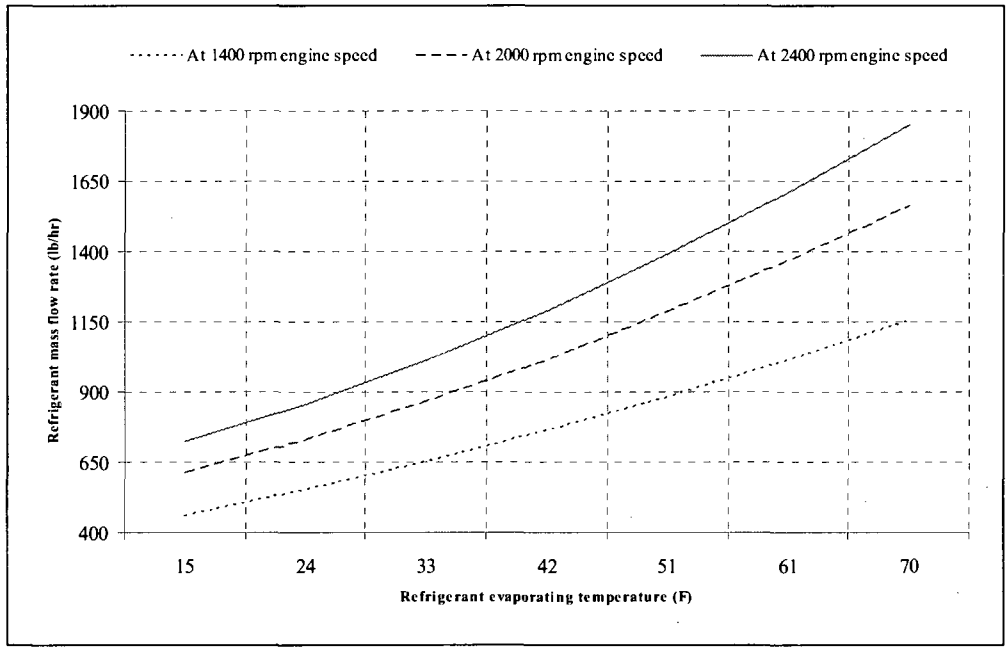

Figure 4.13 Refrigerant Mass Flow Rates vs. Evaporating Temperature

The main disadvantage of an air source heat pump are the effects large variations of ambient temperature within seasons and areas. Such variations have a significant effect on the performance of air source heat pump. The evaporator temperature will fall with decreased ambient temperature.

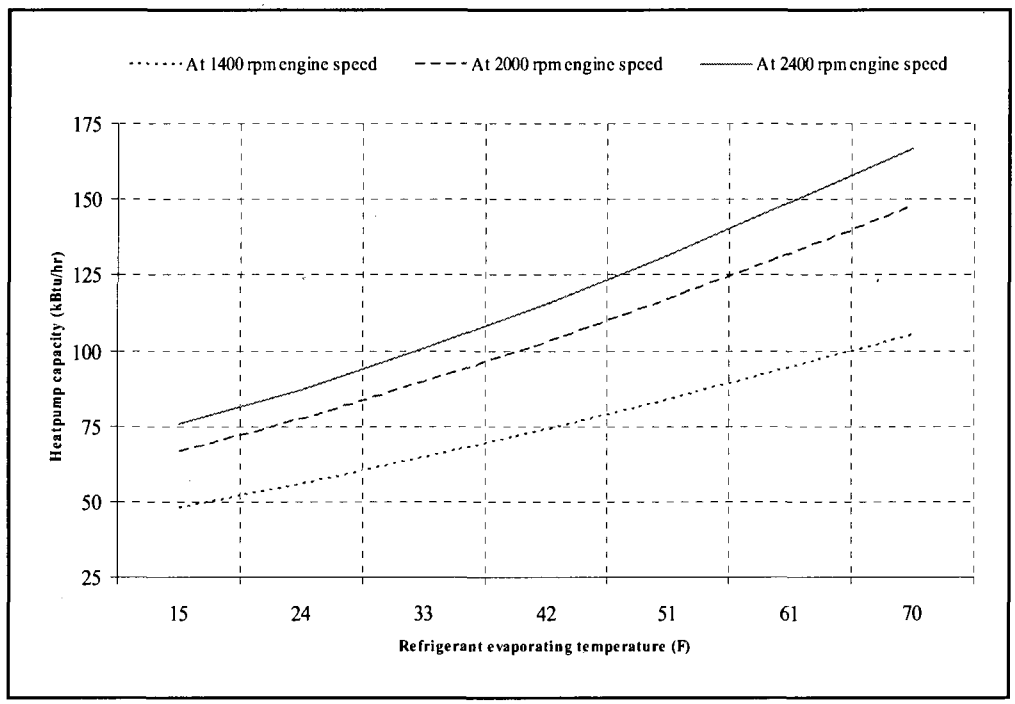

Figure 4.14 Heat Pump Capacity vs. Evaporating Temperature

This means that the temperature difference increased and this results in the diminishing of the heat pump capacity. The heat pump capacity variation is shown in Figure 4.14. At high engine speed (2400 rpm), the capacity of the heat pump falls by 54.6% when the evaporating temperature decreases from 70 to $15^{o}F$. The heat pump capacity could be improved by recovering the engine coolant/exhaust at the low ambient condition (it'll be discussed in the next section).

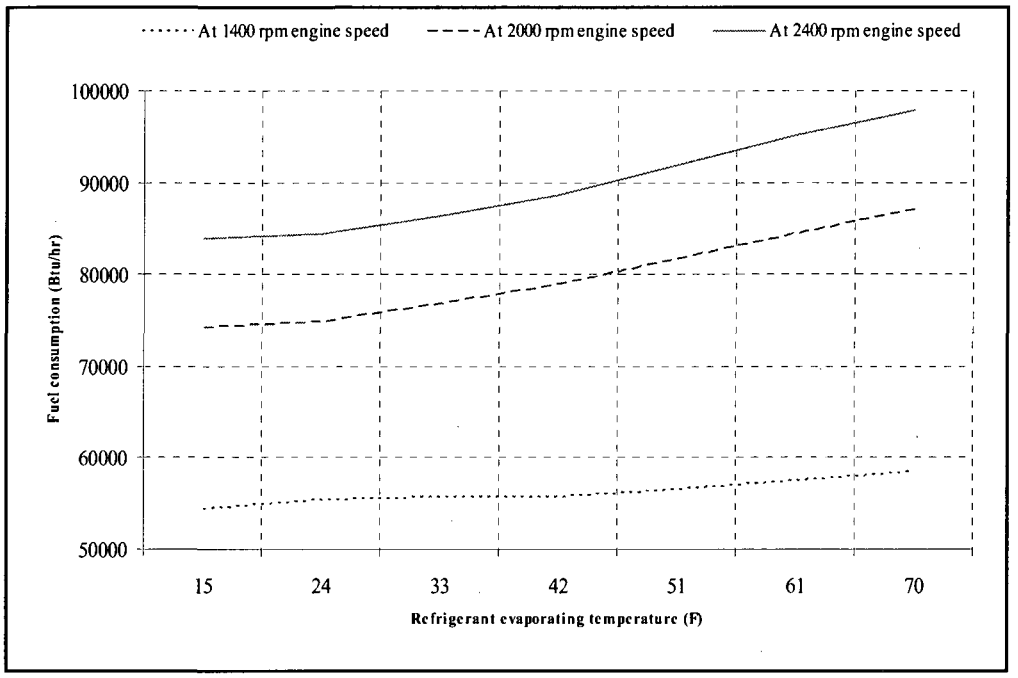

Figure 4.15 Fuel Consumption vs. Evaporating Temperature

The engine fuel consumption is not a strong function of the heat pump evaporating temperature especially at lower speeds. Figure 4.15 illustrates that the fuel consumption is significantly influenced by the engine speed. The fuel consumption increased by 48.6% and 67.4% when the engine speed increased from 1400 rpm to 2000 and 2400 rpm respectively.

As shown in Figure 4.16, the GHP power efficiency is proportional to engine speed and evaporating temperature increase. Here, the engine power efficiency is defined as:

$$\text{GHP power efficiency} = \frac{\text{Compressor input power}}{\text{Fuel consumption by the engine}} \qquad (4.3)$$

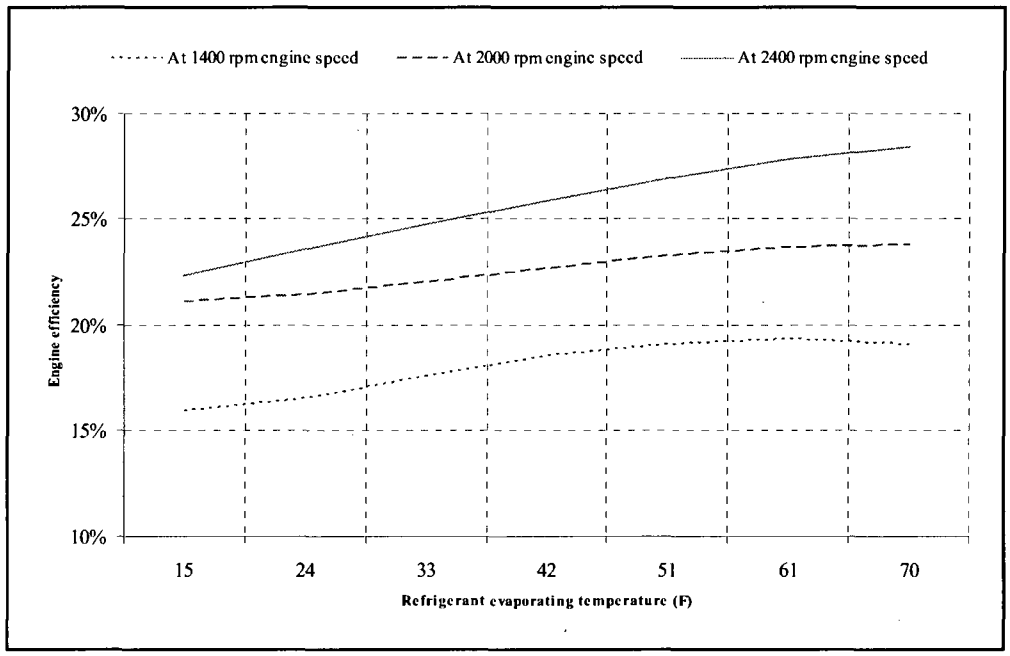

Figure 4.16 GHP Power Efficiency vs. Evaporating Temperature

In this section it is shown that the evaporating pressure (temperature), suction specific volume and the compressor rotation speed show influence on the mass flow rate, capacity and compressor input power. It is inferred that the evaporating pressure (temperature) has a larger influence on the refrigerant mass flow rate and capacity. The first conclusion inferred from the results is that the refrigerant mass flow rate is largely dependent on the evaporating temperature (pressure) which influences the suction specific volume, and therefore, on the suction conditions. Given the limited influence of the superheating and the rest of variables considered, it follows that the mass flow rate evolution is mainly governed by the compression ratio and more importantly by the evaporating pressure. Analyzing the refrigerating capacity it's been reached to the conclusion that the mass flow rate evolution becomes the most important influence on the refrigerating capacity behavior. With reference to the power input requirement to compressor, the consumption

tends to decrease more slowly with increasing compression ratios. The engine power efficiency tends to decrease as the evaporating temperature decreases.

4.2. Heating Performance Analysis with Suction Line Heat Recovery

In this section GHP's heating performance utilizing suction side heat recovery will be analyzed and discussed. Suction side heat recovery utilizes the engine heat to superheat the vapor exiting the evaporator coil. This mode essentially reduces the evaporator load, enabling it to operate at a slightly higher pressure. Figure 4.17 compares the heating performance of the GHP with and without heat recovery. The comparison is at engine speed of 2400 rpm and return air temperature $70°F$. The result shows a 21% capacity gain at a rated ambient temperature of condition of $47°F$.

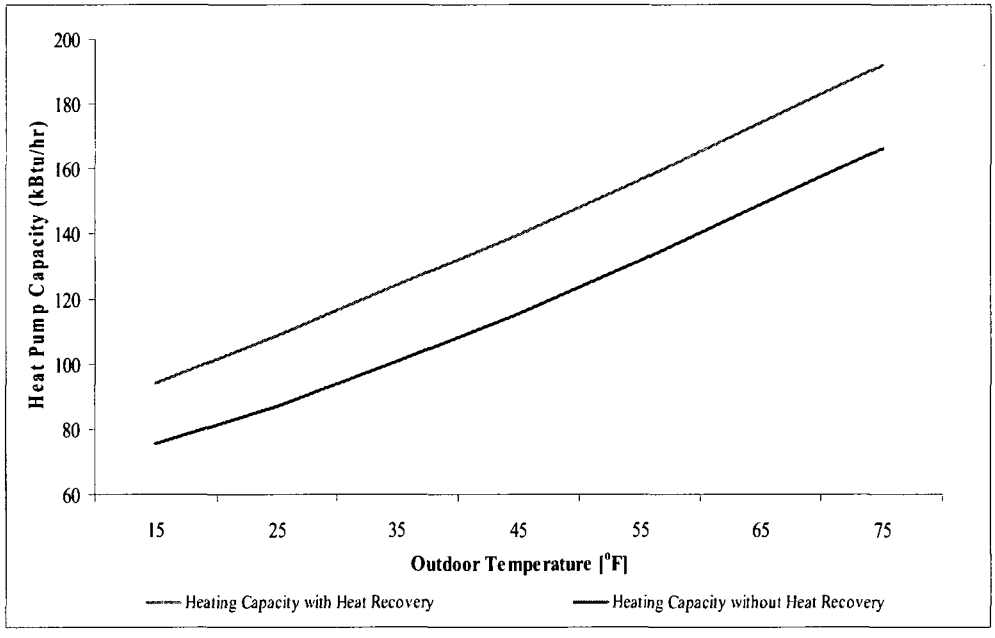

Figure 4.17 Heating Capacity of GHP vs. Outdoor Temperature

The heating characteristic of the GHP in different ambient temperatures is shown in Figure 4.18. The engine speed is set at 2400 RPM. When the ambient temperature increases, the heating capacity of the condenser increases much, while that of the waste heat increases a little. The reason is that the performance of an air source heat pump is affected much by the outdoor temperature, but the input power of the compressor changes little. Therefore, the performance of the gas engine is almost unchanged.

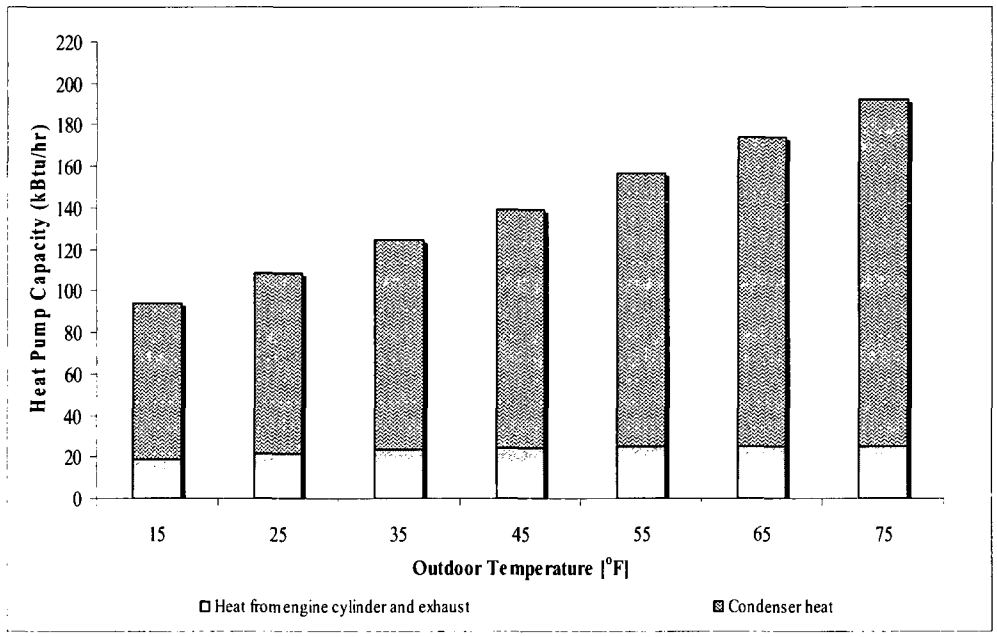

Figure 4.18 Heat Pump Capacity at Different Outdoor Temperatures

Essentially, by recovering the heat at the suction side (outlet of the evaporator) one is increasing the refrigerant discharge and suction temperatures. As illustrated in Figure 4.19 the suction and discharge temperatures increased from 12 to 67 ^{o}F and 147 to 191^{o}F (at 15^{o}F ambient temperature) and respectively when heat is recovered at the outlet of the evaporator.

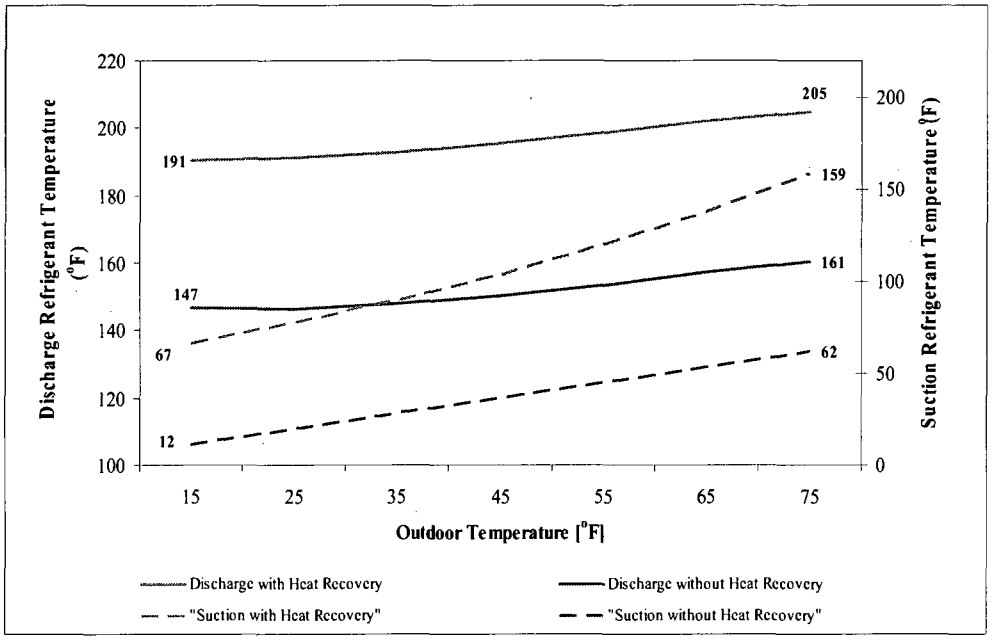

Figure 4.19 Discharge Refrigerant Temperature vs. Outdoor Temperatures

A heat pump heats a space thermodynamically. It will absorb heat from lower temperature ambient air or any other heat source and delivers it to the higher indoor temperature to maintain indoor thermal comfort. However, there is a major concern about the conventional heat pump operation during the heating mode operation. One is the "cold blow" that the conventional heat pump supply air temperature is generally low, which can cause a sensation of cold air blowing across the skin. When frost starts accumulating on the outdoor coil, the supply air temperature will be even lower. As shown in Figure 4.20, a GHP increases the supply air temperature by 4.5 and 6.3 ^{o}F at ambient temperatures of 15 and 75 ^{o}F respectively by utilizing the recovered heat.

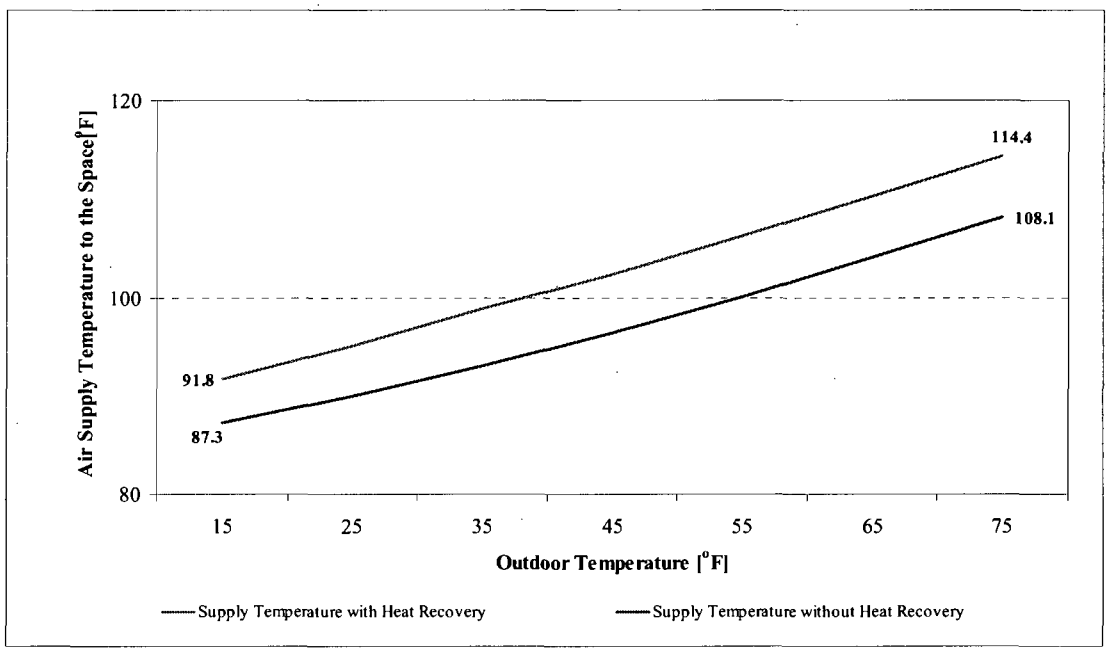

Figure 4.20 Supply air Temperature to the Space vs. Outdoor Temperatures

Figure 4.21 shows the variation of the system total heat pump coefficient of performance (COP_h) related to the ambient temperature when the engine speed is 2000 RPM. It is shown that the system COP_h increases much with the increase of temperature.

$$COP_h = \frac{Q_{cond} + Q_{rec}}{Engine_{fuel\_input}} \tag{4.4}$$

Where Q_{cond} and Q_{rec} are condenser heat (heat power supplied to the facilty) and engine wasted heat recovered by the refrigerant from the engine exhaust and coolant respectively.

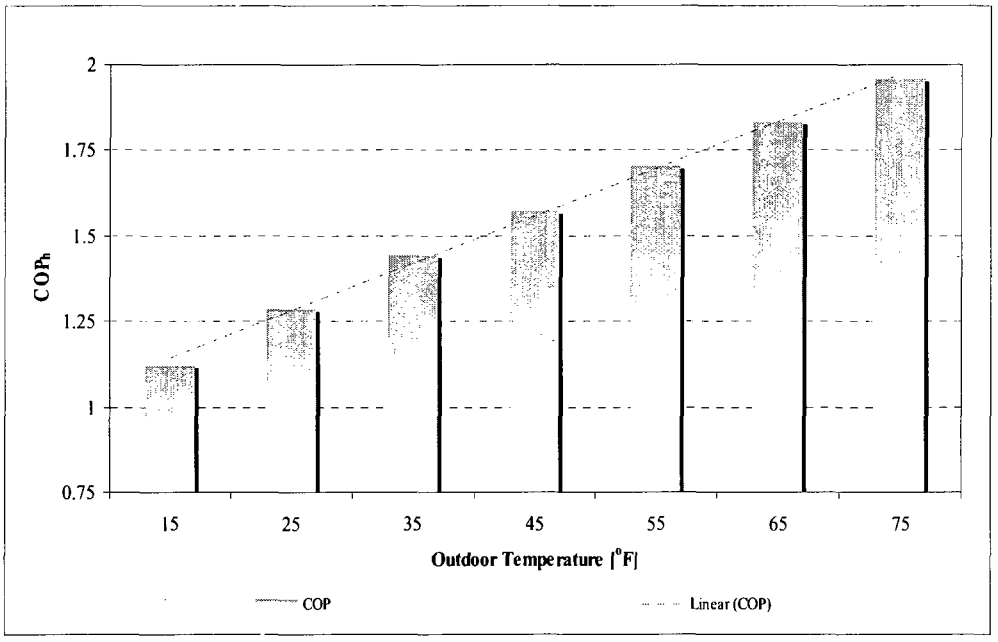

Figure 4.21 System Total Heating COP at Different Outdoor Temperatures

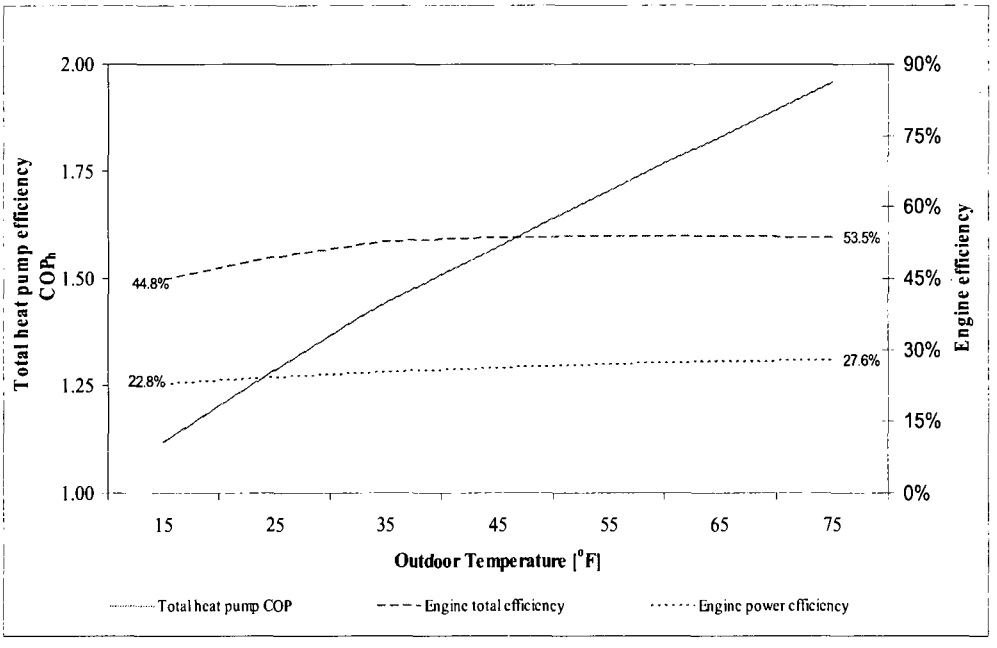

Figure 4.22 Engine and Heat Pump Efficiency vs. Outdoor Temperature

The performances of the heat pump and gas engine as affected by ambient temperature are shown in Figure 4.22. When the ambient temperature rises, both the heating efficiency and the engine power efficiency increase linearly, but the total energy efficiency of the engine increases at the beginning and levels later.

In this section the performance of the GHP is analyzed under various operating conditions. In particular, the heating performance of the gas engine and heat pump system is analyzed separately in order to investigate the mutual influence between the two parts. The results show that

A. the waste heat of the gas engine can take about 20-25% of the total heating capacity in rated operating condition;
B. the ambient temperature affects the performance of the heat pump but has little influence on the engine efficiency in the constant engine speed mode;
C. because of the limitation of speed, the GHP still needs extra equipment to back up the heating in extreme low ambient temperatures.

4.3. Analysis of Suction Liquid Line Heat Exchanger on Cooling Performance

In this section, the effect of a suction-gas/liquid-line heat exchanger (SGLLHX) on the performance of an R410A heat pump cycle will be analyzed. The liquid-suction heat exchanger affects the performance of a refrigeration system by influencing both the high and low pressure sides of a system. The enthalpy of the refrigerant leaving the condenser is decreased prior to entering the expansion device by rejecting energy to the vapor refrigerant leaving the evaporator prior to entering the compressor. Based on the CFD analysis of the heat exchanger the effect of pressure drop is insignificant compared to

system operating pressure. The cooling of the condensate that occurs on the high pressure side serves to increase the refrigeration capacity and reduce the likelihood of liquid refrigerant flashing prior to reaching the expansion device. On the low pressure side, the liquid-suction heat exchanger increases the temperature of the vapor entering the compressor and reduces the refrigerant pressure due to friction losses, both of which increases the specific volume of the refrigerant and thereby decreases the mass flow rate and capacity.

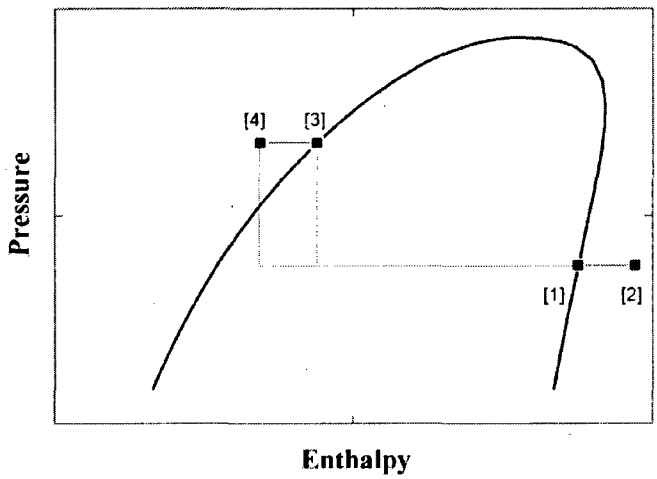

Figure 4.23 Pressure- Enthalpy Diagram

Without a liquid-suction heat exchanger, the refrigerating effect per unit mass flow rate of circulating refrigerant is the difference in enthalpy between states 1 and 3 in Figure 4.23. When the heat exchanger is installed, the refrigeration effect per unit mass flow rate increases to the difference in enthalpy between states 1 and 4. The extent of the capacity increase is a function of the specific refrigerant, the heat exchanger effectiveness, and the system operating conditions. Figure 4.24 illustrates the effect of a

liquid-suction heat exchanger on refrigeration capacity can be quantified in terms of a relative capacity change index (RCI) as defined in equation (4.5):

$$RCI = \left(\frac{Capacity_{LLSUC\_HEX} - Capacity}{Capacity} \right) \times 100\% \qquad (4.5)$$

Where:

$Capacity_{LLSUC\_HEX}$ is the refrigeration capacity with a liquid-suction heat exchanger

Capacity is the refrigeration capacity for a system operating at the same condensing and evaporating temperatures without a liquid-suction heat exchanger.

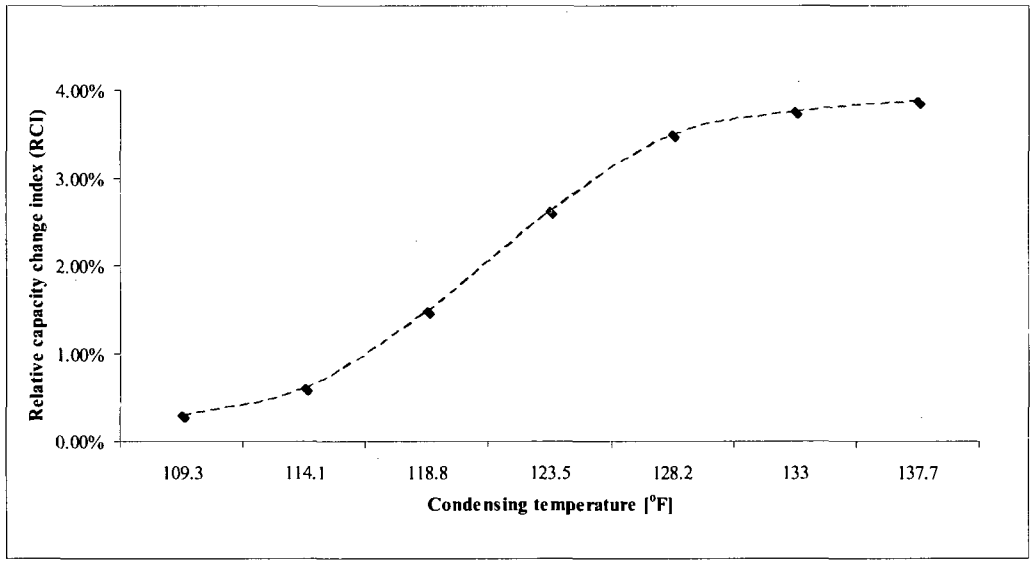

Figure 4.24 Effect of a SGLLHX on the Cooling COP of a R-410A Cycle

Figure 4.24 shows that the SGLLHX provides a small improvement in COP at high ambient temperatures, but that the advantage disappears at lower ambient. The predicted

effects of the SGLLHX on the liquid and suction temperatures are shown in Figure 4.25 at a condensing temperature of 125°F. The SGLLHX heat exchanger lowers the liquid temperature by 19°F, while raising the vapor temperature by 35°F.

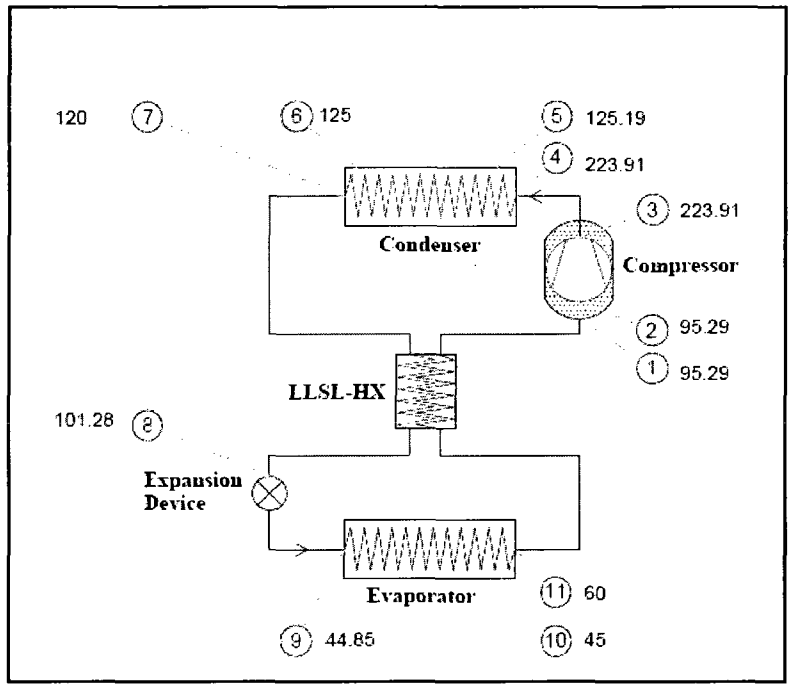

Figure 4.25 Refrigerant Temperatures for SGLLHX

A performance gain by using suction liquid line heat exchanger is shown especially at higher ambient conditions. Another major benefit of the liquid-suction heat exchanger is that it reduces the possibility of liquid carry-over from the evaporator which could harm the compressor. Liquid carryover can be readily caused by a number of factors that may include wide fluctuations in evaporator load and poorly maintained expansion devices. The economic factor will be the determining factor to incorporate this heat exchanger in the heat pump system.

CHAPTER 5

EXPERIMENTAL PERFORMANCE EVALUATION

5.1. Test Facility

The performance of the test unit was measured through the use of a psychrometric test facility at Oak Ridge National Heat pump Laboratory. Temperature conditioning for each thermally-activated heat pump chamber is provided by a dedicated glycol fluid loop which circulates glycol at he appropriate temperature through the fluid-to-air heat exchanger in the room. Additional temperature conditioning is provided by sheathed electric heaters located directly in the air stream.

Each glycol loop includes a pump, fluid heater and (2) refrigerant-to-glycol heat exchangers. The rooms share a common refrigeration plant consisting of three 30-horsepower compound compressors which provide mechanical refrigeration for the room glycol circuits as well as for the Direct-Expansion (DX) dehumidification coils in each room and the DX pre-cool and post-cool coils in the Makeup Air System. The three compound compressors are water-cooled utilizing refrigerant R507 (AZ50). The design temperature range for each room is from -20°F to +125°F with a ±1°F. The humidity range for the indoor chamber (small room) is 18 to 75% RH and the outdoor chamber (larger room) from 18 to 81% RH with humidity tolerances of ±1.5%. Humidity is provided from steam with a capacity of 75 lb/h at 30 psig supplied through a 1" NPT (National Pipe Thread) pipe. Each room has 18 kWs of air heaters in addition to 18kW of

glycol fluid heater. The test facility features a micro-processor-based control system designed around an Allen-Bradley PLC-5/20 Programmable Logic Controller (PLC). Multiple temperature and humidity control loops reside within the PLC, including several feed-forward and cascade control loops designed to optimize stability and maintain tight control tolerances even under rapidly-changing load conditions.

Temperature sensors are 100 ohm Resistance Temperature Detectors (RTD's) with dedicated 4-20mA transmitters. Humidity is monitored with true dew-point sensors (capacitive humidity sensors), providing a reliable indication of actual moisture content unaffected by air temperature. Room enclosures are constructed of 24 gauge embossed galvanized steel walls with foamed-in-place internal insulation, and a 16 gauge galvanized floor. The indoor chamber is 14' 8" x 11' 4" x 11' 10" and the outdoor chamber is 14' 8" x 19' 4" x 11'10".

The GHP was installed in the outdoor chamber with supply/return air from the indoor chamber. This air duct is sealed by a duct sealant to prevent air leakage, and wrapped with insulation to prevent heat losses. The duct size was determined according to ASHRAE Standard 40 [62]. Both supply and return used 20" round flexible insulated duct. The supply consists of a single piece 15 feet in length while the return consists of two pieces 12 ft in length each totaling 24 ft. The flexible ducts are insulated with an R-value of six. Figure 5.1shows the GHP inside the environmental chamber.

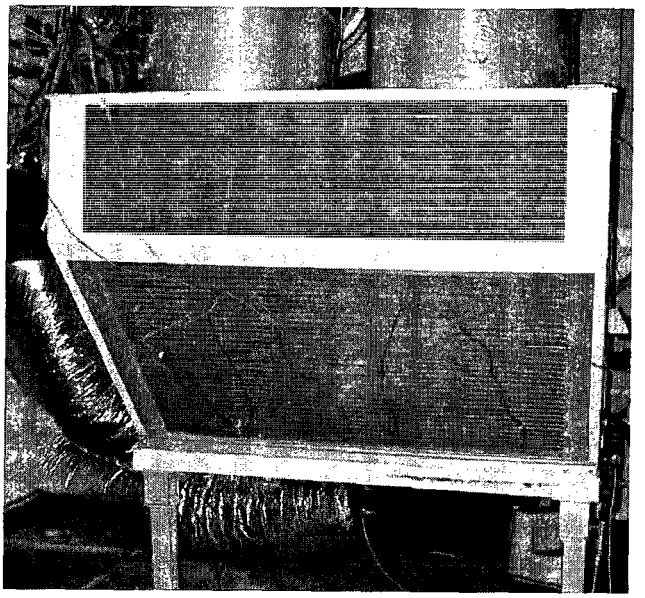

Figure 5.1 GHP in the Outdoor Chamber

5.2. Instrumentation and Measurement

Along with the test facility, instrumentation to measure the performance of the test unit was implemented. The instrumentation was designed to determine the properties of air and refrigerant. There are basically four types of measurements necessary to obtain the required data to calculate and evaluate the performance of the test unit. These are temperatures, pressures, mass flow rate, and power.

5.2.1. Temperature Measurement

The dry-bulb and dew-point temperatures of the return air were monitored by averaging thermistor (BAPI duct averaging thermistor) and chilled mirror (General Eastern Optica Hygrometer) respectively. The National Institute of Standards and Technology (NIST) traceable chilled mirror sensing technology of the Optica Hygrometer measures dew-point temperature by regulating the temperature of a polished metal mirror by the use of optical feedback such that a constant mass of dew or frost is

maintained. The Optica chilled mirror sensors provide a measurement range from -112°F to 185°F dew-point with 0.4°F or better accuracy.

The supply air dry-bulb and dew-point temperatures were monitored by averaging thermistor (BAPI duct averaging thermistor) and capacitive humidity sensor (Vaisala humidity sensor/transmitter) respectively. The Vaisala HMT337 warmed probe which provides NIST traceable measurement in near saturation environment.

5.2.2. Pressure Measurement

The transducers were directly connected to the piping system with tees. The transducers were calibrated by utilizing a pressure calibrator (Omega, PCL5000) after installation into the system. The correlation obtained from the calibration was used in the data acquisition program to convert voltage output into pressure values.

5.2.3. Refrigerant Mass Flow Rate Measurement

Refrigerant, coolant and natural gas mass flow was measured with a Coriolis type mass flow meter. The output signal of 4-20 mA was adjusted to correspond to a range for refrigerant R-410A, coolant and natural gas by using a transmitter calibrator.

5.2.4. Air Flow Measurement

Fan evaluators (Air Monitor Corporation) were used to monitor the supply air and outdoor flow rates. The fan evaluator is a multi-point, self-averaging Pitot traverse station with integral air straightener-equalizer honeycomb cell, capable of continuously measuring fan discharges or ducted airflow. For the supply air, a 4.5 ft^2 (18" x 36" rectangular) the fan evaluator unit was used with 27" straight-run upstream and downstream of the unit. A differential pressure transducer (Veltron DPT2500-plus, accuracy 0.25% of natural span) calibrated for this evaluator was used to monitor the

supply air flow. For the outdoor flow rates from the two fans, two 24" circular ducts (3.14 ft^2) fan evaluator units were used with 24" straight-run upstream of each unit. Two differential pressure transducers (accuracy 0.25% of natural span) calibrated for these evaluators were used to monitor the outdoor air flow rates.

5.2.5. Power Measurement

Ohio Semitronics, Inc. (OSI) watt-transducer was used to monitor the total electric power consumption of the GEDAC unit. This included the power used by the indoor blower. The OSI unit is a self-powered 0-5 VDC output for 0-5 kW with accuracy of ±0.5% of full scale.

5.2.6. Data Acquisition

Signals from all instruments were fed to a LabView data acquisition software package through the use of National Instruments' FieldPoint DAQ modules. These modules allow for flexibility in instrumentation, as additional channels may be added or removed easily if required later. These modules may also be placed close to the individual parts of the experiment (rather than the computer), eliminating both excessive cable lengths, and problems arising from incorrect wiring. A total of 96 channels of data were collected (64 thermocouples and 32 analog inputs) and sent to the computer for collection and instantaneous on-screen visualization of system parameters (e.g. pressures, temperatures, air flow rates, etc.). The tested sampling rate of this system was 1 minute. Numeric outputs monitored include air side temperatures, air flow rates, dew points, performance (including COP, compressor work, and both latent and sensible cooling loads), refrigerant pressures, mass flow rate, and in-stream temperatures. The graphical portion of the program monitored the history of many of these same measurements. When all measured

data reached steady state within 1% variation (temperature variation less than 0.1°F) for more than 30 minutes, the data collection was started for one hour.

Table 5.1 Major Test Instrumentation and Measurement Accuracies

Measurement	**Sensor**	**Range**	**Accuracy**
Temperature	Strap-on thermistors	-67 to 302°F	±0.4°F (32 to 158°F)
Average Temperature	Duct averaging thermistor	-67 to 302°F	±0.4°F (32 to 158°F)
Refrigerant pressures	Transducer	0 to 750 psig	±0.25% of full scale
Coolant pressures	Transducer	0 to 25 psig	±0.25% of full scale
Indoor Air flow	Fan Evaluator	0 to 4,400 cfm	±2%
Outdoor Air flow	Fan Evaluators	0 to 6,000 cfm	±2%
Coolant flow	Coriolis mass flow sensor	0 to 7,500 lb/h	±0.5%
Natural Gas Flow	Coriolis mass flow sensor	0 to 20 lb/h	±0.06 lb/h
Refrigerant flow	Coriolis mass flow sensor	0 to 2,000 lb/h	±0.1%
Dew-Point Temperature	Chilled mirror	-40 to 140°F	±0.2°F
Humidity Transmitters (Dew-Point)	Capacitive humidity sensor	-40 to 212°F	±0.4°F
Rotational speed	Portable tachometer	0 to 5000 rpm	±0.1%
Electric power	Watt transducer	0 to 5 kW	±0.5% of full scale

Sensors used for these measurements and associated accuracies are shown in Table 5.1. The required accuracy of the test instrumentation is in accordance with [63-67]. Piping and instrumentation diagram of the GHP is shown in Figure 5.2.

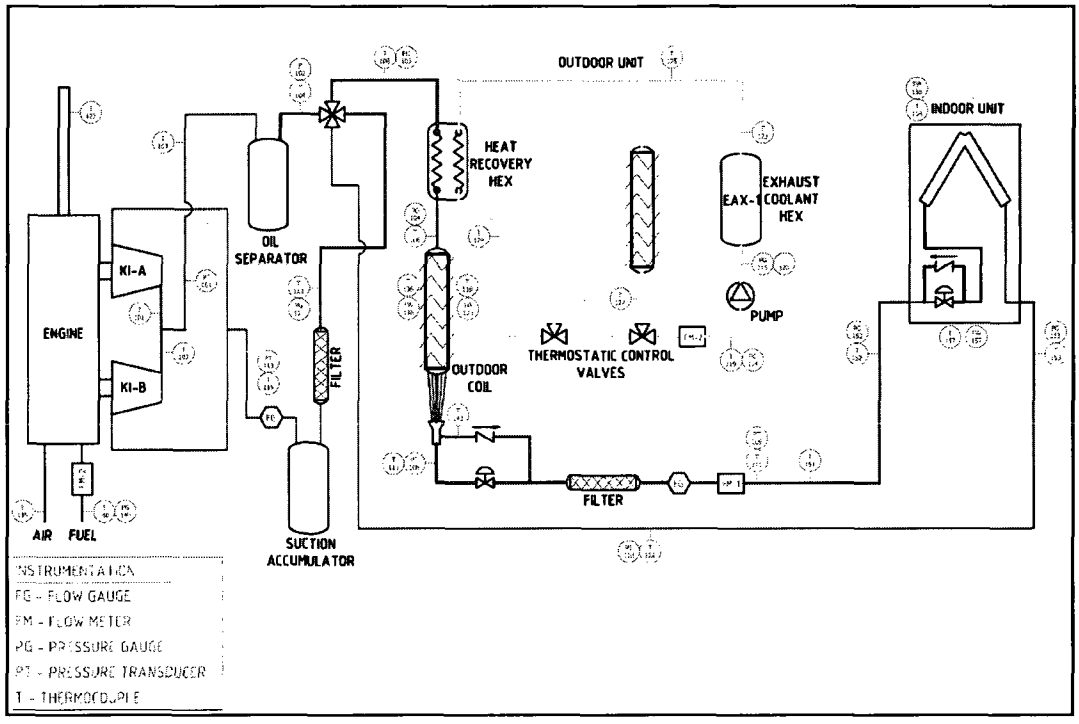

Figure 5.2 Piping and Instrumentation Diagram of the Tested GHP

5.3. Performance Evaluation

The performance of the test unit was evaluated in terms of its capacity and COP as described below. To evaluate the capacity experimentally, the air-side capacity and refrigerant-side capacity were calculated from the measured data.

5.3.1. Air-Side Capacity

The sensible air-side capacity (q_{si}) was calculated by equation (5.1) ASHRAE Standard 37 [68].

$$q_{si} = \frac{60 Q_{mi} C_{pa} (t_{ain} - t_{aout})}{v_n' (1 + W_n)} \tag{5.1}$$

where:

Q_{mi} : air flow, indoor, measured, $\left(\frac{ft^3}{\min} \right)$

C_{pa} : Specific heat of air

t_{ain} : Air temperature entering the indoor unit

t_{aout} : Air temperature leaving the indoor unit

v_n' : Specific volume of air at orifice throat

W_n : Humidity ratio of air at orifice throat

The latent air-side capacity (q_{lci}) was calculated from the humidity ratio difference between inlet and outlet by equation (5.2).

$$q_{lci} = \frac{63600 Q_{mi} (W_{i1} - W_{i2})}{[v_n' (1 + W_n)]} \tag{5.2}$$

where:

W_{i1} : Humidity ratio of air entering the indoor unit

W_{i2} : Humidity ratio of air leaving the indoor unit

Then the total air-side capacity is calculated by summing up the sensible air-side capacity and the latent air-side capacity.

5.3.2. Refrigerant-Side Capacity

The refrigerant-side capacity (q_{ref}) was calculated using the mass flow rate of refrigerant and enthalpy difference between inlet and outlet of the evaporator. The

evaporator inlet enthalpy was obtained from the expansion valve inlet enthalpy by assuming an isenthalpic expansion process. These enthalpies were calculated based on the measured pressures and temperatures by using thermodynamic property routines [69]. Then the refrigerant-side capacity (q_{ref}) was calculated using equations (5.3).

$$q_{ref} = m_{ref}(h_{out} - h_{in}) \tag{5.3}$$

where:

m_{ref}: refrigerant mass flow rate

h_{in}: enthalpy of refrigerant at the indoor unit inlet

h_{out}: enthalpy of refrigerant at the indoor unit outlet

To confirm that the data are reliable, the capacity determined using these two methods should agree within 6% of each other as required by ASHRAE Standard 116 [70]. The reported capacity and COP values were based on refrigerant-side values. The air-side values were used only to check the total energy balance.

5.3.3. Coefficient of Performance (COPs)

COPs were calculated for both the air-side and the refrigerant-side based on the capacity and fuel consumption

5.4. Error Analysis

During experimentation, the bias (or systematic) error and the precision (or random) error are two important parameters to be mindful of Beckwith et al.[71]. Detailed error analysis to determine the magnitude of these values is described as follows. The bias error is an uncertainty that occurs in the same way each time a measurement is made. The

total uncertainty of a measurement due to the uncertainty of individual parameters is referred to as the propagation of uncertainty [71]. Also referred to as bias, the total uncertainty of any function may be calculated using the Pythagorean summation of uncertainties which is defined by equation (5.4) [72]:

$$U_F = \sqrt{\left(\frac{\partial F}{\partial v_1}u_1\right)^2 + \left(\frac{\partial F}{\partial v_2}u_2\right)^2 + \left(\frac{\partial F}{\partial v_3}u_3\right)^2 + \cdots + \left(\frac{\partial F}{\partial v_n}u_n\right)^2} \tag{5.4}$$

where:

U_F = uncertainty of the function

u_n = uncertainty of the parameter

F = function

v_n = parameter of interest (measurement)

n = number of variables

The partial derivatives of each independent measurement for the relevant calculated parameters were determined using the uncertainty propagation function in the Engineering Equation Solver (EES), and applied within the program to the root mean square (rms) outcome. The results of this effort are shown in Table 5.2.

The precision error is different for each successive measurement but have an average value of zero. This minimum/maximum error in the measurements of importance was calculated with a spreadsheet based upon the rated deviation of the system's instrumentation. The precision error was calculated to have a confidence level of 99.7%. After evaluating the bias and precision errors, the total errors are calculated by summing up these two errors.

Table 5.2 shows the results of the total error calculation. From this, it was determined that the air side calculations for capacity and COP generated the most uncertainty, primarily due to the accuracy of the instruments involved in the measurement, and this is the reason for reporting the refrigerant-side performance as the primary method

Table 5.2 Measurement Error

Parameter	Air-side capacity	Air-side COP	Refrigerant capacity	Refrigerant COP
Bias error (%)	±0.9	±0.9	±1.6	±2.5
Precision error (%)	±3.2	±3.2	± 0.7	± 0.9
Total error (%)	±4.1	±4.8	±2.3	±3.4

5.5. Test Procedure

The GHP unit was operated over a wide range of ambient conditions including the operating conditions for standard rating and performance tests [73-75]. These operating conditions are shown in Table 5.3 and Table 5.4 for heating and cooling modes. It should be noted that the unit was charged with 25 lb of R410A. Evaluations were conducted at:

- High engine speed (2,400 rpm),
- Intermediate engine speed (2,000 rpm) and
- Low engine speed (1,400 rpm)

The evaluation was conducted at Oak Ridge National laboratory environmental chamber. Wide range of tests at various indoor dry bulb and wet bulb temperatures were conducted.

Table 5.3 Operating Conditions for Evaluation of GHP in Cooling Mode

	OUTDOOR	INDOOR	Engine	Part Load
	Air Entering DB/WB/DP	Air Entering DB/WB/DP	Speed	(PLR)
	(°F)	(°F)	(rpm)	
Standard Rating Conditions, SS	95/75/66.5	80/67/60.2	1,400-2400	
		80/70/65.3	1,400-2400	
		75/63/55.8	1,400-2400	
		67/57/49.8	1,400-2400	
Cooling SS	80/65/55	80/67/60.2	1,400-2400	
SS Dry Coil	80/65/55	80/57/36.8	1,400-2400	
Low Temperature	67/57/49.8	67/57/49.8	1,400-2400	
		75/63/55.8	1,400-2400	
		80/67/60.2	1,400-2000	
Maximum Conditions	115/75/55	80/67/60.2	1,400-2200	
		75/63/55.8	1,400-2200	
High Temperature	110/75/58.2	80/67/60.2	1,400-2400	
Higher Temperature	120/75/51.3	80/67/60.2	1,400-2000	
Highest Temperature	125/75/47.1	80/67/60.2	1,400-1650	

Table 5.4 Operating Conditions for Evaluation of GHP in Heating Mode

	OUTDOOR	INDOOR UNIT	Engine	Part Load
	Air Entering DB/WB/DP	Air Entering DB/WB/DP	Speed	(PLR)
	(°F)	(°F)	(rpm)	
Standard Rating Conditions	47/43/38.7	70/60/53.5 (max)	1,400-2400	
		65/55.8/48.8	1,400-2400	
		75/64.2/58.2	1,400-2000	
High Temperature Steady State	62/56.5/52.7	70/60/53.5 (max)	1,400-2400	
		75/64.2/58.2	1,400-2400	
Steady State	17/15/9.4	70/60/53.5 (max)	1,400-2400	
		65/55.8/48.8	1,400-2400	
Maximum	75/65/59.5	80/68.5/62.8	1,400-2000	

5.6. Cooling Mode Experimental Results and Analysis

The cooling capacity of the GHP as a function of ambient temperature is shown in Figure 5.3. Ambient air temperature plays an important role in the cooling capacity of an air cooled heat pump system.

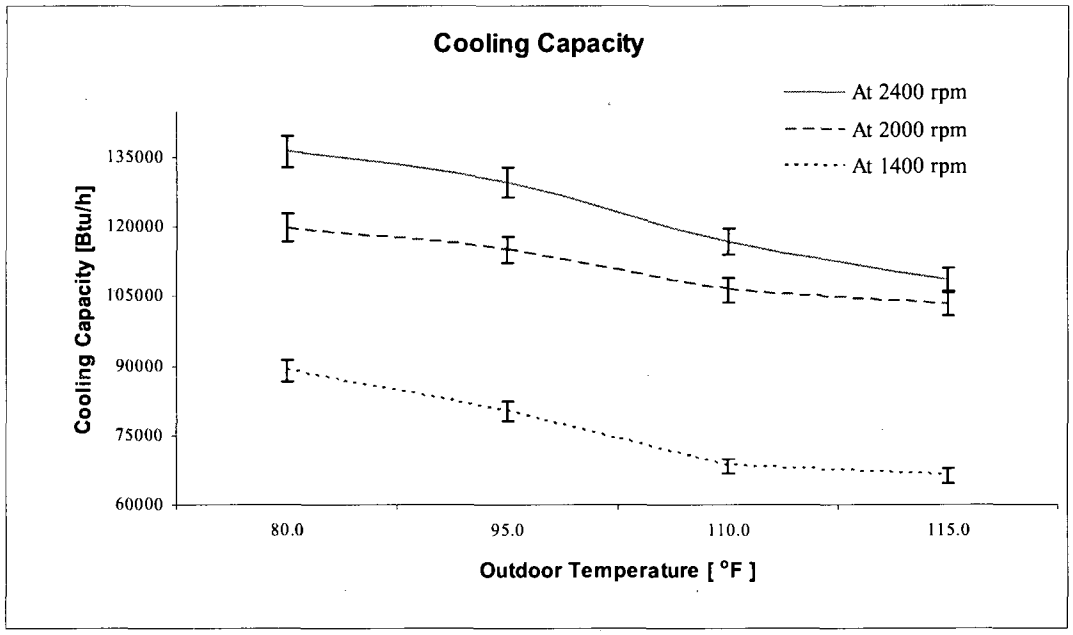

Figure 5.3 Cooling Capacity vs. Ambient Temperature

In order for the condenser to reject the total heat (process heat load plus heat of compression) to the ambient air, the temperature difference between the hot refrigerant gas and the ambient air must be sufficient. As the ambient air temperature increases, the ability of the condenser to transfer the process heat from the refrigerant to the ambient air is reduced, causing higher condensing temperatures and pressures that could result in reduced system performance.

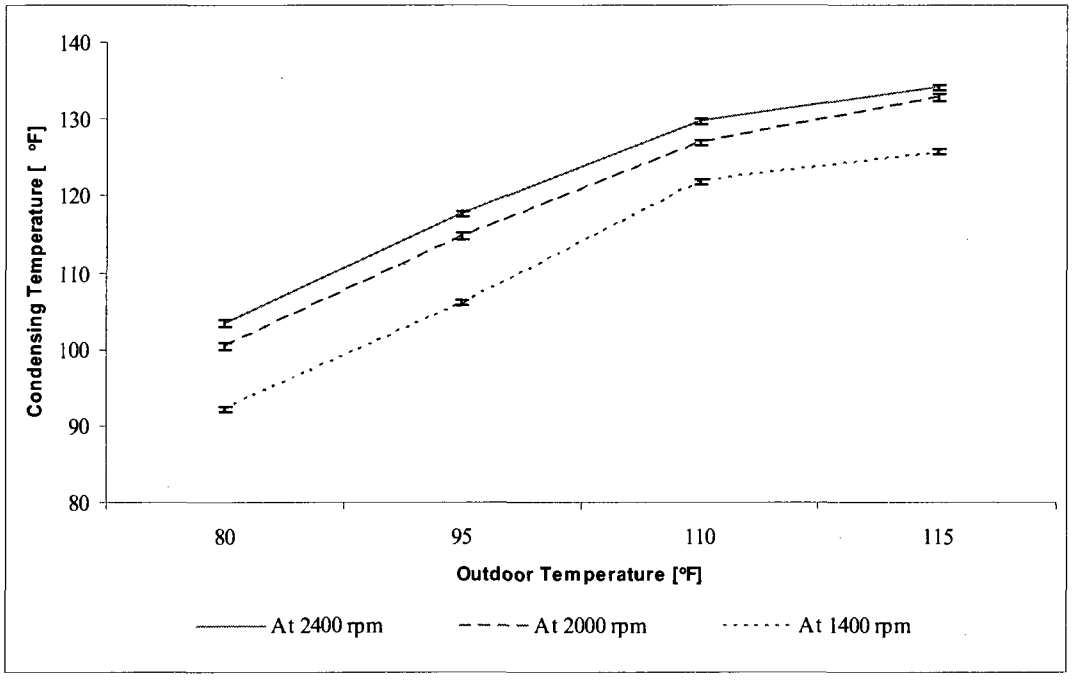

Figure 5.4 Condensing Temperature vs. Outdoor Temperature

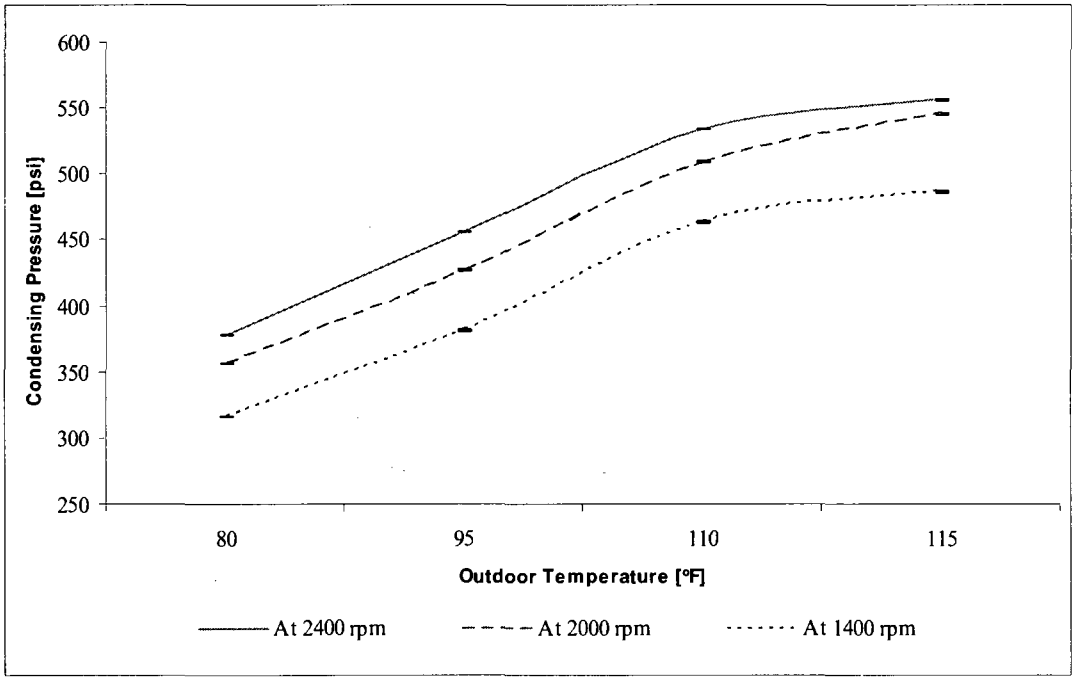

Figure 5.5 Condensing Pressure vs. Outdoor Temperature

Similarly, if the ambient temperature decreases, the performance will improve due to the larger initial temperature differential. Figure 5.4 and Figure 5.5 show the relationship between the condensing temperatures and pressures as a function of ambient temperature.

As shown in Figure 5.6 and Figure 5.7, the refrigerant compression ratio and fuel consumption by the engine increase as the ambient temperature increases. Higher condensing pressures caused by higher condensing temperature lead to higher compression ratios. Higher compression ratio requires higher power input by the engine to the compressor and higher fuel consumption by the engine.

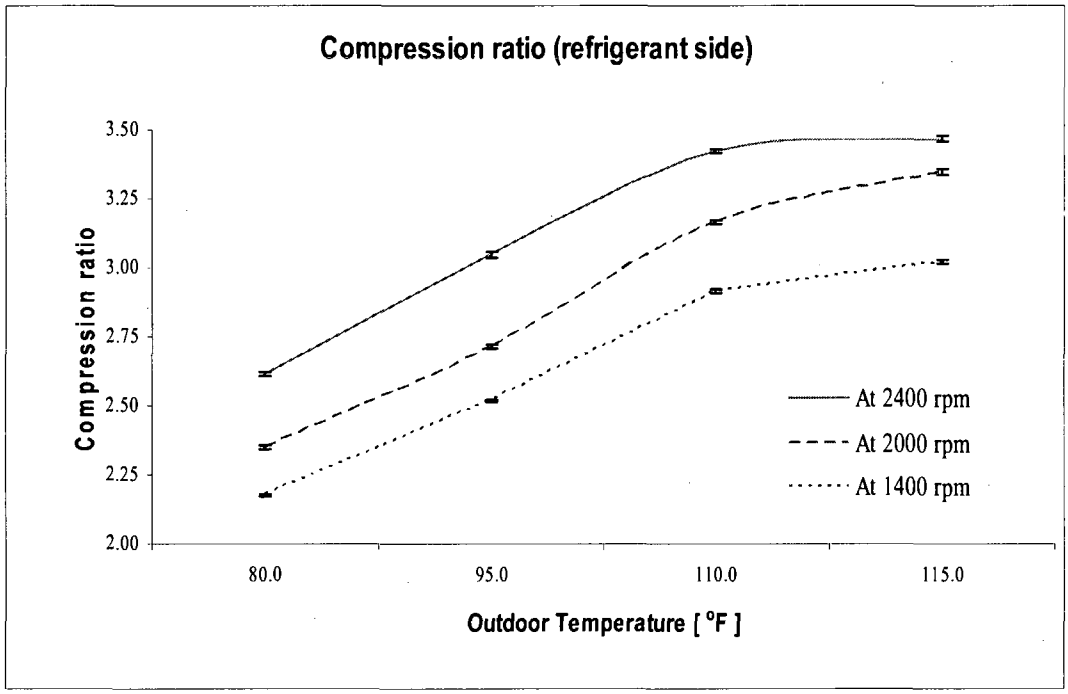

Figure 5.6 Compression Ratio vs. Outdoor Temperature

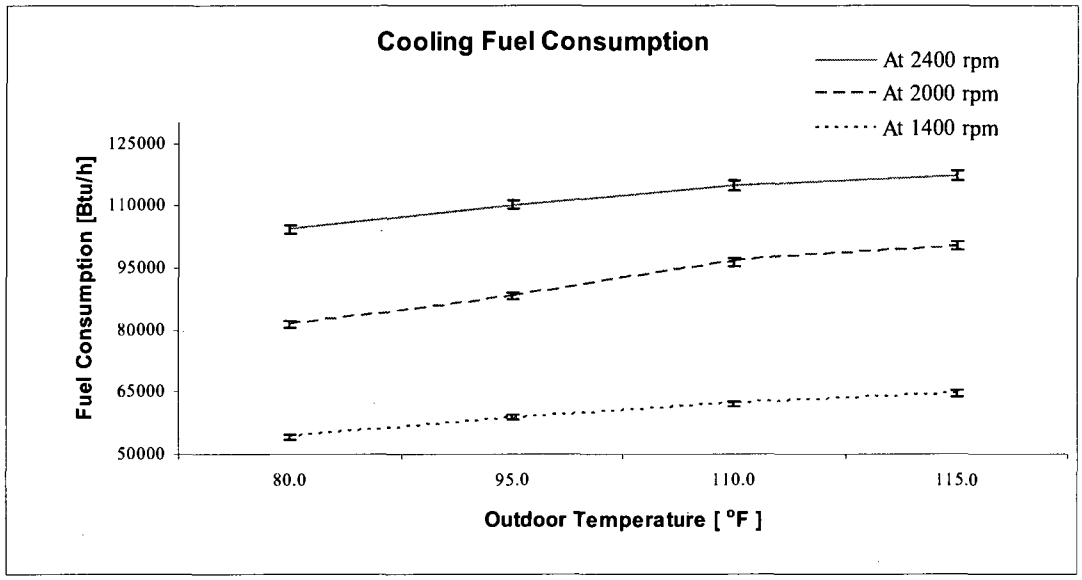

Figure 5.7 Fuel Consumption vs. Outdoor Temperature

In order to quantitatively evaluate the performance of any heat pump system, a figure of merit must be established. For a heat pump system utilizing a vapor compression refrigeration cycle, the efficiency is expressed in terms of the cooling/heating coefficient of performance or the COP. The coefficient of performance is a dimensionless quantity. It is the ratio of the rate of cooling or heating capacity to the power input. In this study, the COP is expressed as:

$$COP = \frac{Cooling_{capacity}}{Engine_{fuel\_input}} \tag{5.5}$$

Figure 5.8 shows a decrease in COP at elevated ambient temperatures. Operation of an air conditioner at elevated ambient temperatures inherently results in a lower COP. This conclusion comes directly from examining the Carnot cycle. The COP relation indicates that the COP decreases when the condenser temperature increases at a constant evaporation temperature.

$$COP_{Carnot} = \frac{T_{evap}}{(T_{cond} - T_{evap})} \tag{5.6}$$

This theoretical indication derived from the reversible cycle is valid for all refrigerants. For refrigerants operating in the vapor compression cycle, the COP degradation is greater than that for the Carnot cycle. A COP of 1.37, 1.30, and 1.18 is achieved at a rated condition of 95 °F outdoor temperatures for low, intermediate and high engine speeds respectively.

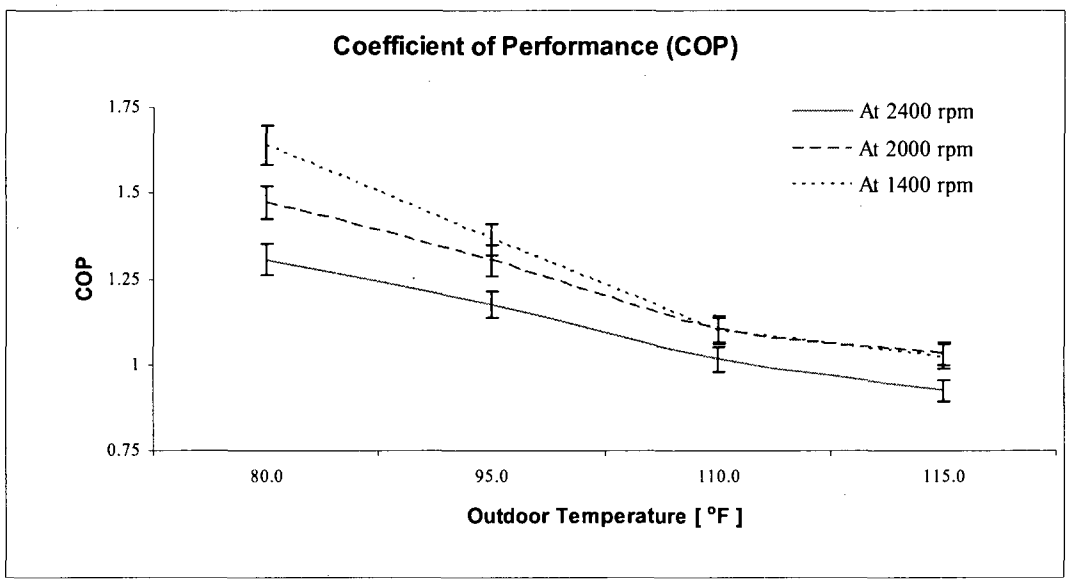

Figure 5.8 Cooling COP vs. Outdoor Temperature

5.7. Heating Mode Experimental Results and Analysis

Figure 5.9 shows the heating capacity as a function of ambient temperature and engine speed. This is the total capacity including heat recovered from the engine coolant. The heating capacity is highly a function of ambient temperature. The heating capacity

decreased by 52.3%, 52.25% and 47.9% when the ambient temperature dropped from 62 to 17 °F at 1400, 2000 and 2400 rpm engine speeds respectively.

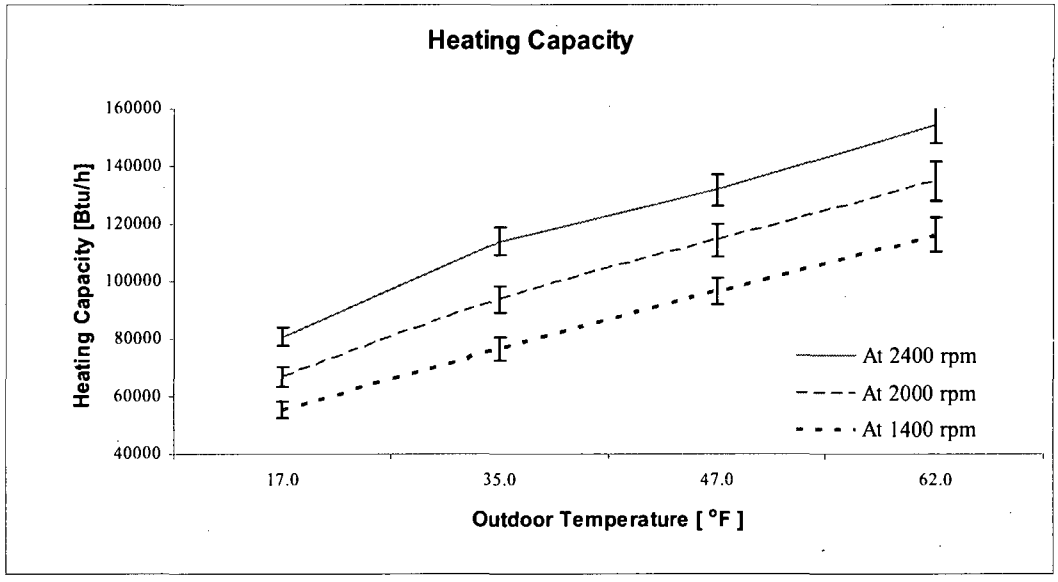

Figure 5.9 Heating Capacity vs. Outdoor Temperature

The fuel consumption on average increased by 18% when the ambient temperature lowered from 62 to 17 °F. The fuel consumption also increased by 27.6 % and 23.3% when the engine speed rose from 1400 to 2000 rpm and 2000 to 2400 rpm respectively. The overall heat pump capacity is the highest at the lowest engine speed. This is due to low fuel consumption at the lowest engine speed and relative minimal increase of heat recovery as the engine speed increases. As shown in Figure 5.11, at rated 47 F outside air, a COP of 1.65, 1.53, and 1.43 is achieved at engine speed of 1400, 2000, and 2400 rpm respectively.

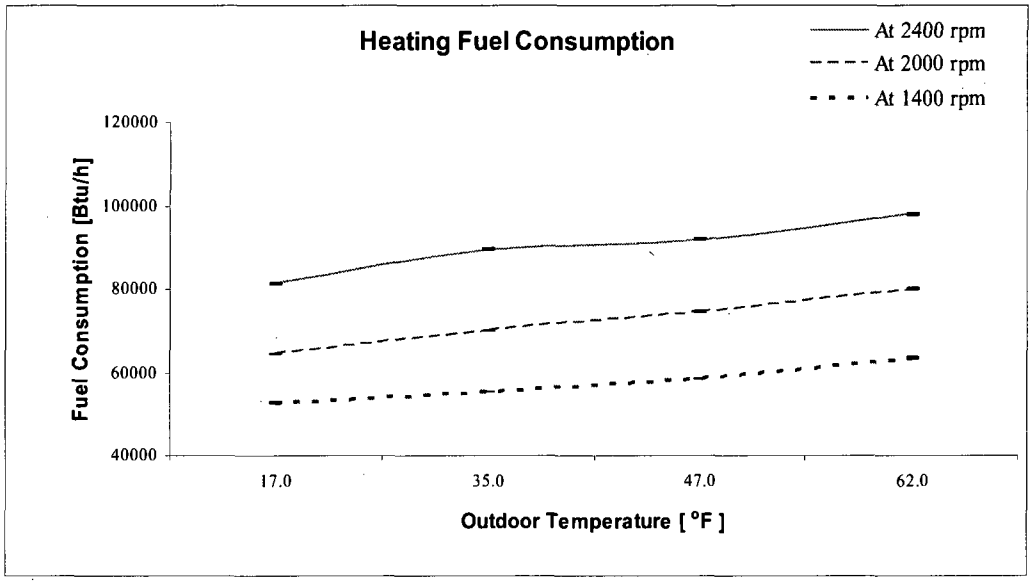

Figure 5.10 Fuel Consumption vs. Outdoor Temperature

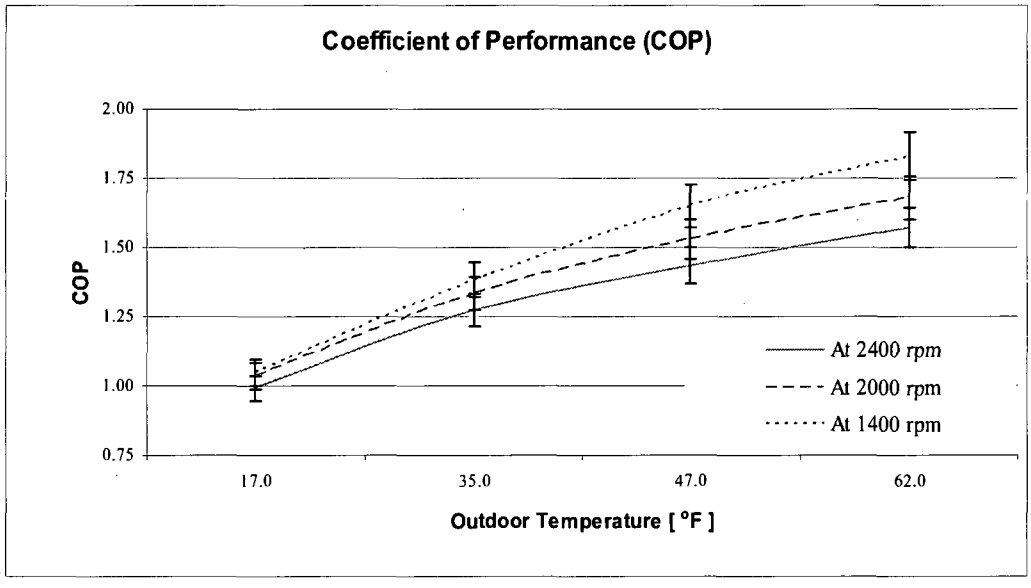

Figure 5.11 Heating COP vs. Outdoor Temperature

The heating characteristic of the GHP in different ambient temperatures is shown in Figure 4.18. As stated in the heating modeling section, when the ambient temperature

increases, the heating capacity of the condenser increases a great deal, while that of the waste heat increases only a little. The reason is that the performance of an air source heat pump is affected grestly by the outdoor temperature, but the heat output of the engine changes relatively less. Therefore, the performance of the gas engine is almost unchanged.

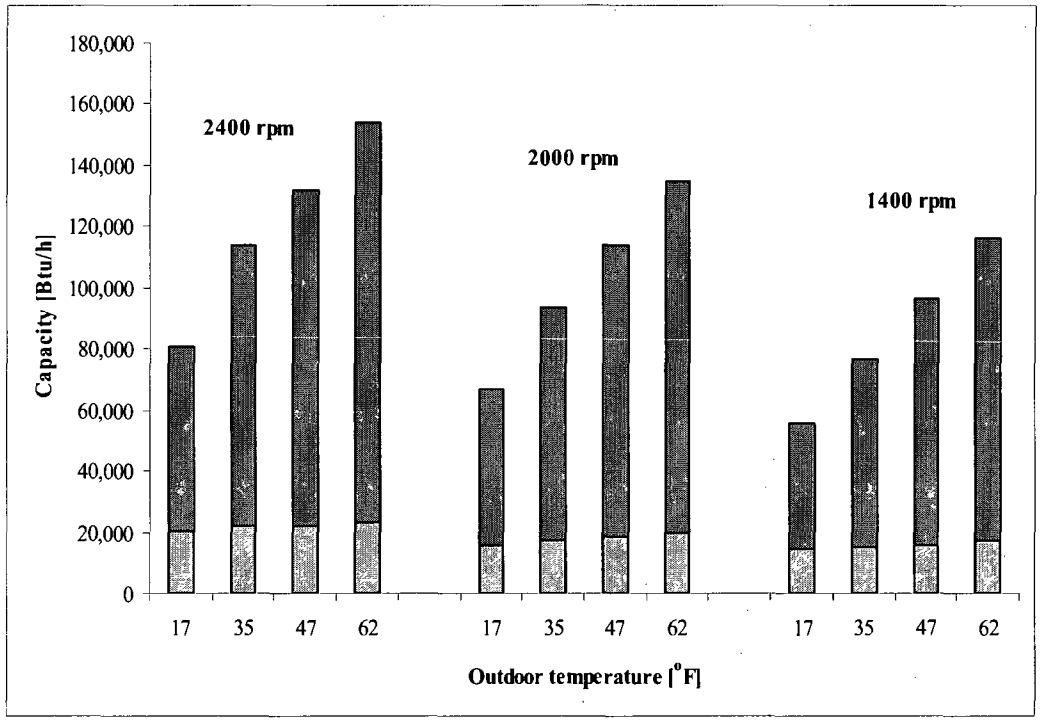

Figure 5.12 Heating Capacity as a Function of Outdoor Temperature

As the speed of IC engine increases, friction losses increase. Higher torque is also achieved using fuel enrichment, which reduces efficiency. At lower torque, the engine suffers most from what is termed pumping loss (the flow of air into the cylinders is restricted by closing a throttle valve). For the heating case run the optimum efficiency the engine produces around 26.7% of its rated peak power at 2000 rpm.

CHAPTER 6

THERMAL LOAD SIMULATION AND COST ANALYSIS

6.1. Description of Modeling Software and Simulated Building

As illustrated in the modeling and experimental section, the technology of GHP has a potential to play a vital role in reducing end-user energy consumption, cost, and greenhouse gas emissions. In order to effectively award end-users with these benefits, the technology must be applied appropriately. To determine the appropriateness of the technology in various applications, thermal simulation software called, EnergyPlus, can be used to compare the GHP with other air-conditioning options. Within this section, EnergyPlus is used to compare the GHP to its most common counterparts: an electrical DX heat pump and an AC unit with a gas furnace for heating. The three units were assumed to provide cooling and heating for a 5000 ft^2 office building. Both the building and the units were simulated for arid and cold climates. The energy consumption, energy cost, and CO_2 emission were calculated for each unit and were used for comparison.

EnergyPlus is an energy analysis and thermal load simulation program. Based on the user's description of a building, EnergyPlus will calculate the heating and cooling loads necessary to maintain thermal control set-points, which are matched with user-defined performance curves of HVAC systems. These curves, for an air-source heat pump, consist of the following:

A. The normalized total cooling (or heating) capacity modifier curve, *CAP* (function of temperature) is a biquadratic curve with two independent variables: wet-bulb temperature of the air entering the cooling coil, T_{wb_in}, and dry-bulb temperature of the air entering the air-cooled condenser coil, T_{db_o} (for heating calculations, the curve has to be a function of the indoor and the outdoor dry-bulb temperature). Normalized total capacity is the ratio of the capacity at any operating conditions to the capacity at the rated conditions. Equations 1 and 2 show the general form of the function for cooling and heating respectively.

$$CAP = a + bT_{wb\_in} + cT_{wb\_in}^2 + dT_{db\_o} + eT_{db\_o}^2 + fT_{wb\_in}T_{db\_o} \quad (6.1)$$

$$CAP = a + bT_{db\_in} + cT_{db\_in}^2 + dT_{db\_o} + eT_{db\_o}^2 + fT_{db\_in}T_{db\_o} \quad (6.2)$$

B. The normalized total cooling/heating capacity modifier curve (function of flow fraction) is a quadratic or cubic curve with the independent variable being the ratio of the actual air flow rate across the cooling coil to the rated air flow rate (i.e., fraction of full load flow).

C. The normalized energy input ratio, *EIR*, modifier curve (function of temperature) is a biquadratic curve with two independent variables: wet-bulb temperature of the air entering the cooling coil, and dry-bulb temperature of the air entering the air-cooled condenser coil (for heating calculation, the curve has to be a function of the indoor and the outdoor dry-bulb temperature.) EIR is defined as the ratio of the energy input to the capacity (inverse of the COP). Normalized EIR is the ratio of EIR at any operating

$$EIR = a + bT_{wb\_in} + cT_{wb\_in}^2 + dT_{db\_o} + eT_{db\_o}^2 + fT_{wb\_in}T_{db\_o} \quad (6.3)$$

$$EIR = a + bT_{db\_in} + cT_{db\_in}^2 + dT_{db\_o} + eT_{db\_o}^2 + fT_{db\_in}T_{db\_o} \quad (6.4)$$

D. The normalized energy input ratio (EIR) modifier curve (function of flow fraction) is a quadratic or cubic curve with the independent variable being the ratio of the actual air flow rate across the cooling coil to the rated air flow rate (i.e., fraction of full load flow).

E. The part load fraction correlation, *PLF* (function of part load ratio, *PLR*) is a quadratic or cubic curve with the independent variable being part load ratio (abbreviated as PLR and is defined as the sensible cooling or heating load divided by the steady-state sensible cooling or heating capacity). The curve should be normalized to a value of 1.0 when the part-load ratio equals 1.0. Equation 5 shows the general form of the correlation.

$$PLF = a + bPLR + cPLR^2 \quad (6.5)$$

For a multi-speed heat pump, the above curves are separately defined at corresponding compressor speeds. EnergyPlus is also capable of simulating other HVAC configurations such as water-source heat pumps, chillers, fan-coil units, VAV systems, etc. Complex control strategies can be described in EnergyPlus for any system through the use of schedules, set-points, and plant operation schemes. The software can also size the system components and calculate the design supply air flow rates if desired. EnergyPlus can be configured to calculate the initial and the operating cost of the system

being simulated. It can also calculate the pollutants resulting from on and off-site energy consumptions.

A 5000 ft^2, 3-zone, one-story, office building was modeled. Figure 6.1 shows a layout of the building. The ceiling is 8 ft high, and the roof is 10 ft high. The space between the ceiling and the roof is unconditioned. All the exterior walls are composed of three layers: ¾" plaster, 4" common brick, and 1" stucco on the outside. Partitions between different zones are composed of 8" clay tile sandwiched between two ¾" plaster layers. The floor slab is 8" HW concrete. The ceiling is ¾" acoustic tile. The roof is composed of ½" slag, ⅜" felt and membrane, 1" dense insulation, and 2" HW concrete on the outside. The building has a 108 ft^2 window on the south wall.

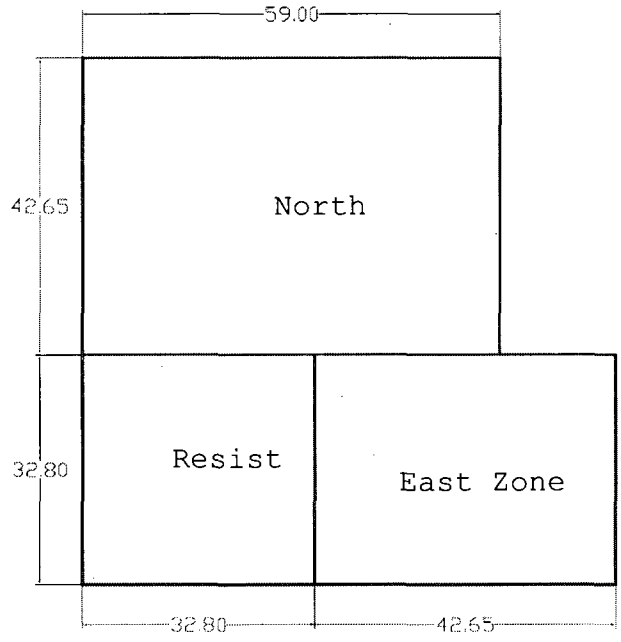

Figure 6.1 Building Layout (Dimensions in ft.)

The building has a peak occupancy of ten people. The level of occupancy changes according to the day of the week and the time of the day with zero occupancy on the

weekends and from 6:00 PM to 8:00 AM on any week day. The peak lighting load is 7985 Btu/hr (2.34 kW.) The level of lighting also varies throughout the day. On weekends, the lighting load is zero throughout the day. The electric equipment load is 24976.9 Btu/hr (7.32 kW.) This load is constant from 8:00 AM to 6:00 PM on Monday through Friday, and zero on Saturday and Sunday.

During occupancy hours, fresh air is admitted into the building at a rate of 500 SCFM. Design supply air flow rates to the different zones are summarized in Table 6.1. The east zone is the controlling zone with dual temperature set-points as summarized in Table 6.2.

Table 6.1 Supply Air Flow Rate to Each Zone.

	Resistive Zone	**East Zone**	**North Zone**
Air flow rate, ft^3/min	1000	1500	2000

Table 6.2 Dual Temperature Set-points.

Mode of operation	
Monday through Friday from 7:00 AM to 5:00 PM Any other time (cooling)	75.2°F 86°F
Monday through Friday from 7:00 AM to 5:00 PM Any other time (heating)	68°F 59°F

The GHP operates at three different speeds; 1650, 2000, and 2400 rpm. Rated capacities of the GHP were obtained from the results of the tests conducted. Table 6.3 and Table 6.4 summarize the coefficients (*a, b, c, d, e,* and *f* in equations 1 through 5) of the different performance curves for the GHP. Capacity and EIR curves as function of the air flow rate are not included since the GHP has a fixed air flow rate at each speed. For

the Chicago simulation, the GHP was assumed to have a 130,000 Btu/hr supplemental gas heating coil with efficiency of 80% to meet the peak heating load requirements.

Table 6.3 Capacity and EIR Curves for Cooling and Heating.

	Capacity Modifier Curve			**EIR Modifier Curve**		
	Cooling					
	Speed 1	Speed 2	Speed 3	Speed 1	Speed 2	Speed 3
a	0.698111	0.936691	0.396841	1.464089	-0.68842	-1.12722
b	-0.03226	-0.02591	0.063464	0.001925	0.173358	0.128932
c	0.003933	0.002081	-0.00029	-0.00173	-0.00455	-0.00304
d	0.021272	0.005125	-0.01068	-0.0315	0.004441	0.071381
e	8.15E-05	-1.84E-5	0.000364	0.000636	0.000524	-0.00057
f	-0.00205	-0.00058	-0.00088	0.000642	-0.00108	-0.00153
	Heating					
a	-0.28549	0.569604	0.31284	0.376399	1.323043	1.386603
b	0.120955	0.028981	0.058177	0.038214	-0.05076	-0.05102
c	-0.00339	-0.00083	-0.00165	-0.00039	0.001588	0.001292
d	0.004883	0.026841	0.008516	0.012214	0.028753	0.018334
e	-0.0003	-0.00012	-0.00027	5.54E-05	0.000145	-1.12E-6
f	0.001321	-2.09E-5	0.000826	-0.00032	-0.00111	-0.00047

Table 6.4. Part Load Fraction Curves.

	Cooling			**Heating**		
	Speed 1	Speed 2	Speed 3	Speed 1	Speed 2	Speed 3
a	0.75881	0.75881	0.75881	0.72458	0.72458	0.72458
b	0.24119	0.24119	0.24119	0.27542	0.27542	0.27542
c	0	0	0	0	0	0

The GHP was compared to two different alternatives; an electrical heat pump and a gas pack unit. The heat pump has DX coils and an electrical supplemental heating coil. It operates at a rated COP of 3.52. The gas pack unit is a straight cooling air conditioner with gas furnace for heating. The gas furnace was assumed to be 80% efficient. The two

units had the same total cooling and heating capacity as the GHP with the same air flow rates to the different zones.

The cost of electricity and gas were gathered form utility companies at the corresponding locations. The simulated tariffs are summarized in Table 6.5.

Table 6.5 Gas and Electricity Cost in Las Vegas and Chicago.

	Las Vegas		**Chicago**	
Electric	Facilities Charge, per kW	$3.54	For the first 80 hours , per kWh	$0.16
	Demand Charge, per kW		For the next 80 hours per kWh	$0.09
	Summer on-peak	$7.23	Additional use, per kWh	$0.04
	Summer mid-peak	$0.53	Demand Charge, per kW	$4.11
	Summer off-peak	$0.00		
	All other periods	$0.25		
	Energy Charge, per kWh			
	Summer on-peak	$0.11		
	Summer mid-peak	$0.09		
	Summer off-peak	$0.06		
	All other periods	$0.07		
Gas	Commodity Charge	$0.94	For the first 100 Therms	$0.35
			For the next 4900 Therms	$0.14
			Additional use, per Therm	$0.07
			Gas charge, per Therm	$0.80

Becoming an increasingly more important factor in designing or selecting any product, environmental impacts of using the GHP were compared to those of the other alternatives. This was done through comparing the CO_2 annual production associated with using each of the three units. National average CO_2 production factor of 1.57 pound per kWh of end-use delivered electricity is used. Similarly, a factor of 117 pounds of CO_2 per each million Btu was used for natural gas (this factor is estimated specifically for using natural gas as a fuel for reciprocating engines) [76].

6.2. Results and Analysis

A total of six simulations were performed; each of the three units was simulated once for each location. TMY3 weather files were used for both locations. Monthly electricity and gas consumed by the HVAC system were reported. In order to compare the total energy consumed by each of the three units, secondary source energy (electricity) was converted to its primary source energy equivalent. The primary source energy equivalent is the amount of energy used at the power plant (in the form of fuel) for each unit of electric energy delivered for the end-use. The conversion factor for the US national grid is estimated at 10,240 Btu/kWh [77].

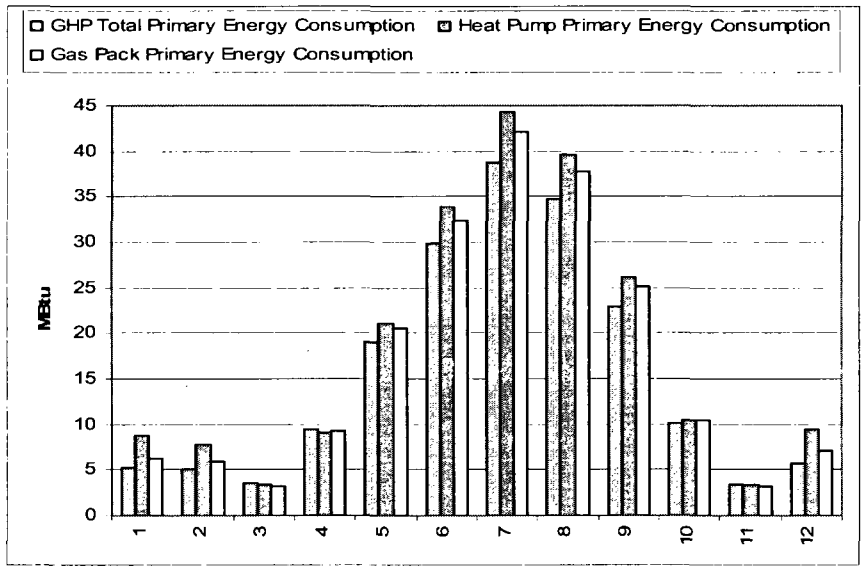

Figure 6.2 Monthly Primary Energy Consumption for Las Vegas Case

This means that 3.125 units of fuel energy are consumed at the power plant for each unit of electric energy delivered for the end-use. Figure 6.2 shows the monthly total primary energy consumption of the GHP, the electric DX Heat Pump, and the Gas Pack

unit for the Las Vegas simulations. The annual total primary energy consumptions of the three units are shown in Figure 6.3. The GHP consumes 187.7 MBtu of primary energy annually, while the electric heat pump consumes 217.2 MBtu and the gas pack unit consumes 202.9 MBtu.

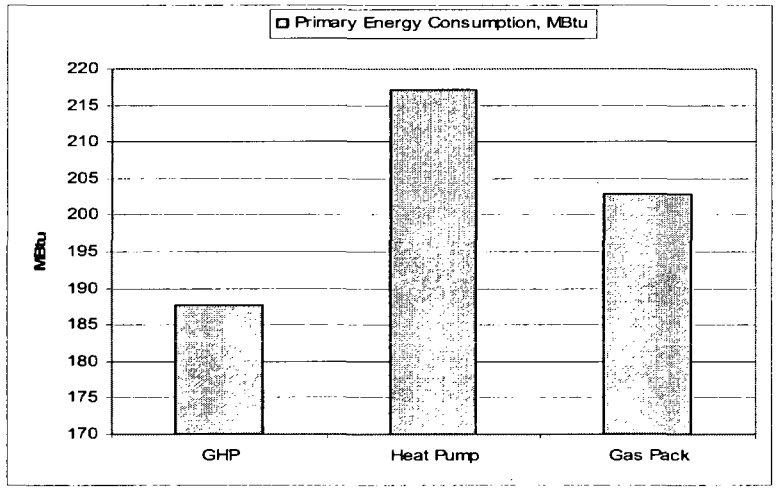

Figure 6.3 Annual Primary Energy Consumption for Las Vegas Case.

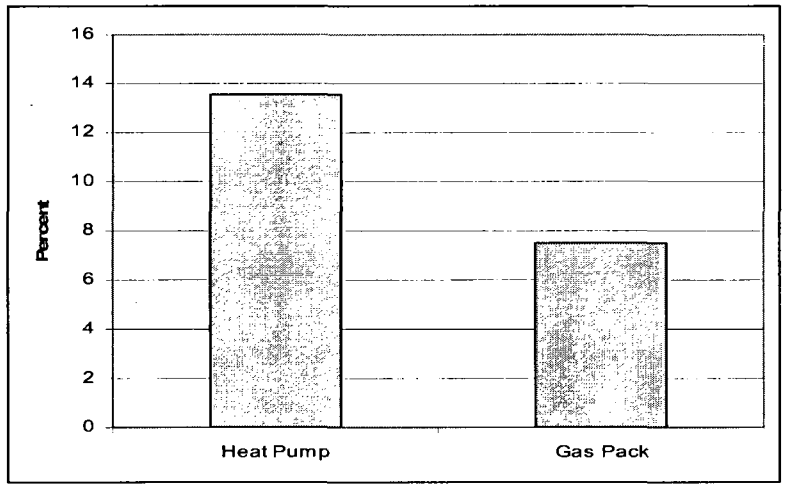

Figure 6.4 Reduction in Primary Energy for Las Vegas Case.

Thus, using the GHP instead of any of the other two units' results in reduced primary energy consumption. This reduction was calculated as in equation (6.6) and shown in Figure 6.4. The GHP consumes 13.6% less primary energy than the electric heat pump and 10.6% less than the gas pack unit. CO_2 production associated with using each of the three different units is shown in Figure 6.5. The GHP produces 22679 pounds of CO_2. This is 29% less than what the electric heat pump produces (31979 pounds), and 26% less than the gas pack unit (30660 pounds.).

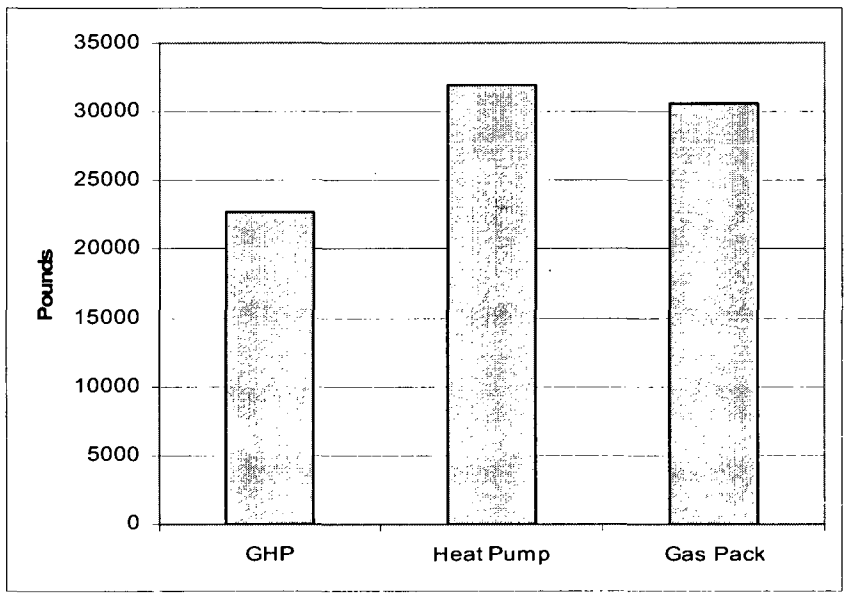

Figure 6.5 CO_2 Emission for the Las Vegas Case.

Figure 6.6 shows the monthly energy cost for each unit for the Las Vegas simulation. The GHP was remarkably less expensive (costs about only 30% of what any of the other two unit costs) during the cooling season. During the heating season, it also costs less than the electric heat pump and almost the same as the gas pack unit. Annually, the GHP

costs $1824, which is 67% and 63% less expensive than the electric heat pump (which costs $5487) and the gas pack unit (which cost $4979) respectively.

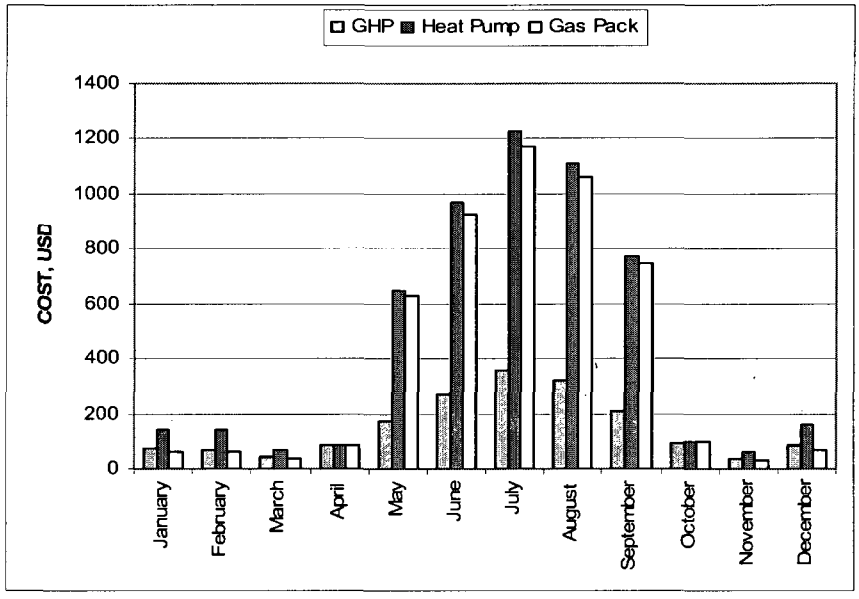

Figure 6.6 Monthly Energy Cost for the Las Vegas Simulation.

The same analysis was performed for the Chicago simulations. Figure 6.7 shows the total monthly primary energy consumption for the three units. The energy consumption profile of the GHP as shown in this figure indicates that the GHP has more energy consumption reduction potential during heating seasons. Figure 6.8 shows the total annual primary energy consumption of the three units.

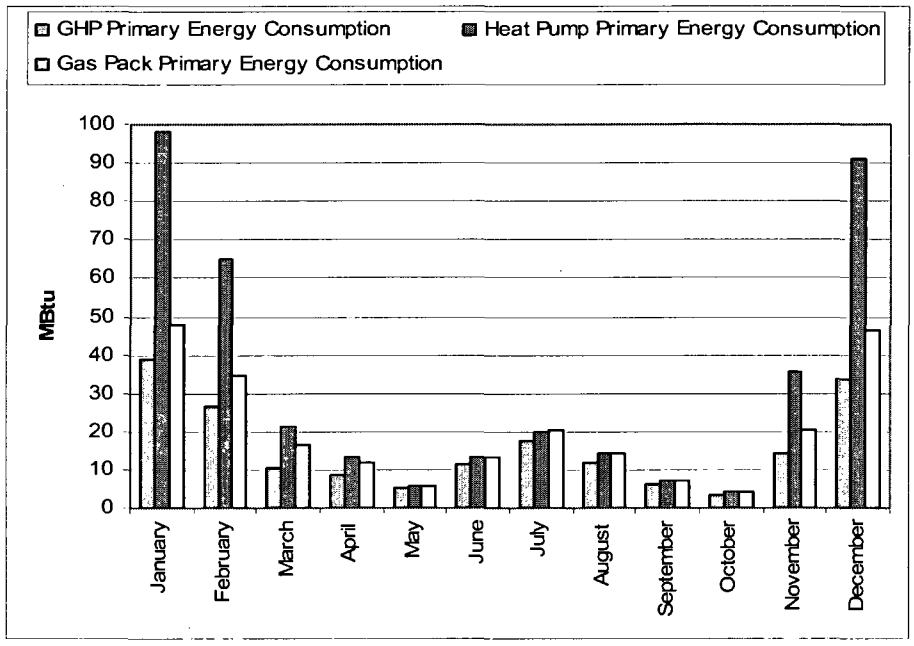

Figure 6.7 Monthly Primary Energy Consumption for Chicago Case

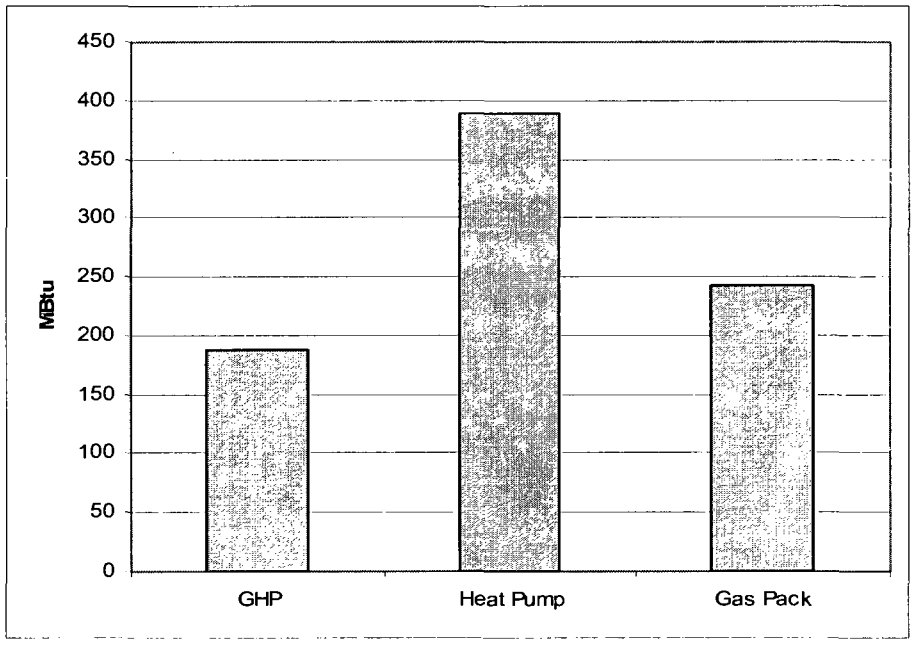

Figure 6.8 Annual Primary Energy Consumption for Chicago Case

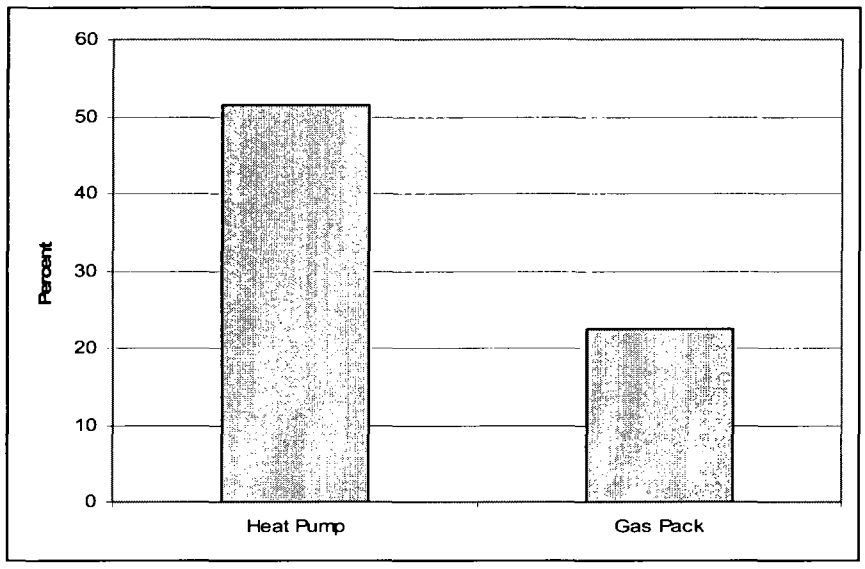

Figure 6.9. Reduction in Primary Energy Consumption for Chicago

Figure 6.10 shows the annual CO_2 production for each unit. The GHP produces 22938 pounds of CO_2 which is 60% less than what the electric heat pump results in (57172 pounds of CO_2) and 69% less than the gas pack unit (73663 pounds.)

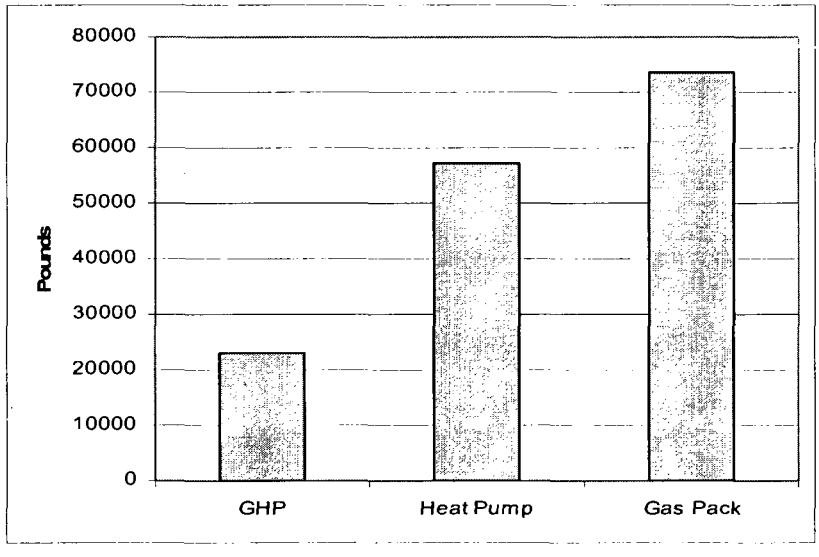

Figure 6.10. CO_2 Emission for the Chicago Case

Figure 6.11 shows the monthly energy cost for the three different units for the Chicago simulation. Annually, the GHP costs $2005. This is 65% less expensive than the electric heat pump (which costs $5678), and 31% less expensive than the gas pack unit (which costs $2917.)

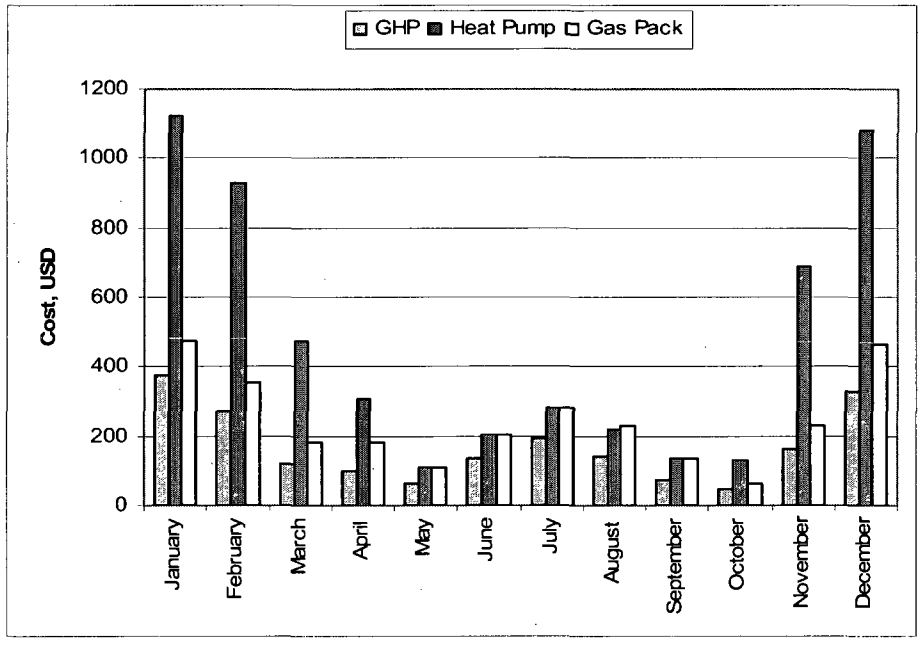

Figure 6.11. Monthly Energy Cost for Chicago Case.

6.3. Conclusions

For both climate conditions, GHP consumed less primary energy (10.6% for the Las Vegas simulation and 22.6% for the Chicago simulation less than its nearest alternative), and accordingly produced less CO_2 emissions (26% for the Las Vegas simulation, and 59.9% for the Chicago simulation less than its nearest alternative). Primary energy consumptions and CO_2 productions are summarized in Table 6.6 and Table 6.7 respectively.

Table 6.6 Primary Energy Consumption Summary

	GHP	DX Heat Pump	% Reduction	Gas Pack	% Reduction
Las Vegas	187.7	217.2	13.6	209.2	10.6
Chicago	188.0	388.0	51.5	243	22.6

Table 6.7 CO_2 Production for Both Locations.

	GHP	DX Heat Pump	% Reduction	Gas Pack	% Reduction
Las Vegas	22679	31979	29.0	30660	26.0
Chicago	22938	57172	59.9	73663	68.9

In terms of energy cost, the GHP costs less than its conventional counterparts in both climatic extremes with more saving potential in the colder climate (63% for Las Vegas simulation and 31% for Chicago simulation less than its nearest alternative.) Table 6.8 summarizes the energy cost of the different alternatives for both locations.

Table 6.8 Cost (in USD) Summary.

	GHP	DX Heat Pump	% saving	Gas Pack	% saving
Las Vegas	1825	5487	67	4979	63
Chicago	2005	5678	65	2916	31

The equipment cost of the GHP is 75 to 85% higher than conventional 10 refrigeration ton unit. However, reduction in electrical infrastructure size (transformer, electrical panel, disconnects, and wiring) will significantly reduce the upfront initial cost to the customer. Currently, the product is in the monitoring and trail sales phase and mature unit pricing is not available. The goal is to have a payback period to the customer in less than 5 years.

Although the GHP resulted in more primary energy consumption in Chicago, it resulted in more savings in Las Vegas. This is due to the high electricity rates during the summer in Las Vegas. Using natural gas, the GHP avoided the need for paying on-peak demand and energy charges. Besides, natural gas pricing doesn't incorporate demand or on-peak charges like electricity rates do. This is one of the most prominent economical merits of using the GHP. It should be noted also that for higher air conditioning tonnage applications the savings will be more since the electric power demand will rise accordingly.

CHAPTER 7

CONCLUSIONS AND RECOMMENDATIONS

7.1. Conclusions

The detailed numerical and experimental study has been made for a GHP system by using suction-liquid line heat exchangers in cooling operation and suction line waste heat recovery to augment heating capacity. To improve the system performance, a new refrigerant 410A has been used as the working fluid. Both 3D computational fluid dynamics modeling on the heat exchanger and integrated system modeling were established. The improved performance has been obtained comparing with the traditional electrical DX heat pump. The major conclusions for this dissertation are obtained as follows.

According to the CFD analysis on the design of the heat exchanger for seven working cases during the heating and cooling operation, that although the effectiveness of the shell tube exchanger is small due to the small thermal conductivity of vapor refrigerant R410A, the goal of this numerical study still has been reached and over 30,000 btu/hr heat exchange has been obtained for the current heat exchanger configuration. The output from the CFD analysis, total heat transferred and pressure drop, are used as an input to the overall GHP modeling.

With using the system modeling software MODCON developed in ORNL, the steady-state heating and cooling performance of the GHP system has been obtained.

Three different GHP cycles with/without suction liquid heat exchange and heat recovery were evaluated. The results show that an improved system performance has been obtained by using suction liquid line heat exchanger and heat recovery. The waste heat of the gas engine can take about 20-25% of the total heating capacity in rated operating condition. The performance of GHP system is affected by the ambient temperature while the engineer efficiency in the constant engine speed almost keep the same under different ambient temperature.

Experiments on the system performance of GHP have been taken place in a psychrometric test facility at Oak Ridge National Heat pump Laboratory. The comparison between experimental results and system simulation over a range of speeds and ambient indicated has been made. The trends in COP and capacity were generally well predicted and a good agreement has been obtained.

The energy consumption and CO_2 emissions for a 5000 ft^2 office building at different locations have been evaluated by using the Energy Plus for both the GHP and its most common counterparts: an electrical DX heat pump. The results shows that there is a great energy saving can be obtained comparing with the electrical DX heat pump while the CO_2 emissions has been reduced greatly. For the simulation at Las Vegas, a 10.6% primary energy saving was obtained while the CO_2 emissions have been reduced by about 26%. For the simulation for Chicago, a 22.6% primary energy saving were obtained while the CO_2 emissions have been reduced about 59.9%.

7.2. Recommendations for Future Research

In this study, it's been shown a significant savings in primary energy by utilizing GHP. However, there are several areas where further investigation required in improving the overall performance of the unit. Some of the areas needing further study include: enhanced heat exchangers for indoor and outdoor coils, more efficient refrigerant vapor compression for high pressure ratios, and work recovery devices that reduce the expansion process irreversibility characteristic of throttling valves.

Vortex tubes and vapor injection compressors work well in heat pump installations due to relatively high pressure ratio during system operation but their development is in the early stage phase. Because heat pumps usually operate at elevated pressure ratios in comparison to the conventional air-conditioning installations, opportunities for energy efficiency improvement have been evolved from multi-stage compression techniques traditionally adopted in refrigeration applications, such as injection compressors and economizers. Novel injection techniques reduce the throttling and pumping losses of conventional vapor injection port design and potentially improve the energy performance. Economizer cycles are also well-justified for high compression ratios and they benefit the system at very high and low ambient temperatures, provide superior dehumidification, and promote flexibility in multi-circuit system configuration. More work on those areas is needed.

The conventional throttling valve is an inexpensive but inefficient device of the basic vapor compression cycle. Control of the heat pump systems is mainly performed by a thermal expansion electronic valve (TEV), which plays a primary role during the dynamic frosting and defrosting periods. Recent work in the engineering community

focuses on replacing the throttling valve with expanders, ejectors, vortex tubes, and other work recovery devices that augment the energy efficiency performance with respect to the basic heat pump system. Expanders, which are usually mechanically coupled and integrated within the compressor shell, recover the expansion work of the gas that flows from high pressure condensers to low pressure evaporators. The benefits of the expanders (screw, scroll, rotary, swing piston, and reciprocating type) depend on their overall efficiency.

The interactive nature of the mixture and throttle controls with overall performance required a large number of tests to be conducted.. The currently investigated system has an open loop controller. A closed loop control system by adding of an oxygen sensor on the engine exhaust that could be used by the controller to adjust the air/fuel mixture to achieve the desire oxygen content in the flue will give better management of the system.

According to a proposed U.S. EPA standard, before a natural gas engine driven heat pump can be used in the United States, its emission performance must be determined. The total brake specific concentrations of key regulated emissions, such as oxides of nitrogen (NOx), carbon monoxide (CO), and the total hydrocarbons (THC) must be determined over the appropriate test cycle (as specified by the U.S. EPA). In addition it is also important to assess the emitted levels of unregulated species, such as formaldehyde, which may also be subject to mandatory emission standards.

APPENDIX I

PROGRAM INPUT PARAMETERS

```
***  PARAMETRIC DATA GENERATOR FRONT-END IS BYPASSED  ***
***** INPUT DATA *****

     SUMMARY OUTPUT
     ATMOSPHERIC PRESSURE IS 14.696 PSIA
     COOLING MODE OF OPERATION
     THE SYSTEM REFRIGERANT IS R-410A
                    R-32/R-125(50/50)
     REFRIGERANT CHARGE IS NOT SPECIFIED
     COMPRESSOR INLET SUPERHEAT IS SPECIFIED AT   10.00 F
     CONDENSER  EXIT SUBCOOLING IS SPECIFIED AT   15.00 F
     ESTIMATE OF:
      SATURATION TEMPERATURE INTO   COMPRESSOR   45.00 F
      SATURATION TEMPERATURE OUT OF COMPRESSOR  125.00 F
     COMPRESSOR CHARACTERISTICS:
     GEDAC-410A OPEN COMPRESSOR, 4080 rpm
     **SELECTED COMPRESSOR:
      SELECTED OPERATING FREQUENCY RATIO       1.000
      DRIVE TYPE OF INPUT COMPRESSOR DATA IS    1-SPEED TYPICAL
      SELECTED COMPRESSOR EER                 11.70 BTU/W-H
      SELECTED COMPRESSOR CAPACITY          113400. BTUH
      EER SCALING FACTOR FROM BASE COMPRESSOR   1.000
      CAP SCALING FACTOR FROM BASE COMPRESSOR   1.890
      SELECTED COMPRESSOR DISPLACEMENT        5.991 CU IN
      SELECTED MOTOR SIZE IS                  9.45 HP
      NOMINAL FREQUENCY FOR     MOTOR RATING AT  60.0 HZ
      NOMINAL VOLTAGE  FOR      MOTOR RATING AT 220.0 VOLTS
      SELECTED OPERATING VOLTS/HERTZ MULTIPLIER   1.0
     **BASE COMPRESSOR:

      BASE EER        FOR COMPRESSOR MAP      11.70 BTU/W-H
      BASE CAPACITY    FOR COMPRESSOR MAP     60000. BTUH
      BASE DISPLACEMENT FOR COMPRESSOR MAP      3.170 CU IN
      BASE MOTOR SIZE IS                   5.00 HP
      NOMINAL FREQUENCY FOR BASE MOTOR RATING AT  60.0 HZ
      NOMINAL VOLTAGE  FOR BASE MOTOR RATING AT 220.0 VOLTS
      BASE SUPERHEAT   FOR COMPRESSOR MAP     18.000 F
      BASE REFRIGERANT  FOR COMPRESSOR MAP     R-410A
                          R-32/R-125(50/50)

***** INPUT DATA *****
      ** USER PROVIDED ARI 10-TERM COEFS FOR COMPR POWER AND MASS FLOW AT DISCRETE FREQS **
      MAP REPRESENTATIONS AT  1 DISCRETE FREQUENCY(S)
      MAP COEFFICIENTS AT  60.0 HZ FREQUENCY   NOMINAL SPEED OF  4080.0 RPM   DRIVE VOLTAGE OF  230.0
VOLTS
      MAP INDEPENDENT PARAMETER IS SATURATION TEMP (F)
      POER DRAW=
        7.651E+02 WATTS + -1.272E+01*INLETparam
       + -6.354E+00*OUTLETparam +  4.276E-01*INLETparam**2
       +  1.696E-01*OUTLETparam*INLETparam +  4.338E-01*OUTLETparam**2
       + -3.715E-03*INLETparam**3 + -3.287E-03*OUTLETparam*INLETparam**2
       + -2.817E-05*INLETparam*OUTLETparam**2 + -8.544E-04*OUTLETparam**3
      MASS FLOW RATE=
```

```
      6.194E+02 LBM/HR + 4.140E+00*INLETparam
     + -6.071E+00*OUTLETparam + 1.027E-01*INLETparam**2
     + 7.959E-02*OUTLETparam*INLETparam + 6.218E-02*OUTLETparam**2
     + -3.905E-04*INLETparam**3 + -2.208E-05*OUTLETparam*INLETparam**2
     + -3.477E-04*INLETparam*OUTLETparam**2 + -2.052E-04*OUTLETparam**3
     GENERAL SHELL HEAT LOSS CORRELATION IS SELECTED:
      CANFAC =  -1.70400E-02*CONDENSING TEMPERATURE + 5.61000E-05*CONDENSING TEMPERATURE**2 +
1.31400E+00
     SUPERHEAT CORRECTION TERMS (SET IN BLOCK DATA):
      POWER CORRECTION ADJUSTMENT MULTIPLIER  0.000
      VOLUMETRIC EFFICIENCY CORRECTION FACTOR 0.750
      SUCTION GAS HEATING FACTOR          0.330
      SUCTION SUPERHEAT HEAT TRANSFER FACTOR  0.050
      SUCTION GAS HEAT PICKUP FRACTION      0.750
***** INPUT DATA *****
   INDOOR UNIT:
     INLET AIR TEMPERATURE   80.000 F      WET BULB TEMPERATURE     67.000 F
     FAN OPERATING FREQUENCY            60.00 HZ
     FAN NOMINAL  FREQUENCY   60.00 HZ  NOMINAL AIRFLOW RATE  4000.00 SCFM
     FAN NOMINAL  SPEED  1080.00 RPM     NUMBER OF MOTOR POLES        6
     NOMINAL  FAN POWER   1460.00 WATTS  REFERENCE TEMP         -999.00 F
     SPECIFIED EXTERNAL (DUCT) PRESSURE DROP   0.15 IN H20
     APPLICATION CAPACITY OF FILTER/HEATER    10.00 TONS     HEATER FLOW AREA                 5.12 SQ FT
     FILTER FLOW AREA     11.12 SQ FT   NUMBER OF HEATER BANKS              3.
     FRONTAL AREA OF HX              15.280 SQ FT
     CORRUGATED FINS              FIN PATTERNS PER TUBE ROW SPACING        2
     FIN PATTERN DEPTH (PEAK TO VALLEY)     0.0520 IN      FIN PATTERN ANGLE              18.41 DEG
     NUMBER OF TUBES IN DIRECTION OF AIR FLOW  4.00        FIN PITCH                   18.00 FINS/IN
     NUMBER OF PARALLEL CIRCUITS          20.00        FIN THICKNESS              0.00450 IN
     OD OF TUBES IN HX              0.31250 IN      THERMAL CONDUCTIVITY: FINS        128.30 BTU/H-FT-F
     ID OF TUBES IN HX             0.28850 IN      THERMAL CONDUCTIVITY: TUBES       225.00 BTU/H-FT-F
     HORIZONTAL TUBE SPACING         0.625 IN      FRACTION OF COMPUTED CONTACT CONDUCTANCE 100.000
     VERTICAL TUBE SPACING            1.000 IN      NUMBER OF RETURN BENDS            140.00
     NUMBER OF PARALLEL CIRCUITS- SUBCOOL REGION20.00        CROSS COUNTERFLOW FOR N ROWS
     REF-SIDE TUBE SURFACE           RIFLED-A       AIR-SIDE HEAT-TRANSFER MULTIPLIER      1.000
     REF-SIDE HEAT-TRANSFER MULTIPLIER      1.000      AIR-SIDE AREA MULTIPLIER          1.000
     REF-SIDE AREA MULTIPLIER          1.000      AIR-SIDE PRESSURE-DROP MULTIPLIER - UNIT  1.000
     REF-SIDE PRESSURE-DROP MULTIPLIER      1.000      AIR-SIDE PRESSURE-DROP MULTIPLIER - SYSTEM 1.000
     RIFLED-TUBE GEOMETRY:
     NUMBER OF FINS IN TUBE            50.0       RIFLED TUBE HELIX ANGLE           18.0 DEG
     RIFLED TUBE FIN HEIGHT       8.00 MILS    RIFLED TUBE FIN ANGLE  50.0 DEG
   OUTDOOR UNIT:
     INLET AIR TEMPERATURE  95.000 F      WET BULB TEMPERATURE   75.000 F
     FAN OPERATING FREQUENCY            60.00 HZ
     FAN NOMINAL  FREQUENCY            60.00 HZ      NOMINAL AIRFLOW RATE          8000.00 SCFM
     FAN NOMINAL  SPEED              1080.00 RPM     NUMBER OF MOTOR POLES           6
     NOMINAL  FAN POWER              600.00 WATTS    REFERENCE TEMPERATURE          -999.00 F
     FRONTAL AREA OF HX              27.500 SQ FT
     SLIT/LANCED FINS                    WIDTH OF SINGLE STRIP IN FLOW DIRECTION  0.0780 IN
     NUMBER OF STRIPS PER ENHANCED ZONE       7       HEIGHT (OFFSET) OF SINGLE STRIP      0.0575 IN
     NUMBER OF TUBES IN DIRECTION OF AIR FLOW  2.00        FIN PITCH                   20.00 FINS/IN
     NUMBER OF PARALLEL CIRCUITS          9.00        FIN THICKNESS              0.00450 IN
     OD OF TUBES IN HX              0.31250 IN      THERMAL CONDUCTIVITY: FINS        128.30 BTU/H-FT-F
     ID OF TUBES IN HX             0.28850 IN      THERMAL CONDUCTIVITY: TUBES       225.00 BTU/H-FT-F
     HORIZONTAL TUBE SPACING         0.625 IN      FRACTION OF COMPUTED CONTACT CONDUCTANCE 100.000
     VERTICAL TUBE SPACING            1.000 IN      NUMBER OF RETURN BENDS            63.00
     NUMBER OF PARALLEL CIRCUITS- SUBCOOL REGION 9.00        CROSS COUNTERFLOW FOR N ROWS
     REF-SIDE TUBE SURFACE           RIFLED-A       AIR-SIDE HEAT-TRANSFER MULTIPLIER      1.000
     REF-SIDE HEAT-TRANSFER MULTIPLIER      1.000      AIR-SIDE AREA MULTIPLIER          1.000
     REF-SIDE AREA MULTIPLIER          1.000      AIR-SIDE PRESSURE-DROP MULTIPLIER - UNIT  1.000
     REF-SIDE PRESSURE-DROP MULTIPLIER     1.000      AIR-SIDE PRESSURE-DROP MULTIPLIER - SYSTEM 1.000

     RIFLED-TUBE GEOMETRY:
     NUMBER OF FINS IN TUBE            50.0       RIFLED TUBE HELIX ANGLE           18.0 DEG
     RIFLED TUBE FIN HEIGHT           8.00 MILS     RIFLED TUBE FIN ANGLE           50.0 DEG
   COMPRESSOR CAN HEAT LOSS ADDED TO AIR AFTER  CROSSING THE OD COIL.
    POWER TO THE INDOOR  FAN ADDED TO AIR AFTER  CROSSING THE INDOOR  COIL.
     POWER TO THE OUTDOOR FAN ADDED TO AIR AFTER  CROSSING THE OUTDOOR COIL.
***** INPUT DATA *****
    LINE HEAT TRANSFER:
```

```
    HEAT GAIN IN SUCTION LINE              0.0 BTU/H
    HEAT LOSS IN DISCHARGE LINE            0.0 BTU/H
    HEAT LOSS IN LIQUID LINE               0.0 BTU/H
   LINE AUXILIARY PRESSURE DROPS:
    @NOMINAL REFRIGERANT FLOW RATE OF      0.0 LBM/H
    SUCTION LINE                  0.0 PSI
    DISCHARGE LINE                0.0 PSI
    LIQUID LINE                   0.0 PSI
   DESCRIPTION OF CONNECTING TUBING:
    LIQUID LINE FROM INDOOR TO OUTDOOR HEAT EXCHANGER
      ID            0.43600 IN
      EQUIVALENT LENGTH     10.00 FT
    FROM INDOOR COIL TO REVERSING VALVE       FROM OUTDOOR COIL TO REVERSING VALVE
      ID            1.02500 IN          ID            1.02500 IN
      EQUIVALENT LENGTH     10.00 FT          EQUIVALENT LENGTH     4.00 FT
    FROM REVERSING VALVE TO COMPRESSOR INLET    FROM REVERSING VALVE TO COMPRESSOR OUTLET
      ID            1.02500 IN          ID            0.78500 IN
      EQUIVALENT LENGTH     4.00 FT          EQUIVALENT LENGTH     4.00 FT
   COMPRESSOR AND ACCUMULATOR GEOMETRY DATA:
    VOLCMP =  395.00 CU IN
    ACCHGT =  30.00 IN  ACCDIA =  6.00 IN  ATBDIA =  0.6800 IN
    OILDIA =  0.035 IN  UPPDIA =  0.040 IN  HOLDIS =  2.50 IN
   ITERATION TOLERANCES :
    AMBCON  0.100 F   CMPCON  0.050 BTU/LBM   TOLH  0.00100 BTU/LBM
    CNDCON  0.200 F   FLOCON  0.200 LBM/HR    TOLS  0.00005 BTU/LBM-R
    EVPCON  0.500 F   CONMST  0.003 F
   HEAT TRANSFER CORRELATIONS:
    EVAPORATING CORRELATION: THOME,et al, 2002
    CONDENSING CORRELATION: THOME/CAVALLINI,et al, 2004
    AIR-SIDE CORRELATIONS: WANG, 1999-2000
***** COMPUTED HEAT EXCHANGER CHARACTERISTICS *****
                          CONDENSER   EVAPORATOR
   AIR FLOW AREA / FRONTAL AREA          0.61744     0.62354
   INSIDE  PERIMETER OF TUBE (FT)        0.11800     0.11800
   OUTSIDE PERIMETER OF TUBE (FT)        0.08417     0.08417
   OUTSIDE CROSS-SECTIONAL AREA OF TUBE (FT2) 0.00056     0.00056
   CROSS-SECTIONAL FLOW AREA OF TUBE (FT2)  0.00044     0.00044
   CONTACT CONDUCTANCE (BTU/H-FT2-F)      151674.7     130813.5
   LENGTH OF HX TUBING PER CIRCUIT (FT)      73.333      36.672
   REFRIGERANT SIDE HEAT TRANSFER AREA
         PER CIRCUIT (FT2)           8.653       4.327
   TOTAL REFRIGERANT SIDE HEAT TRANSFER AREA
         ALL CIRCUITS (FT2)          77.881      86.547
   REFRIGERANT SIDE HEAT TRANSFER AREA
         / HEAT EXCHANGER VOLUME (1/FT)  27.188      27.188
   TOTAL AIR-SIDE HEAT TRANSFER AREA (FT2)   1246.95     1317.83
   FIN HEAT TRANSFER AREA
      / TOTAL AIR-SIDE HEAT TRANSFER AREA  0.959       0.957
   FIN AREA ENHANCEMENT FACTOR              1.000       1.054
   AIR-SIDE AREA ENHANCEMENT FACTOR         1.000       1.051
   AIR SIDE HEAT TRANSFER AREA
         / HEAT EXCHANGER VOLUME (1/FT)  435.300     413.979
   AIR-TO-REFRIGERANT HEAT TRANSFER AREA RATIO  16.011      15.227


*** FAN/BLOWER PERFORMANCE          CONDENSER       EVAPORATOR
   INPUT POWER                 600.0 WATTS      1460.0 WATTS
   AIR MASS FLOW RATE (DRY)   35441.4 LBM/H     17811.4 LBM/H
   AIR VOL. FLOW, STANDARD     8000.0 SCFM      4000.0 SCFM
   AIR VOL. FLOW AT FAN  INLET  8876.3 ACFM      3951.6 ACFM
   AIR VOL. FLOW AT COIL INLET  8569.3 ACFM      4148.5 ACFM
   FACE   VEL. AT COIL INLET   311.6 FT/MIN      271.5 FT/MIN
   SURFACE  VEL. AT COIL INLET   504.7 FT/MIN      435.4 FT/MIN
   UNIT  PRESSURE DROP        0.111 IN H20     0.289 IN H20
   DUCT  PRESSURE DROP                  0.150 IN H20
   FILTER PRESSURE DROP                 0.088 IN H20
   HEATER PRESSURE DROP                 0.127 IN H20
   TOTAL  PRESSURE DROP       0.111 IN H20     0.654 IN H20
   MOTOR SPEED             1080.00 RPM      1080.00 RPM
   % OF NOMINAL FREQUENCY      100.00 %         100.00 %
```

```
    DRIVE EFFICIENCY
     AT OPERATING SPEED        1.000          1.000
    COMBINED DRIVE & FAN
     EFFICIENCY          0.17398        0.21062
***** CALCULATED HEAT PUMP PERFORMANCE *****
*** CONDENSER -- HEAT TRANSFER PERFORMANCE OF EACH CIRCUIT
    INLET AIR TEMPERATURE          95.000 F
    AIR TEMPERATURE  LEAVING COIL   114.871 F
     HEAT LOSS FROM COMPRESSOR     2388.2 BTU/H
     HEAT GENERATED FROM FAN       2047.2 BTU/H
    OUTLET AIR TEMPERATURE         115.378 F
    TOTAL HEAT EXCHANGER EFFECTIVENESS 0.6995

                        SUPERHEATED      TWO-PHASE      SUBCOOLED
                          REGION          REGION         REGION
    NTU                   1.8404          1.1809         1.4562
    HEAT EXCHANGER EFFECTIVENESS   0.7501          0.6930         0.6608
    CR/CA                 0.3234          *******        0.4316
    FRACTION OF HEAT EXCHANGER     0.1324          0.7399         0.1277
    FRACTION OF AIR FLOW RATE      0.2647          1.0000         0.2554
    HEAT TRANSFER RATE          3336.3 BTU/H    14451.7 BTU/H    1535.0 BTU/H
    INLET  AIR TEMPERATURE       111.421 F       96.578 F       95.000 F
    OUTLET AIR TEMPERATURE       124.400 F       111.440 F      101.180 F
    INLET  REFRIGERANT TEMPERATURE  164.756 F       119.377 F      116.669 F
    AVE.  REFRIGERANT TEMPERATURE                118.023 F
    OUTLET REFRIGERANT TEMPERATURE  124.682 F       116.669 F      102.351 F


    AIR SIDE:                          REFRIGERANT SIDE:
     MASS FLOW RATE        3937.9 LBM/H      MASS FLOW RATE          225.5 LBM/H
     PRESSURE DROP          0.1110 IN H2O     PRESSURE DROP          17.649 PSI
      AUGMENTATION FACTOR 1.511  TWO-PHASE MASS FLUX     508.4 KLBM/H/SQ-FT
     REYNOLDS NUMBER 1197.3     SUBCOOLED MASS FLUX      508.4 KLBM/H/SQ-FT
                                    HEAT TRANSFER COEFFICIENT
     HEAT TRANSFER                   VAPOR REGION          334.857 BTU/H-SQ-FT-F
      COEFFICIENT18.764 BTU/H-SQ-FT-F  TWO PHASE REGION 991.678 BTU/H-SQ-FT-F
      AUGMENTATION FACTOR 1.472     SUBCOOLED REGION  386.135 BTU/H-SQ-FT-F
      FIN PATTERN ANGLE       0.00 DEG        BULK TEMP.WITH WET WALL  124.68 F
     FIN EFFICIENCY (SURFACE)  0.744          DESUPERHEATED FRACTION   0.846

    CONTACT INTERFACE:
     CONTACT CONDUCTANCE    151674.719 BTU/H-SQ-FT-F
    UA VALUES PER CIRCUIT:
     VAPOR REGION (BTU/H-F)       TWO PHASE REGION (BTU/H-F)     SUBCOOLED REGION (BTU/H-F)
      REFRIGERANT SIDE   383.553    REFRIGERANT SIDE   6349.645    REFRIGERANT SIDE   426.728
      AIR SIDE          255.883    AIR SIDE          1430.388    AIR SIDE          246.880
      CONTACT INTERFACE  88000.047    CONTACT INTERFACE 491921.000    CONTACT INTERFACE  84903.961
      COMBINED          153.219    COMBINED          1164.642    COMBINED          156.110
*** FLOW CONTROL DEVICE -- CONDENSER EXIT SUBCOOLING IS  15.000 F
     PERMANENT BLEED FACTOR     1.150
     TXV CAPACITY RATING:       8.765 TONS
      WITH NOZZLE AND TUBES
       NOZZLE SIZE IS          10 TONS
       DISTRIBUTOR TUBES ARE    1/4 IN OD
       DISTRIBUTOR LENGTH IS  30.000 IN

***** CALCULATED HEAT PUMP PERFORMANCE *****
*** EVAPORATOR -- HEAT TRANSFER PERFORMANCE OF EACH CIRCUIT
    INLET AIR TEMPERATURE          79.921 F
    AIR TEMPERATURE  LEAVING COIL    56.066 F
     HEAT GENERATED FROM FAN       4981.5 BTU/H
    OUTLET AIR TEMPERATURE         57.205 F
    MOISTURE REMOVAL OCCURS
    SUMMARY OF DEHUMIDIFICATION PERFORMANCE (TWO-PHASE REGION)
                LEADING EDGE       POINT WHERE MOISTURE
                 OF COIL          REMOVAL BEGINS          LEAVING EDGE OF COIL
                   AIR          AIR          WALL          AIR          WALL
    DRY BULB TEMPERATURE  79.921 F     79.921 F     57.613 F     55.718 F     52.182 F
    HUMIDITY RATIO      0.01122      0.01122      0.01012      0.00890      0.00828
    ENTHALPY  31.531 BTU/LBM  31.531 BTU/LBM  24.849 BTU/LBM  23.066 BTU/LBM   21.522 BTU/LBM
```

```
      RATE OF MOISTURE REMOVAL                    1.9237 LBM/H
      FRACTION OF EVAPORATOR THAT IS WET          1.0000
      LATENT HEAT TRANSFER RATE IN TWO-PHASE REGION      2050. BTU/H
      SENSIBLE HEAT TRANSFER RATE IN TWO-PHASE REGION    4926. BTU/H
      SENSIBLE TO TOTAL HEAT TRANSFER RATIO FOR TWO-PHASE REGION  0.7062
      OVERALL SENSIBLE TO TOTAL HEAT TRANSFER RATIO      0.7178
      OVERALL CONDITIONS ACROSS COIL
                    ENTERING    EXITING
                      AIR         AIR
      DRY BULB TEMPERATURE   79.921 F    56.066 F
      WET BULB TEMPERATURE   66.934 F    55.198 F
      RELATIVE HUMIDITY      0.515       0.949
      HUMIDITY RATIO         0.01122     0.00906
      TOTAL HEAT EXCHANGER EFFECTIVENESS (SENSIBLE)  0.8473
                        SUPERHEATED     TWO-PHASE
                          REGION         REGION
      NTU                 1.2054         2.0100
      HEAT EXCHANGER EFFECTIVENESS   0.6185       0.8660
      CR/CA               1.9421       *******
      FRACTION OF HEAT EXCHANGER     0.0688       0.9312
      HEAT TRANSFER RATE          288.0 BTU/H    6975.6 BTU/H
      AIR MASS FLOW RATE          61.29 LBM/H    829.28 LBM/H
      INLET  AIR TEMPERATURE      79.921 F       79.921 F
      OUTLET AIR TEMPERATURE      60.774 F       55.718 F
      INLET  REF TEMPERATURE      48.963 F       52.161 F
      AVER.  REF TEMPERATURE                50.562 F
      OUTLET REF TEMPERATURE      58.822 F       48.963 F
      AIR SIDE:                              REFRIGERANT SIDE:
       MASS FLOW RATE      890.6 LBM/H       MASS FLOW RATE        101.5 LBM/H
       PRESSURE DROP       0.654 IN H2O      PRESSURE DROP         9.335 PSI
        AUGMENTATION FACTOR  1.277           MASS FLUX             228.8 KLBM/H/SQ-FT
       HEAT TRANSFER COEFFICIENT             HEAT TRANSFER COEFFICIENT
        DRY COIL  .586 BTU/H-SQ-FT-F    VAPOR REGION        133.284 BTU/H-SQ-FT-F
        WET COIL (AVERAGE)    8.083 BTU/H-SQ-FT-F    TWO PHASE REGION    1191.430 BTU/H-SQ-FT-F
        DRY AUGMENTATION FACTOR  0.817
        WET AUGMENTATION FACTOR  0.803
        FIN PATTERN ANGLE      18.41 DEG
       DRY FIN EFFICIENCY (SURFACE) 0.859
       WET FIN EFFICIENCY (AVERAGE) 0.815
       WET CONTACT FACTOR (AVERAGE) 1.330
       REYNOLDS NUMBER        1127.0
      CONTACT INTERFACE:
       CONTACT CONDUCTANCE   130813.523 BTU/H-SQ-FT-F
      UA VALUES PER CIRCUIT:VAPOR     TWO PHASE
                    REGION     REGION
       REFRIGERANT SIDE  39.695     4800.922 BTU/H-F
       AIR SIDE
        DRY COIL      33.431       0.000 BTU/H-F
        WET COIL                 404.046 BTU/H-F
       CONTACT INTERFACE
        DRY COIL     ********      0.000 BTU/H-F
        WET COIL              329325.125 BTU/H-F
       COMBINED
        DRY COIL      18.132       0.000 BTU/H-F
        WET COIL                 372.260 BTU/H-F
**** SUMMARY OF ENERGY INPUT AND OUTPUT *****
-- Heat,Pump, Design Cooling Condition, Max Speed --
      OPERATING CONDITIONS:
       AIR TEMPERATURE INTO EVAPORATOR        79.92 F
       AIR TEMPERATURE INTO CONDENSER         95.00 F
       SATURATION TEMP INTO  COMPRESSOR       48.37 F
       SATURATION TEMP OUT OF COMPRESSOR      120.09 F
      DRIVE FREQUENCIES:
       COMPRESSOR                  60.00 HZ
       INDOOR  FAN                 60.00 HZ
       OUTDOOR FAN                 60.00 HZ
      DRIVE FREQUENCY RATIOS:
       COMPRESSOR                  1.00
       INDOOR  FAN                 1.00
       OUTDOOR FAN                 1.00
```

ENERGY INPUT SUMMARY:
HEAT PUMPED FROM AIR SOURCE 145273.2 BTU/H
POWER TO INDOOR FAN MOTOR 1460.0 WATTS
POWER TO OUTDOOR FAN MOTOR 600.0 WATTS
TOTAL PARASITIC POWER 2060.0 WATTS
POWER TO COMPRESSOR MOTOR 9123.9 WATTS
TOTAL INPUT POWER 11183.9 WATTS
REFRIGERANT-SIDE SUMMARY:
HEAT GAIN TO EVAPORATOR FROM AIR 145273.2 BTU/H
HEAT GAIN TO SUCTION LINE 0.0 BTU/H
ENERGY INPUT TO COMPRESSOR 31130.6 BTU/H
HEAT LOSS FROM COMPRESSOR SHELL 2388.2 BTU/H
HEAT LOSS FROM DISCHARGE LINE 0.0 BTU/H
HEAT LOSS FROM CONDENSER TO AIR 173906.6 BTU/H
HEAT LOSS FROM LIQUID LINE 0.0 BTU/H
ENERGY OUTPUT SUMMARY:
HEAT RATE FROM REFRIGERANT TO INDOOR AIR 145273.2 BTU/H
HEAT RATE FROM FAN TO INDOOR AIR 4981.5 BTU/H

REFERENCES

[1] W. Wongsuwan, S. Kumar, P. Neveu and F. Meunier, A review of chemical heat pump technology and applications, *Appl Thermal Eng* 21 (2001), pp. 1489–1519.

[2] A. Hepbasli and L. Ozgener, Development of geothermal energy utilization in Turkey: a review, *Renewable Sustainable Energy Rev* 8 (2004), pp. 433–460.

[3] O. Ozgener and A. Hepbasli, A review on the energy and exergy analysis of solar assisted heat pump systems, *Renewable Sustainable Energy Rev* 11 (2007), pp. 482–496.

[4] Omer M. Ground-source heat pumps systems and applications. *Renewable and Sustainable Energy Rev*, 2007: in press.

[5] Z. Lian, S. Park, W. Huang, Y. Baik and Y. Yao, Conception of combination of gas-engine-driven heat pump and water-loop heat pump system, *Int J Refrigeration* 28 (2005), pp. 810–819

[6] Nowakowski GA, Inada M, Dearing MP. Development and field testing of a high-efficiency engine-driven gas heat pump for light commercial applications. *ASHRAE Transactions*, AN-92-10-4. p. 994–1000.

[7] Gary A. Nowakowski, An introduction and status update on unitary engine-driven heat pumps, *ASHRAE J* (1996) (December), pp. 42–47.

[8] S. Li, W. Zhang, R. Zhang, D. Lv and Z. Huang, Cascade fuzzy control for gas engine driven heat pump, *Energy Convers Manage* 46 (2005), pp. 1757–1766.

[9] R. Lazzarin and M. Noro, District heating and gas engine heat pump: economic analysis based on a case study, *Appl Thermal Eng* 26 (2006), pp. 193–199.

[10] A. Ficarella and D. Laforgia, Energy conservation in alcohol distillery with the application of pinch technology, *Energy Convers Manage* 40 (1999), pp. 1495–1514.

[11] G.A. Nowakowshi, M. Inada and M.P. Dearing, Development and field testing of a high-efficiency engine-driven gas heat pump for light commercial applications, *ASHRAE Trans* (1992) (Pt. 1), pp. 994–1000.

[12] G. Nowakowski, G. Merten and J. Brogan, Field performance of a 3-ton natural gas engine-driven heating and cooling system, *ASHRAE Trans* (1995) (Pt. 2), pp. 1382–1388.

[13] T. Kaneko, M. Obitani and T. Imura, Performance of a four-ton gas-engine-driven heat pump, *ASHRAE Trans* 98 (1992) (Pt. 1), pp. 989–993.

[14] L. Wolfe Vinton Jr. and P. Getman Robert, Gas engine heat pump performance in a southern climate, *ASHRAE Trans* 101 (1995) (Pt. 2), pp. 1389–1395.

[15] T.L. Cornell, R.L. Hedrick and W.W. Bassett, Performance characterization of an engine-driven gas heat pump in a single-family residence, *ASHRAE Trans* 99 (1993) (Pt. 1), pp. 1430–1435.

[16] G.G. Haselden and D.A. Clark, Experimental studies of a gas engine-driven domestic heat pump Australian refrigeration, *Air Condition Heat* 47 (1993) (1), pp. 25–31.

[17] F.C. Chen, C. Mei Vince and E. Domitrovic Ronald, Test of an improved gas engine-driven heat pump, *ASHRAE Trans* 104 (1998) (Pt. 1B), pp. 1471–1477.

[18] Z. Yang, Z. Haibo and Z. Wu, Technical and economic analysis of gas-engine driven heat pump in China, *Int J Global Energy Issues* 20 (2003) (3), pp. 223–232.

[19] T. Yokoyama, Design considerations for gas-engine heat pumps, *ASHRAE Transactions* 1992, v.98, pt.1.

[20] J.W. MacArthur and E.W. Gerald, Unsteady compressible two-phase flow model for predicting cyclic heat pump performance and a comparison with experimental data, *Int J Refrigeration* 12 (1989), pp. 29–41.

[21] R.P. Rusk, J.N. Van Gerpen, R.M. Nelson and M.B. Pate, Development and use of a mathematical model of an engine-driven heat pump, *ASHRAE Trans* (Pt. 2) (1990), pp. 282–290.

[22] Z. Yang, S. Zhang and H. Zhao, Dynamic study of the exhaust heat recovery system for a gas engine-driven heat pump, *ACTA Energiae Solaris Sinica* 25 (2004), pp. 712–716.

[23] Y. Shin, H. Yang, C.-S. Tae, C.-Y. Jang and S. Cho, Dynamics modeling of a gas engine-driven heat pump in cooling mode, *J Mech Sci Technol* 20 (2006), pp. 278–285.

[24] R.R. Zhang, X.S. Lu, S.Z. Li, W.S. Lin and A.Z. Gu, Analysis on the heating performance of a gas engine driven air to water heat pump based on a steady-state model, *Energy Conversion Manage* 46 (2005), pp. 1714–1730

[25] L.A. Howe, R. Radermacher and K.E. Herold, Combined cycles for engine-driven heat pumps, *Int J Refrigeration* 12 (1) (1989), pp. 21–28.

[26] C.D. Rakopoulos and E.G. Giakoumis, Second-law analyses applied to internal combustion engines operation, *Progr Energy Combust Sci* 32 (2006), pp. 2–47.

[27] Radermacher, R. and Jung, D., 1991. Theoretical analysis for replacement refrigerants for R-22 for residential uses, *U.S. Environmental Protection Agency Report*, US EPA/400/1-91/041.

[28] Kondepudi, S. N., 1993. Drop-in testing of R-32 blends As R-22 alternatives in a split-system air conditioner, *ASHRAE Transactions*, vol. 99, pt. 2, pp. 406-413.

[29] Domanski, P. A. and Didion, D. A., 1993. Thermodynamic evaluation of R-22 alternative refrigerants and refrigerant mixtures, *ASHRAE Transactions*, vol. 99, pt. 2, pp. 627-635.

[30] Bivens, D. B., Shiflett, M. B., Wells, W. D., Shealy, G. S., Yokozeki, A., Patron, D. M.,Kolliopoulos, K. A., Allgood, C. C., and Chisolm, T. E. C., 1995. HFC-22 alternatives for air conditioners and heat pumps," *ASHRAE Transactions*, vol. 101, pt. 2, pp. 1065-1071.

[31] ASHRAE Refrigeration Handbook, ISBN 1-883413-54-0, Chapter 2, (1998).

[32] Stoecker, W. F. and Walukas, D. J., Conserving energy in domestic refrigerators through the use of refrigerant mixtures, *ASHRAE Transactions,* Vol. 87, No. 1, pp. 279-281, (1981).

[33] McLinden, M.O., Optimum refrigerants for non-ideal cycles: an analysis employing corresponding states, *Proceedings ASHRAE – Purdue CFC and IIR – Purdue Refrigeration Conferences*, W. Lafayette, IN July 17-20, (1990).

[34] Domanski, P. A., and Didion, D. A., Thermodynamic evaluation of R22 alternative refrigerants and refrigerant mixtures, *ASHRAE Transactions*, Vol. 99, No. 2, pp. 636-648, (1993).

[35] Domanski, P. A., Didion, D. A., and Doyle, J. P., Evaluation of suction-line/liquid-line heat exchange in the refrigeration cycle", *Rev. Int. Froid*, Vol. 17, No. 7, pp. 487-493, (1994).

[36] Bivens, D. B., Allgood, C. C., Shiflett, M. B., Patron, D. M., Chisolm, T. C., Shealy, G. S., Yokozeki, A., Wells, W. D., and Geiger, K. A., HCFC-22 alternative for air conditioners and heat pumps", *ASHRAE Transactions*, Vol. 100, No. 2, pp. 566-572, (1994).

[37] Bittle, R. R., Stephenson, W. R., and Pate, M. B., An experimental evaluation of capillary tube-liquid-suction heat exchanger performance with R152a, *ASHRAE Transactions*, Vol. 101, No. 1, pp. 124-135, (1995a).

[38] Bittle, R. R., Stephenson, W. R., and Pate, M. B., An evaluation of the ASHRAE method for predicting capillary tube-liquid-suction heat exchanger performance", *ASHRAE Transactions*, Vol. 101, No. 2, pp. 434-442, (1995b).

[39] Klein S. A., Reindl D. T., and Brownell K., Refrigeration system performance using liquid-suction heat exchangers, *International Journal of Refrigeration,* Vol. 23, Part 8, pp. 588-596 (2000).

[40] Kim, M. H., Shin, H. S, Kim, K. J., The performance of R-407C and R-410B in a residential window air-conditioner with a liquid suction heat, *American Society of Mechanical Engineers Advanced Energy Systems Division (Publication) AES* Volume 41, 2001, Pages 173-178.

[41] B. E. Launder and D. B. Spalding, Lectures in Mathematical Models of Turbulence, Academic Press, London, England, 1972.

[42] R. D. Ellison and F. A. Creswick, A computer simulation of steady state performance of air-to-air heat pumps, *ORNL/CON-16*, 1978.

[43] R. D. Ellison et al., Heat pump modeling: A Progress Report, *Proceedings of the Fourth Annual Heat Pump Technology Conference*, Oklahoma State University, Stillwater, April 9-10, 1979.

[44] C. C. Hiller and L. R. Glicksman, Improving heat pump performance via compressor capacity control-analysis and test, *VOWS. I and II MIT Energy Laboratory Report No. MIT-EL 76-001,* 1976.

[45] G. T. Kartsounes and R. A. Erth, Computer Calculation of the thermodynamic properties of refrigerants 12, 22, and 502, *ASHRAE Transactions*, Vol. 77, Part II, 1971.

[46] J. E. Flower, Analytical modeling of heat pump units as a design aid and for performance prediction, *Lawrence Livermore Laboratory Report*, UCRL-52618, 1978.

[47] T. Kusuda, NBSLD, the computer program for heating and cooling loads in buildings, *NBS Building Science Series 69*, July 1976.

[48] Air-Conditioning & Refrigeration Institute (ARI) Standard 540, Performance rating of positive displacement refrigerant compressors and compressor units, 2004.

[49] A. E. Dabiri and C. K. Rice, A compressor simulation method with corrections for the level of suction as superheat, ASHRAE Transactions, Vol. 87, Part II, 1981.

[50] J. E. Flower, Analytical modeling of heat pump units as a design aid and for performance prediction, *Report, UCRL-52618, Lawrence Livermore Laboratory*, 1978.

[51] G. T. Kartsounes and R. A. Erth, Computer calculation of the thermodynamic properties of Refrigerants, *ASHRAE Transactions*, Vol. 77, Part II, 1971.

[52] W. M. Kays and A. L. London, Compact heat exchangers, *McGraw-Hill Book Company*, New York, 1974, p. 182.

[53] F. W. Dittus and L. M. K. Boelter, University of California (Berkeley) Pub. Eng., Vol. 2, p. 443, 1930.

[54] F. C. McQuiston, Finned tube heat exchangers; state of the art for the air side, *ASHRAE Transactions*, Vol. 87, Pt. 1, 1981.

[55] F. C. McQuiston, "Correlation of heat, mass, and momentum transport coefficients for plate-fin-tube heat transfer surfaces with staggered tube, *ASHRAE Transactions*, Vol. 84, Part I, 1978.

[56] R. J. Myers, The effect of dehumidification on the air-side heat transfer coefficient for a finned tube coil, *University of Minnesota Master's Thesis*, 1967.

[57] T. E. Schmidt, Heat transfer calculations for extended surfaces, *Refrigerating Engineering*, April 1949, pp. 351-357.

[58] F. C. McQuiston and D. R. Tree, Optimum Space Envelopes of the Finned Tube Heat Transfer Surface, *ASHRAE Transactions*, Vol. 79, Pt. 2, 1973.

[59] J. R. S. Thorn, Prediction of pressure drop during forced circulation boiling of water, International Journal of Heat and Mass Transfer, Vol. 7, pp. 709-724, 1964.

[60] S. D. Goldstein, On the calculation of R-22 pressure drop in HVAC evaporators, ASHRAE Transactions, Vol. 85, Part 2, 1979.

[61] F. Geary, Return bend pressure drop in refrigeration Systems, ASHRAE Transactions, Vol. 81, Pt. I, 1975.

[62] American Society of Heating, Refrigerating, and Air-Conditioning Engineers, Inc., Method of Testing for Rating Heat Operated Unitary Air-conditioning Equipment for Cooling, *ASHRAE ANSI/ ASHRAE 40,* 1980.

[63] ANSI/ASHRAE 41.1-1986 (RA 2006), Standard Method for Temperature Measurement, 2006.

[64] ASME Power Test Code (PTC) 19.2-1987 (Reaffirmed 2004), Instruments and Apparatus, Part 2, Pressure Measurements, *American Society of Mechanical Engineers (ASME)*, 345 E. 47th St., New York NY 10017, 2004.

[65] ANSI/ASHRAE 41.3-1989, Standard Method for Pressure Measurement, 1989.

[66] ASME Power Test Code (PTC) 19.5-2004, Flow Measurement, 2004.

[67] ASHRAE 41.8-1989, Standard Methods of Measurement of Flow of Liquids in Pipes Using Orifice Flow meters, 1989.

[68] American Society of Heating, Refrigerating, and Air-Conditioning Engineers, Inc., 1988, Method of Testing for Rating Unitary Air-conditioning and Heat Pump Equipment, *ASHRAE ANSI/ ASHRAE 37.*

[69] NIST REFPROP V7.0, Reference Fluid Thermodynamic and Transport Properties, 2002.

[70] American Society of Heating, Refrigerating, and Air-Conditioning Engineers, Inc., Methods of Testing for Seasonal Efficiency of Unitary Air-conditioners and Heat Pumps, *ASHRAE ANSI/ ASHRAE 116,* 1995.

[71] Beckwith, T., R. Marangoni, and J. Lienhard, Mechanical Measurements, Addison-Welsey Publishing Company, 1993.

[72] Kline, S. and F. McClintock, Describing Uncertainties in Single-Sample Experiments, Mech. Eng., Vol. 75, pp. 3-8, 1953.

[73] ARI 340/360-2004 Standard, Performance Rating of Commercial and Industrial Unitary Air-Conditioning and Heat Pump Equipment, *Air-Conditioning & Refrigeration Institute*, 2004.

[74] ANSI/ASHRAE Standard 40-2002, Methods of Testing for Rating Heat-Operated Unitary Air-Conditioning and Heat Pump Equipment, 2002.

[75] ANSI Z21.40.4a-1998 and CGA 2.94a-M98 Standard, Performance Testing and Rating of Gas-Fired, Air-Conditioning and Heat Pump Appliances, 1998.

[76] Deru, M. and Torcellini, P., Source Energy and Emission Factor for Energy Use in Buildings, NREL/TP-550-38617.

[77] Energy Information Administration / Annual Energy Review, 2008

VITA

Graduate College
University of Nevada, Las Vegas

Isaac Y. Mahderekal

Local Address:
2181 Norwegian Wood Lane
Henderson, NV 89074

Degrees:

Bachelor of Science, Mechanical Engineering, 2002
University of Nevada, Las Vegas, USA

Master of Science, Mechanical Engineering, 2004
University of Nevada, Las Vegas, USA

Selected Publications:

I. Mahderekal and R. F. Boehm, Thermal Analysis of a Concentrating Photovoltaic Receiver, *ISEC SOLAR 2004 Conference*, paper 65006.

I. Mahderekal, C. Halford, and R. Boehm, Simulation and Optimization of a Concentrated Photovoltaic System, *Journal of Solar Energy Engineering*, May 2006, pp. 139-145.

I. Mahderekal, A. Zaltash and E. Vineyard, Laboratory Evaluation of a Gas Engine Driven Heat Pump, *ASHRAE Transactions*, SL-08-022, 2008.

I. Mahderekal, K. Hinderliter and T. Young, Design and Development of a Gas Engine Driven Heat Pump (GHP), *ASME Proceedings of ES2008-54110*, 2008.

I. Mahderekal, K. Hinderliter and R. Boehm, The Development of a Model for a Solar-Fired Single Effect Absorption Chiller, Engine Driven Heat Pump (GHP), *ASME Proceedings of ES2008-54186*, 2008.

Dissertation Title: Experimental Evaluation and Modeling of Engine Driven Heat Pump

Dissertation Examination Committee:

Chairperson, Robert Boehm, Ph. D., P.E.
Committee Member, Woosoon Yim, Ph. D.
Committee Member, Samir F. Moujaes, Ph. D., P. E.
Committee Member, Daniel Cook, Ph. D.
Graduate College Representative, Eugene McGaugh, Ph. D.